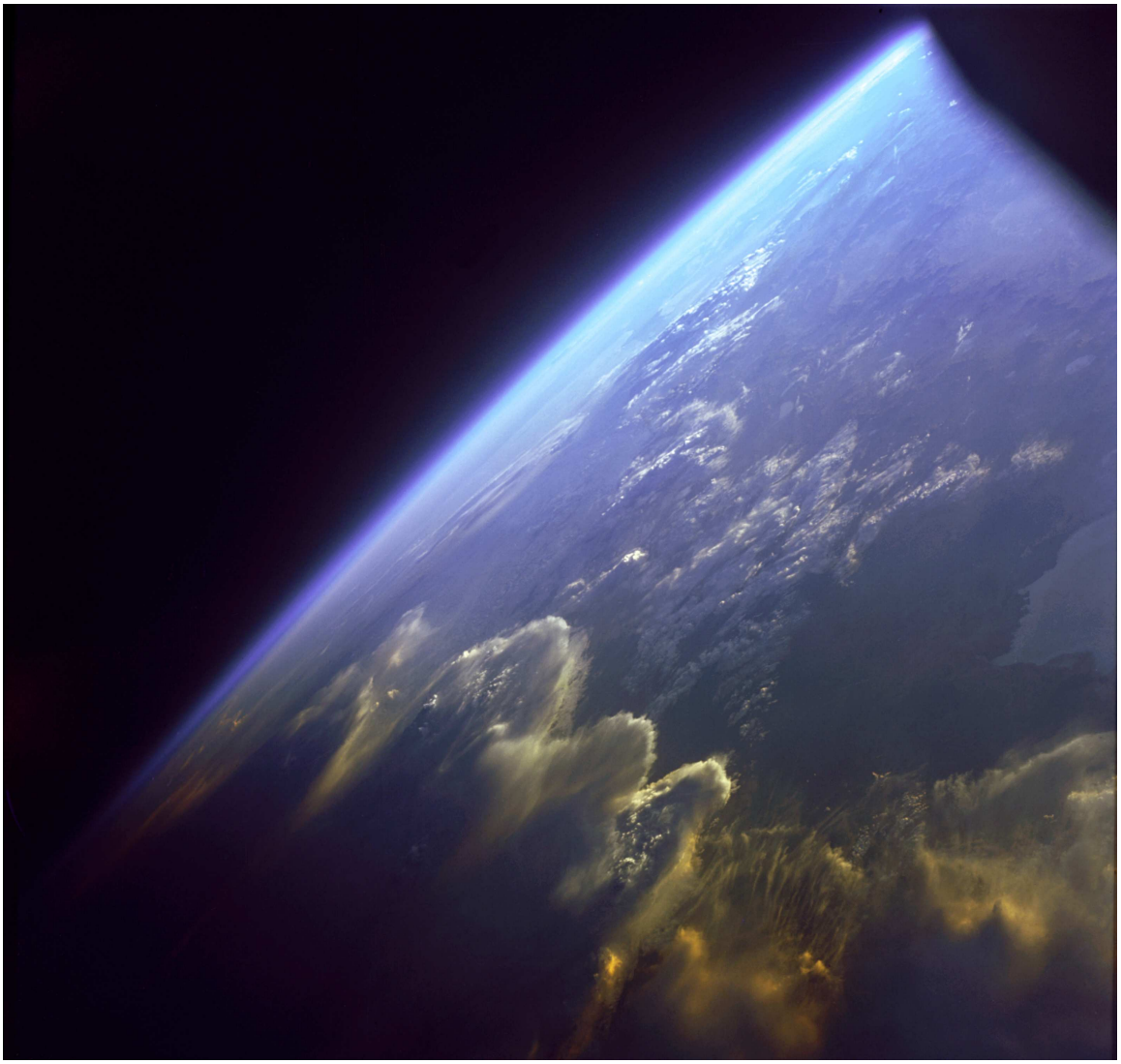

This thesis was typeset with LaTeX, using a modified version of the University of California Ph.D. dissertation class file, `ucthesis.cls`. Unless otherwise noted, all figures in this thesis were created by the author using IDL® or CorelDraw®.

The view on the cover was photographed by astronauts Frank Borman and James A. Lovell during the Gemini 7 mission in 1965. The image is looking South from Northern Bolivia across the Andes. Waves of clouds along the east flanks of the Andes Mountains cast off an orange glow by the low angle of the sun in the West. The dark area to the left is the Earth's terminator. The Intermontane Salt Basins are visible in the background. (Photo courtesy of NASA.)

IRMA CALIBRATIONS AND DATA ANALYSIS FOR TELESCOPE SITE SELECTION

Richard Robert Querel

Bachelor of Science, Honours Physics, University of Waterloo (2000)

A thesis
submitted to the School of Graduate Studies
of the University of Lethbridge
in partial fulfilment of the
requirements of the degree

MASTER OF SCIENCE

Department of Physics
University of Lethbridge
Lethbridge, Alberta, Canada

for the Universe, and
Cindy because you make all things shine,
Bob and Diane because you treat everyone like gold,
Denise for being such a wonderful mom,
André for your *joie de vivre*,
my family, my friends,

and Roméo, your life continues to inspire.

Abstract

Our group has developed a 20 μm passive atmospheric water vapour monitor. The Infrared Radiometer for Millimetre Astronomy (IRMA) has been commissioned and deployed for site testing for the Thirty Meter Telescope (TMT) and the Giant Magellan Telescope (GMT). Measuring precipitable water vapour (PWV) requires both a sophisticated atmospheric model (BTRAM) and an instrument (IRMA). Atmospheric models depend on atmospheric profiles. Most profiles are generic in nature, representing only a latitude in some cases. Site-specific atmospheric profiles are required to accurately simulate the atmosphere above any location on Earth. These profiles can be created from publicly available archives of radiosonde data, that offer nearly global coverage. Having created a site-specific profile and model, it is necessary to determine the PWV sensitivity to the input parameter uncertainties used in the model. The instrument must also be properly calibrated. In this thesis, I describe the radiometric calibration of the IRMA instrument, and the creation and analysis of site-specific atmospheric models for use with the IRMA instrument in its capacity as an atmospheric water vapour monitor for site testing.

Acknowledgements

I'd like to thank David Naylor for welcoming me into the Astronomical Instrumentation Group. It's every bit as off-the-wall as he had originally hailed it to be. Thanks to the group for always being so helpful. Locke for happily stopping whatever he was doing to help, whether it be with an equation, or hauling hundreds of kilograms of scrap lumber. Regan for tolerating what must have sometimes felt like incessant questioning in regards to IRMA software, or computer related issues in general. Regan, you've been infinitely helpful, and I thank you for that. Greg for bringing light and laughter into the lab, whether that be with magnets, moon landing hoaxes or your disdain for relativity. Your knowledge of the IRMA electronics is amazing. It's been great being here in Chile with you.

I'd like to acknowledge the previous people who have brought the IRMA project to where it is today. Graeme, whom I haven't met, started the IRMA work. Ian C. for creating ULTRAM, without which none of the site-specific atmospheric modeling could have been done. Ian S. for building up the communication and control system that serves as the backbone for the IRMA hardware. Dr. Robin Phillips for his work as Project Manager, integrating the cryocooler, helping to make IRMA-III capable of remote operation, and beginning the Antarctic IRMA retrofit process. Thanks to Scott Jones for all his help around the lab. Thanks to Dan Sirbu for all his work too.

I'd also like to thank Matthias Schöck, Project Manager, TMT Site Testing Committee, for his help calibrating the TMT IRMA units. Thank you to Joanna Thomas-Osip for her help in both Lethbridge and Las Campanas, getting the LCO IRMA unit up and running, and troubleshooting as we went along.

Thanks to Drs. Peter Ade and Carole Tucker, University of Cardiff, for supplying us with specially designed IR filters. Thanks to Fluke for loaning us the Ti20 Thermal Imager that started us down the calibration rabbit-hole. Thanks to NSERC, HIA and NRC for funding the IRMA project.

I'm grateful for all of my friends and family, most of whom haven't seen me lately. The trials of a graduate student I'm told. No need to worry, I can already smell the green grass. I'm especially grateful to have Cindy in my life, I look forward to spending much more time together. It's been a long while.

Thank you again to David Naylor for painstakingly going over and revising and editing this thesis. You've been a wonderful help, without which this thesis would have taken on a very different form. Thank you for your time.

— RRQ, September 2007, LCO, Chile

Table of Contents

List of Figures

List of Tables

List of Abbreviations

AASTINO	Automated Astrophysical Site Testing INvincible Observatory
ACURA	Association of Canadian Universities for Research in Astronomy
ADC	Analog-to-digital converter
AHS	Alignment heat source
AIG	Astronomical Instrumentation Group
ALMA	Atacama Large Millimetre Array
ALTAZ	Altitude-Azimuth
AR	Anti-reflection
AWS	Automatic weather station
BB	Blackbody
BTRAM	Blue Sky Transmission and Radiance Atmospheric Model
DAQ	Data acquisition board
DC	Direct current
EM	Electromagnetic
ESO	European Southern Observatory
FASCODE	Fast Atmospheric Signature Code
FPI	Fabry-Pérot interferometer
FTS	Fourier Transform Spectrometer
FWHM	Full-width at half-maximum
GMT	Giant Magellan Telescope
HWHM	Half-width at half-maximum
IDL	Interactive Data Language
IR	Infrared
JCMT	James Clerk Maxwell Telescope
JWST	James Webb Space Telescope
IRMA	Infrared Radiometer for Millimetre Astronomy
LBB	Large Diameter Reference Blackbody
LBL/LBL	Line-by-line/Layer-by-layer
LCO	Las Campanas Observatory

LN_2	Liquid Nitrogen (N_2)
LTE	Local Thermodynamic Equilibrium
LPE	Local Hydrostatic Equilibrium
MCT	Mercury Cadmium Telluride
MIKE	Magellan Inamori Kyocera Echelle spectrograph
NOAA	National Oceanic & Atmospheric Administration (US)
OAP	Off-axis parabolic mirror
OWL	Overwhelmingly Large Telescope
PWV	Precipitable Water Vapour
RH	Relative Humidity
S/N	Signal-to-noise
SMA	Smithsonian Millimeter Array
TMT	Thirty Meter Telescope
UL	University of Lethbridge
ULTRAM	University of Lethbridge Transmission and Radiance Atmospheric Model
USB	Universal Serial Bus
USSA1976	U.S. Standard Atmosphere 1976
UV	Ultraviolet
ZnSe	Zinc-Selenide

Chapter 1

Introduction

1.1 Overview

Developed as a collaboration between the University of Lethbridge and the Herzberg Institute of Astrophysics, the Infrared (IR) Radiometer for Millimetre Astronomy (IRMA) [1] is a light weight and relatively low cost radiometer designed for determining atmospheric water vapour column abundance above high altitude telescope sites around the world. It uses an infrared Mercury Cadmium Telluride (MCT) photoconductive detector [2] to measure the emission from water vapour rotational transitions in a carefully chosen spectral band centred around 20 μm. The total power detected in this band is converted to a column abundance expressed in terms of precipitable water vapour (PWV) using BTRAM, an atmospheric model developed by previous members of our research group [3].

IRMA is a compact, reliable instrument with low power consumption requirements, and therefore lends itself to remote sensing applications. As a result, IRMA is now being used by several major new telescope projects to help select their construction sites. Three

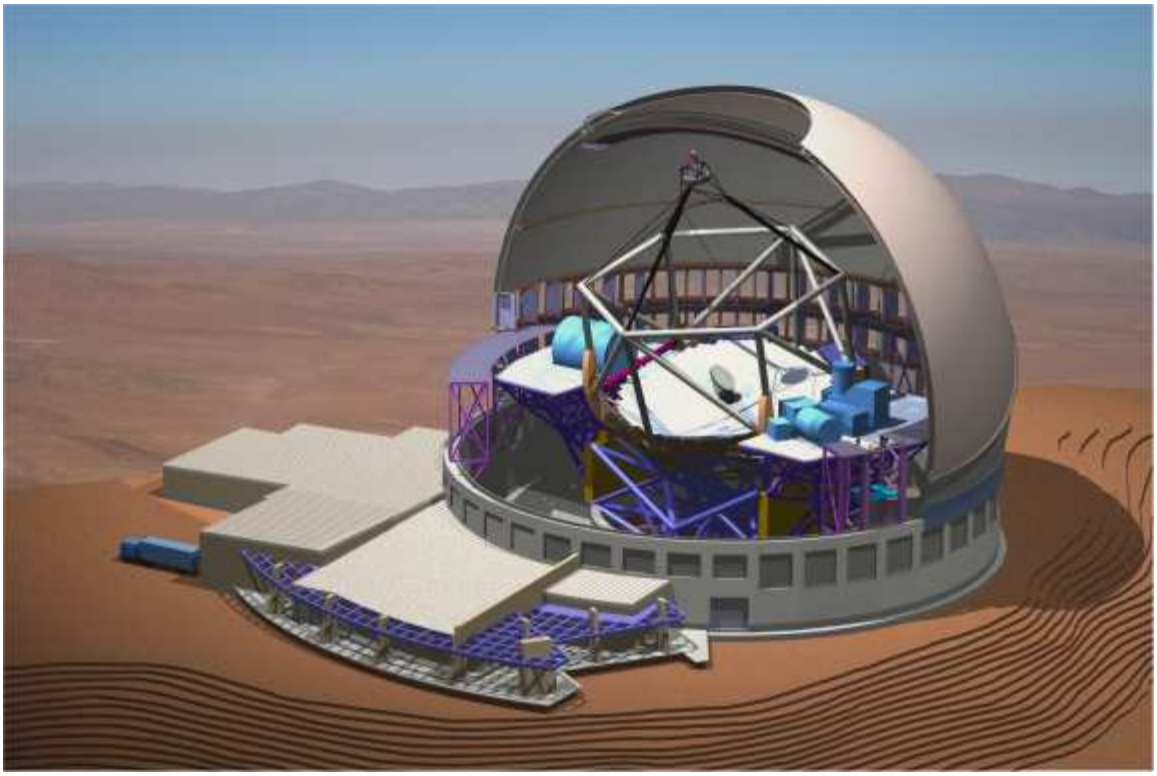

Figure 1.1: An artist rendering of the Thirty Meter Telescope (TMT) project, which is currently in the preliminary design phase. Credit: Thirty-Meter Telescope Project

new IRMA units have been readied for the Thirty Meter Telescope (TMT) project, see Figure 1.1. These three units have been deployed on mountain sites being considered in Chile, Mexico and Hawaii by the TMT site selection committee. In addition to these three, the Giant Magellan Telescope (GMT) has ordered one IRMA unit for surveying several candidate peaks at the Las Campanas Observatory (LCO) site in Chile. In addition to the TMT sites testing units, an IRMA unit is currently being modified for extreme cold weather operation (-80 °C) for site observation and testing at Dome C, Antarctica. In collaboration with the University of New South Wales, a modified IRMA unit will be deployed at the Automated Astrophysical Site Testing INvincible Observatory (AASTINO) [4] instrumentation platform for September 2007 in preparation for the Antarctic winter,

Figure 1.2: The Automated Astrophysical Site Testing INvincible Observatory (AASTINO) at Dome C, Antarctica [4]. The two cylindrical buildings seen in the background are the French-Italian jointly operated Concordia Research Station. Photo Credit: Dept of Astrophysics, UNSW 2004.

see Figure 1.2. Antarctica is a proposed site for future large astronomical telescopes. The main reasons cited are its relatively stable atmosphere (due to low wind velocities,) very low levels of precipitation, and thus a dry atmosphere with low values of PWV implying low atmospheric opacity at infrared wavelengths. Studies have shown that Dome C has equal or better observing conditions than all other terrestrial sites. For roughly 0.5% of the time, the expected observation quality of a telescope at Dome C will match that of the space-based Hubble telescope [5]. This is amazing for a ground based telescope, since it must contend with the highly variable conditions of the atmosphere surrounding it. While technically the

most challenging retrofit of an IRMA unit to date, the Dome C site is expected to be one of the best locations for performing astronomical measurements.

My thesis reports on the contributions that I have made to modeling the atmosphere above various proposed test sites, performing sensitivity analyses on the parameters used in the models, and the full calibration of the IRMA units. All work with the IRMA units will assist in understanding the full range of precipitable water vapour at several high-altitude locations. While the Mauna Kea site is well characterized, sites in Chile and Antarctica are less well understood. Knowing that water vapour dramatically affects the transmission of radiation from astronomical sources, it is essential to have accurate, real-time information about the atmospheric water vapour column abundance and its variability.

TMT will allow for measurements of greater spatial resolution than was previously possible, but this hinges on having and identifying "good"observing nights. A good observing night would include many of the following features; a cloudless night, steady temperature, and little or no air movements to minimize the turbulence that creates the blurring and twinkling of astronomical objects, referred to as astronomical seeing. The factor missing from this list is water vapour. Water vapour is invisible at optical wavelengths. What the naked eye might see as a "clear"night at optical wavelengths may actually represent an atmosphere containing a significant amount of PWV, rendering the atmosphere opaque in the infrared region of the spectrum.

The current TMT site test plan is to collect several months of site data from the three TMT units. These data will then be processed, providing us with a large data set from which to derive statistical information about the potential sites. The analysis will influence the future location of the TMT telescope and the subsequent science that will be

performed. The importance of the site testing process cannot be overemphasized.

TMT is a billion dollar collaboration between the California Institute of Technology (Caltech), the University of California, and the Association of Canadian Universities for Research in Astronomy (ACURA). Due to the large scale of the TMT project, in terms of both the potential for ground-breaking scientific research, and the economics of the project, the site selection committee requires environmental data from candidate sites to make the best possible decision about where to locate the telescope. While no such instrument is currently scheduled for construction at Dome C, there is still interest in characterizing the Antarctic site in regards to water vapour.

In preparing the IRMA units for TMT deployment some difficulties with the calibration process were identified. In the earlier versions of the IRMA instrument, liquid nitrogen (LN_2) was used to cool the photodetector and was thus readily available to serve as a cold load to be used in a 2-point calibration scheme along with an ambient blackbody [1]. When IRMA was modified to allow for remote operation, the wet cryostat was replaced with a Stirling cycle cryocooler [6] that no longer required LN_2. The 2-point temperature scheme of LN_2 and ambient blackbody was replaced with a two-point ambient and hot blackbody measurement. Since the effective sky temperature is less than the ambient surface temperature, an extrapolation of the two point calibration is required, which places additional importance on accurately knowing the effective temperature of the blackbody surface, depicted in Figure 5.2.

For the IRMA unit operating at Mauna Kea, Hawaii, the new 2-point calibration scheme based on the internal blackbody proved adequate. However, for the units operating near Las Campanas, Chile, this was no longer the case. The lower altitude, 2400 m as com-

Figure 1.3: Inclement weather experienced at Gemini South, Cerro Pachon, Chile. Photo taken with the IRMA webcam.

pared to 4200 m at Mauna Kea, and the associated higher ambient temperatures, ranging from −10 °C to +20 °C (as compared to typical temperature of 0 °C to +10 °C at Mauna Kea), affected the instrument performance and sensitivity. Calibration values no longer appear constant, but exhibit a dependence upon internal instrument temperature. These variations in instrument temperature are attributed to the aforementioned environmental conditions and daily events such as sunrise, daylight, sunset, twilight, but more importantly to possible contamination from stray light due to unidentified thermal sources.

To study these effects, and subsequently correct for them, we needed first to identify them. So rather than assuming the surface temperature of the internal blackbody, a process of iterative calibrations was performed. First, the IRMA unit was calibrated using a reference blackbody with temperature diodes embedded into its surface to allow precise determination of its surface temperature. These reference blackbody measurements were

linearly fitted with the IRMA photodetector voltage and internal IRMA unit temperatures. A second fit was then performed by fitting a series of internal blackbody measurements to the "known" flux values measured from the calibrated reference blackbody. Thus, the potential stray radiation contaminations could be systematically identified and accounted for. Chapter 5 fully describes this calibration process and the results obtained from multiple calibrated IRMA units.

Having calibrated multiple IRMA units, they can be deployed to remote sites, and measure PWV. These PWV values, effectively atmospheric opacities, can be analysed to aid in the site selection process. However, the role of IRMA will continue after the site has been selected. An IRMA unit will be deployed at the selected site to serve as a real-time opacity monitor to assist in identifying those nights best suited for performing infrared astronomical observations.

1.2 Precipitable water vapour

Water is essential for life [7]. Most animals and plants contain more than 60% water by volume. Water is the only substance on Earth that co-exists simultaneously in all three physical states of matter: solid, liquid and gas. More than 70% of the Earth's surface is covered with approximately 1.36×10^9 km^3 water/ice [8].

Precipitable water vapour (PWV) refers to the depth of liquid water present upon condensing a vertical column of unit cross sectional area. Unless otherwise specified, the column would be the height of the atmosphere. PWV is a linear parameter referred to in units of mm. If 1 mm PWV was condensed over an area of 1 m^2, the resulting liquid water would have a mass of 1 kg, since 1 m^3 of water has a mass of 1000 kg.

Figure 1.4: Water vapor condensing over a cup of hot tea.

Over time, liquid water, like the Earth oceans, comes to an equilibrium at its surface with the concentration of water vapour above it. If there is no motion this equilibrium will be fixed. For example, there is water vapour in equilibrium above a cup of tea, as shown in Figure 1.4. If you blow away this water vapour, the concentration will decrease so that "new"molecules of water will evaporate from the liquid and take their place. When the "new"molecules evaporate they take with them some heat from the liquid, this is the mechanism by which tea is cooled by blowing on it. If the atmosphere is assumed to be at equilibrium, than the ocean can be considered to be a covered cup of water. Over time there will be an equilibrium reached between the water molecules on the ocean surface and the water molecules in the air above the ocean. The amount of water in the air will depend on the temperature of both the ocean and the air. An example of this relationship between

ocean temperature and airborne water vapour is seen in the El Niño-Southern Oscillation (ENSO) [8], where the surface temperature of large areas of the Pacific ocean can increase by as much as 6 K. As the surface temperature of the oceans increase, the quantity of suspended water vapour increases, resulting in shifting weather patterns that can bring widespread drought over one part of the Earth, and heavy rains over another. Through this mechanism, climate is affected on a global scale.

Gaseous water represents a small but environmentally significant constituent of the atmosphere. The troposphere contains the majority of this water vapour. Besides accounting for most of the Earth's natural greenhouse effect, gaseous water also condenses to form clouds, which may act to warm or cool the surface, depending on the circumstances. In general terms, atmospheric water strongly influences, and is strongly influenced by weather, and weather is modified by climate.

The average residence time of water molecules in the troposphere is ∼10 days. Water depleted by precipitation is replenished by evaporation from the seas, lakes, rivers and the transpiration of plants, and other biological and geological processes [8].

The annual mean global concentration of water vapor would yield about 25 mm of liquid water over the entire surface of the Earth if it were to condense. However, the mean annual precipitation for the planet is on the order of 1 m, which indicates a rapid turnover of water in the air. Figure 1.5 shows the global mean water vapour measured March 21, 2006, by the MODIS instrument on the NASA Terra satellite. PWV in the figure ranges from 0 to ∼75 mm, with the highest PWV values measured across the Tropics. Measurements by the Moderate Resolution Imaging Spectroradiometer (MODIS) cover the entire surface of the Earth every 1-2 days, measuring over 36 spectral bands [9].

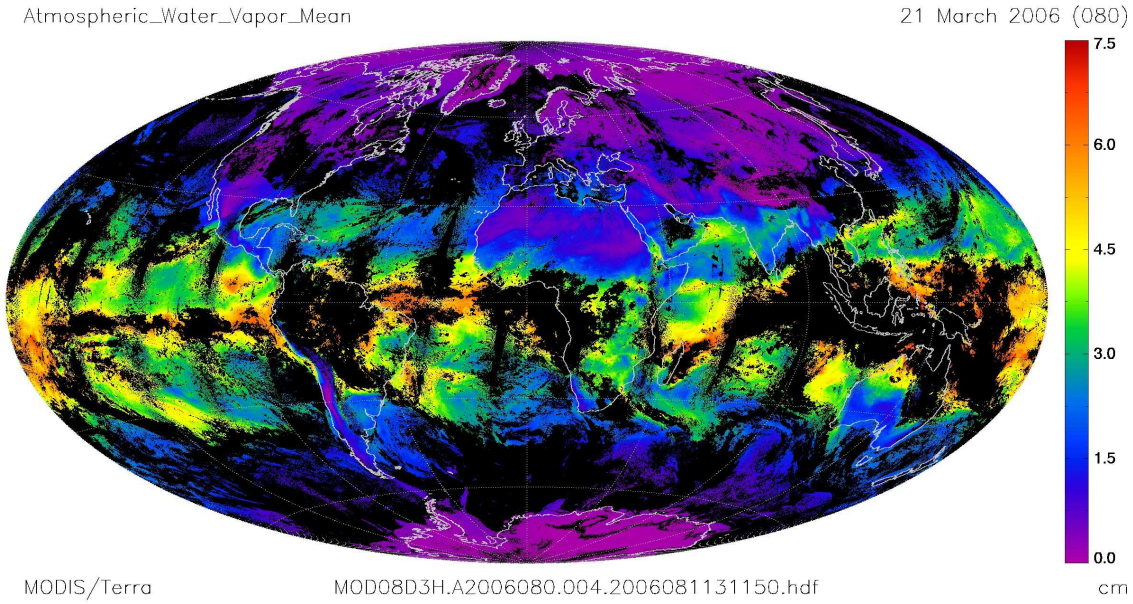

Figure 1.5: Mean atmospheric water vapour for March 21, 2006, as measured by the MODIS instrument on the NASA Terra satellite. Figure courtesy NASA.

The amount of water vapor in the atmosphere directly affects the permittivity of the air [10]. Thus, one way of measuring relative humidity is to measure the capacitance of a parallel plate system using wet air as the dielectric. Some radiosonde instruments use this method to measure humidity. Capacitance, C [C*], is defined as the ratio of charge, Q, to the potential between two conductors, a and b, V_{ab}, given in Equation 1.1.

$$C = \frac{Q}{V_{ab}} = \epsilon_0 \frac{A}{d} \qquad [\mathrm{C}] \quad , \tag{1.1}$$

$$\epsilon = K\,\epsilon_0 \qquad [\mathrm{C}^2\ \mathrm{N}^{-1}\ \mathrm{m}^2] \quad , \tag{1.2}$$

$$C = K\,C_0 = K\,\epsilon_0 \frac{A}{d} = \epsilon \frac{A}{d} \qquad [\mathrm{C}] \quad , \tag{1.3}$$

where ϵ_0 is the permittivity of free space, $\epsilon_0 = 8.854197817 \times 10^{-12}$ C^2 N^{-1} m^2 [10]. The capacitance of a parallel-plate capacitor with conductors of equal area A, and a vacuum separating the plates by a distance d, is given by Equation 1.1. If the vacuum is replaced

*1 coulomb is the amount of electric charge transported by a current of 1 ampere in 1 second.

with a dielectric, the capacitance increases by a factor K. The dielectric constant, K, of 1 atmosphere of dry air at 293 K is $K = 1.00059$, whereas the dielectric for water at 293 K is $K = 80.4$ [10]. This sizeable difference in K lends itself to the determination of the quantity of water vapour within a given quantity of air. Since the permittivity of the dielectric constant of wet air is a function of humidity, using Equations 1.1 and 1.3, it is possible to calibrate and characterize such a device to measure relative humidity. Relative humidity will be discussed further in §4.5.1.

M. C. B. Ashley, *et al.* state the following in their 2004 paper entitled "Robotic telescopes on the Antarctic plateau" [11] : "The Atacama desert has less annual precipitation than the Antarctic plateau, but the figure of merit that is important for astronomers is not the precipitation, but the column of precipitable water vapour (PWV). All the plateau sites are superior to Atacama, both in absolute PWV and, perhaps more importantly, in the stability of the PWV on timescales of minutes to hours. The low PWV has two effects: it opens up new windows, e.g., 200 μm, and it makes existing windows from the ultra-violet to the sub-millimetre and beyond wider and more stable". This allows for a wider variety of observing techniques and technologies to be applied in exploring the night sky.

1.3 Radiative transfer / Atmospheric modeling summary

Radiative transfer is the study of how energy in the form of electromagnetic (EM) radiation propagates through a medium, in our case through a mixture of gases (the atmosphere). Chapter 3 introduces the underlying principles of radiative transfer that are required to accurately model an atmosphere.

Extracting meaningful results from a remote sounding instrument always involves

use of a sophisticated atmospheric model. Atmospheric models tend to come in a variety of forms, the simplest being a plane-parallel, static (non-convective), non-scattering (containing no aerosols, man-made or naturally occurring, no ice-crystals and no clouds), and having a smooth distribution of matter. All of these constraints may seem to reduce the overall applicability or realism of the model, however, they serve to make it simpler and faster computationally while maintaining the defining physical features of the system.

Models depend on many parameters including temperature, pressure, adiabatic lapse rate, scale height, mixing ratios, zenith angle and the nature of the radiation input to the atmosphere [12] (for example looking through an atmosphere at the sun, both the sun's blackbody profile and atmospheric profile would need to be taken into account and corrected). Chapter 4 describes the process of determining the sensitivity of the final PWV to error in the aforementioned model input parameters.

1.4 BTRAM summary

Blue Sky Transmission and Radiance Atmospheric Model (BTRAM, formerly ULTRAM [12]) is a line-by-line radiative transfer model used to simulate transmission through and emission from a user-definable atmosphere. BTRAM was developed by David Naylor and Ian Chapman [3] of the Astronomical Instrumentation Group at the University of Lethbridge. It began as a customizable GUI version with a simplified subset of geometries available in Fast Atmospheric Signature Code (FASCODE) [13]. FASCODE was written in FORTRAN and enabled complicated geometries. By simplifying the available geometries and building the model in IDL® [14], BTRAM allows for customizable atmospheres based on radiosonde data, or through modifying pre-built profiles which include: Antarctic

Summer, Chajnantor Winter, Mauna Kea, Mid-Latitude Summer, Mid-Latitude Winter, Sub-Arctic Summer, Sub-Arctic Winter, Tropical, and U.S. Standard. BTRAM uses the HITRAN 2004 spectral line database for molecular line information [15].

1.5 IRMA summary

The Astronomical Instrumentation Group (AIG) at the University of Lethbridge (UL), under the supervision of Dr. David Naylor has been developing an Infrared Radiometer for Millimetre Astronomy (IRMA) that uses a novel technique for measuring precipitable water vapour. IRMA is a simple infrared radiometer (measures electromagnetic radiation in the infrared region of the spectrum) using a narrow range of the spectrum centred around 20 μm (∼15 THz). The benefits of this region are that it contains primarily rotational spectral features of water vapour [16] and little else, so, to first order, the integrated flux over this narrow band can be attributed to emission from water molecules.

There are two main applications for the IRMA radiometer: one is as a real-time phase-delay monitor for sub-millimetre astronomy, to allow for correction to telescope data due to induced atmospheric effects [1] [3], the other is as a sky opacity monitor for use in infrared astronomy. This thesis focuses on the opacity monitoring aspect of the instrument.

1.5.1 IRMA hardware

IRMA has gone through several major design modifications since its proof of concept in December 1999. These include integrating a Stirling-cycle cooler [6], shown in Figure 1.6, to replace the wet cryostat that required liquid nitrogen to maintain its operating temperature. External computer control was eliminated by employing a PC104

Figure 1.6: Photo of the optical side of the IRMA instrument. The shutter/internal blackbody is open. Components including the detector assembly, the cooler controller, chopper wheel, and paraboloid mirror can be seen from this side of the unit. The far side (not pictured) houses the electronics.

embedded computer [17] [18]. A rabbit micro-controller [19] has also been used to control the altitude-azimuth (ALTAZ) hardware in the base mount, shown in Figure 1.3 as the blue base and forks attached to the radiometer unit.

The Infrared Radiometer for Millimetre Astronomy (IRMA) is a compact, relatively low cost, 20 μm water vapour monitor. By carefully choosing a narrow spectral band containing only water vapour rotational transitions it is possible to use a simple infrared detector to measure the total flux emitted by a column of atmosphere and hence, via an atmospheric model, to determine the total precipitable water vapour.

Figure 1.7: An IRMA unit affixed to the primary reflector (left edge) of this radio telescope in the Smithsonian Millimeter Array (SMA) in Hawaii.

The following description of the IRMA hardware was extracted in part from a paper presented at the 2004 SPIE conference in Glasgow, Scotland by Phillips *et al.* [20]. The IRMA instrument consists of a $35 \times 22 \times 19$ cm box weighing approximately 28 kg. Inside this box, the detector is placed in a vacuum vessel that is cooled using a compact, low power consumption Stirling cycle cooler, to its operating temperature of $\sim$70 K, increasing the sensitivity of the measurements. The incident astronomical signal is passband-filtered and then divided by a five-segment chopper blade to provide a 455 Hz chopped signal to the electronics which are controlled by a small PC104 microcomputer. The sky is viewed via a 100 mm f/1 90°off-axis parabolic (OAP) mirror through an opening in the top of the instrument. The opening can be sealed during bad weather by a lid mechanism that includes an attached black body for instrument calibration. The IRMA box can be attached directly to a telescope and aligned with the main telescope beam to be used as a phase correction tool for radio interferometric data, shown in Figure 1.7.

IRMA can also be used as a real-time IR opacity monitor. It is this functionality that will be further described in this thesis. To function as an opacity monitor, IRMA is mounted between the upright forks of a robotic ALTAZ mount. The ALTAZ mount allows the unit to be arbitrarily pointed adding the ability to perform skymaps and skydips, the former referring to 2-D rotation across all degrees of azimuth and elevation, whilst skydips refer to movement along the elevation axis only. These functions can be run from a remote computer, which then logs the data in daily files. Periodic calibrations are performed by observation of an internal blackbody source at two temperatures: once at ambient temperature and then a second after being heated.

Since February 2005, an IRMA has been measuring PWV levels in Chile at the Gemini South site on Cerro Pachon with a second unit added at the nearby Las Campanas observatories site in August 2005. In early 2007 data collection started with three newly built IRMA units at three locations for the TMT project site testing effort. Additionally, an IRMA unit is in the process of being modified in preparation for deployment at Dome C in Antarctica in Fall 2007 as an addition to the suite of instruments on the University of New South Wales' AASTINO site monitoring facility [4].

I present here a description of the features of the TMT IRMA units that enable them to operate in a remote, unattended location in the Chilean desert that are relevant to the similarly remote Dome C operations. In §6.3, I describe the modifications that have been undertaken, and that are currently being tested, in order for the units to operate with minimal redesign at the extremely low Antarctic winter temperatures.

1.5.2 IRMA advantages

The advantages of a 20 μm radiometer for measuring water vapour are as follows: the peak of the Planck curve for typical atmospheric temperatures occurs at 20 μm (500 cm^{-1}) as shown in Figure 3.15; as identified by Naylor *et al.* the 20 μm atmospheric window contains primarily rotational transitions of water vapour, and therefore the integrated flux across the band provides a sensitive measure of water vapour. In its original development, IRMA was designed to function as a phase-delay monitor for radiotelescope arrays. Whereas other measures of water vapour, i.e. a 183 GHz heterodyne oscillator, had the potential of causing significant interference with the radio measurements, IRMA is a passive radiometer and could not cause any interference at radio frequencies. IRMA also has the added benefits

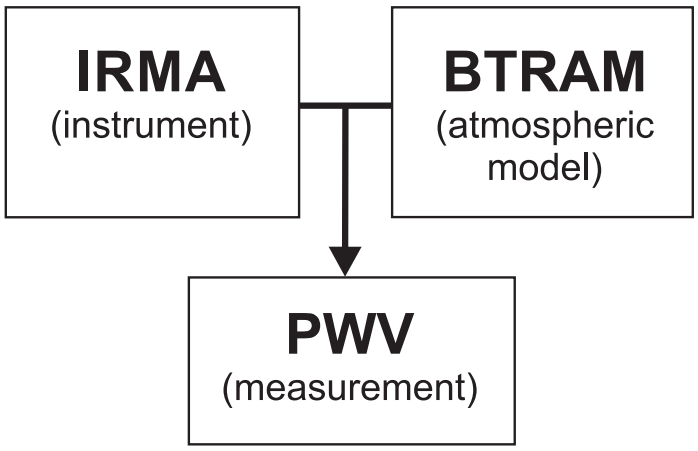

Figure 1.8: Measurements of PWV result from the IRMA-BTRAM, instrument/atmospheric model combination. Uncertainty in either the instrument or atmospheric model will propagate through the system resulting in an uncertainty in the PWV measurement.

of being self-contained, robust, and remotely controlled allowing it to operate away from user intervention in a remote environment.

1.6 Focus of my work in this thesis

As the fourth graduate student working on the IRMA project, my research builds upon that of previous graduate students. Graeme Smith was involved with the proof-of-concept version of IRMA, used at Mauna Kea [1]. Ian Chapman developed the radiative transfer atmospheric model used in conjunction with IRMA to relate atmospheric flux to PWV [3]. Ian Schofield created the communications and control system using a Rabbit microcontroller to enabled the remote operation of the IRMA unit [21]. The primary aim of my thesis was to perform a thorough error analysis on the entire instrument/atmospheric model. Errors associated with internal blackbody temperature measurements were identified and accounted for through implementation of a calibration procedure employing an external calibrated reference blackbody. The atmospheric modeling software [12] was used

to investigate the dependency on retrieved water vapour values as a function of the site-specific model input parameters.

The IRMA instrument, like any radiometer, provides meaningful results only if it calibrated with respect to a known radiometric source. Once calibrated, the IRMA signal can be converted to atmospheric flux using the atmospheric model. Thus, both the instrument and the atmospheric model have associated uncertainties that can propagate through to the final PWV value. The uncertainties associated with the atmospheric model are discussed in detail in Chapter 4; those associated with the radiometer are discussed in Chapter 5. Chapter 5 describes the procedures developed to calibrate and account for stray radiation within the IRMA instrument. The thesis concludes with an intercomparison of three units to illustrate the effectiveness of the calibration procedure.

1.7 Summary

The IRMA instrument is being used to measure PWV to aid in the assessment of candidate sites for the TMT site selection committee. The presence of water vapour in the atmosphere severely limits terrestrial astronomy in the far-infrared and submillimetre spectral regions. Sites with low PWV are favoured for installation of astronomical instrumentation. In the next chapter, the TMT project will be described, and the characteristics of an ideal astronomical observing site will be discussed.

Chapter 2

Site testing for TMT

2.1 TMT overview

The Thirty Meter Telescope (TMT) project is an ambitious undertaking between the California Institute of Technology (Caltech), the University of California, and the Association of Canadian Universities for Research in Astronomy (ACURA), to construct the world's largest optical telescope within the next decade. The sheer size of TMT and its sensitivity to vibration provide obvious design obstacles, and represents a technological milestone in the eventual construction of the European Southern Observatory's (ESO) proposed 100 m diameter Overwhelmingly Large Telescope (OWL).

The initial suite of instruments and adaptive optics systems has been defined and conceptual designs are being developed. The project is currently testing sites to determine the best place to locate TMT. As part of this effort the University of Lethbridge (UL) has been contracted to provide IRMA instruments which have been deployed and are currently measuring the atmospheric opacity at several sites in Chile, Hawaii, and Mexico.

Figure 2.1: One mirror segment being poured for TMT (Photo Credit: Thirty-Meter Telescope Project)

The segmented nature of the primary mirror surface requires the use of active controls in order to maintain it's shape against external deforming forces such as gravity, thermal gradients, and wind. Furthermore, the control system will also incorporate the use of adaptive optics, a key feature of the telescope that will compensate for atmospheric turbulence and thus help to increase image quality.

TMT is scheduled to start construction in 2009, and achieve first light in 2016.

2.2 TMT science goals

At its core, TMT will be the largest and most sensitive optical telescope constructed to date, utilizing 738 mirror segments (see Figure 2.1) that stretch across its 30 m diameter. TMT will operate from the optical to the infrared regions of the electromagnetic spectrum, employing the latest technology in an attempt to answer some key questions in contemporary astronomy. TMT will seek to explore the beginnings of the early universe including the physics of the big bang — the emergence of the first stars and galaxies — the formation of stars and planetary systems — the detection of habitable planets and the possible signatures of life on extra-solar planets. TMT will be used in conjunction with space-based telescopes such as the Hubble Space Telescope's successor, the James Webb Space Telescope (JWST) scheduled to be launched in 2013.

TMT will operate in the $0.3-30$ μm spectral range, using a number of instruments each providing specialized observation capabilities to meet the scientific goals of the project. The first generation instrumentation consists of [22]:

- Infrared Imager and Spectrometer (IRIS)
- Wide Field Optical Imager and Spectrometer (WFOS)
- Near Infrared Multi-Object Spectrograph (IRMOS)
- Planet Formation Instrument (PFI)
- Mid Infrared Echelle Spectrometer (MIRES)
- Narrow Field Infrared Adaptive Optic System (NFIRAOS)

WFOS, PFI, and NFIRAOS are the Canadian contributions to the facility instrumentation.

2.3 Why build a 30 m telescope?

When designing an optical telescope there is a relationship between the diameter of the primary reflecting surface, the wavelength of light being measured, and the maximum spatial resolution provided by the telescope. This relationship is referred to as the angular resolution of the telescope. It determines the maximal spatial resolving power of any image forming device. Resolving power is the ability to measure the angular separation of unique points in an object. In the case of a single telescope, point-likes sources separated by an angle smaller than the angular resolution cannot be resolved. The angular resolution R of a single telescope can be approximated by equation 2.1:

$$R \approx \frac{\lambda}{D} \qquad \text{[radians]} \quad , \tag{2.1}$$

where λ is the wavelength of the observed radiation and D is the diameter of the telescope's objective or primary reflecting surface.

For near-IR radiation (λ ∼1000 nm, or 1.0 μm), a telescope primary mirror diameter of 30 m will give $\sim 3 \times 10^{-8}$ radians of angular resolution. This is equivalent to $\sim 3 \times 10^{-3}$ arcseconds* of angular resolution. By comparison, for far-IR radiation ($\lambda \sim 1$ mm), the 30 m diameter telescope will give ~ 7 arcseconds of angular resolution. To put these angular values in perspective, the full moon viewed from Earth is ~ 0.5 degrees, or 30 arcminutes, or 1800 arcseconds.

In order to maintain angular resolution at longer wavelengths, the effective diameter of the telescope must be increased, hence the use of interferometers like the Smithsonian Millimeter Array (SMA) in Hawaii, or the Atacama Large Millimeter Array (ALMA) planned for Chile. Equation 2.1 can also be used to calculate the angular resolution of an

*Note: 1 arcsecond is $\pi/(180 \times 60 \times 60) = 4.848 \times 10^{-6}$ radians

interferometer, in this case, however, the effective diameter, D, is replaced by the largest baseline of the interferometric array, B.

2.4 Site selection

One of the most important short-term goals of the TMT project is the selection of a site for the location of the telescope by the end of 2007. Six sites have been short-listed; these include four locations in the mountains of Northern Chile, one at San Pedro Martir, Baja California, Mexico, and one at Mauna Kea, Hawaii, USA. All of these sites are to be studied carefully to determine their scientific quality based upon such factors as winds, average cloud cover, turbulence, and water vapour content. The Astronomical Instrumentation Group at the University of Lethbridge has developed an Infrared Radiometer for Millimetre Astronomy (IRMA) that will be used by the TMT project as a PWV monitor. Three IRMA units have been constructed for TMT and are presently operating at the six potential sites. Data are being collected and subsequently analyzed to provide an accurate representation of the local atmospheric conditions at each potential site. The site will be chosen based upon an optimal blend of scientific quality and logistical considerations.

When selecting a site for a ground based observatory, it is important that ground based sources of light are minimal and that the sky is transparent within the spectral region of interest. Many universities have optical telescopes that were moderately useful 50 years ago. However, with the general expansion of urban landscapes, these same small-scale observatories now find themselves within areas completely overrun with light pollution. Another obstacle to observing is the opacity of the atmosphere itself. Naïvely, air is transparent (zero opacity) to visible light, thus we can see the sun, moon, stars, et cetera. However,

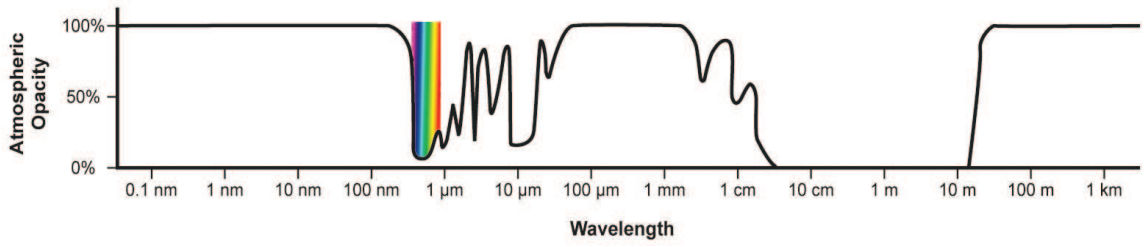

Figure 2.2: Atmospheric Opacity: Why Send Telescopes Into Space? - (Original figure courtesy of Jet Propulsion Laboratory, California Institute of Technology, Pasadena, California.)

this transparency does not apply to all regions of the electromagnetic spectrum, and hence the need for instruments to determine this opacity in regions beyond the limits of human vision. The atmosphere is teeming with species of molecules such as aerosols, gaseous water, liquid water, dimers of water, ice crystals, and varying partial pressures of component gases. Each of these molecules interacts with electromagnetic radiation according to the laws of quantum mechanics. As the optical thickness of the atmosphere increases, more of a specific frequency will be absorbed, until finally the atmosphere becomes completely opaque, effectively saturated at that frequency.

Ideally we would have nothing (no matter or medium) between us and the light we want to observe. This can be achieved by performing the measurement in space, above the Earth's atmosphere. There are both technical and economic difficulties associated with this option. Our next resort is to have a ground based observatory. The atmosphere blankets the earth with a thickness of roughly 16 km everywhere on its surface (thicker at the equator and thinner at the poles due in part to the Earth's rotation, and to solar insulation). To get a sense of the distribution of the atmosphere with respect to height, 50% of the atmosphere by mass is below 5.6 km, 90% by mass is below 16 km, and 99.99997% by mass is below 100 km [23]. By this logic, mountainous regions with base altitudes nearing 5.6 km will be

above 50% of the atmosphere, and notably water vapour which is the dominant source of opacity in the infrared spectral region.

For an atmosphere that is in both local thermal and hydrostatic equilibrium it can readily be shown that pressure and density decrease exponentially with height. Thus, with higher altitude comes lower pressure, as is observed by finding a continuously thinner atmosphere the further one is from the Earth's surface. The thinner the atmosphere the better for observing purposes, since thin implies lower density and therefore lower number of molecules per given volume, decreasing the probability of interaction between radiation and matter, resulting in less absorption/emission/scattering of the light. The logarithmic relationship between pressure and altitude is expressible as the law of atmospheres, also known as the barometric law:

$$\frac{p(z)}{p(0)} = e^{-z/H} \quad , \tag{2.2}$$

where p is pressure [mbar or Pa], z is altitude [m], and H is the scale height [m]. Thus, atmospheric density and pressure decrease by a factor of $1/e$ every time the altitude increases by one scale height. Scale height, H [m], is expressed as:

$$H = \frac{k_B\, T}{m\, g} \qquad [\mathrm{m}] \quad , \tag{2.3}$$

where k_B is Boltzmann's constant [$k_B = 1.3806503 \times 10^{-23}$ JK^{-1}], T is temperature [K], m is the mean molecular mass of the air particle [kg], and g is the acceleration due to gravity [ms^{-2}]. Molecular mass is defined as:

$$m = \frac{M}{N_A} \qquad [\mathrm{kg}] \quad , \tag{2.4}$$

where M is the molar mass [kg mol^{-1}, or atomic mass unit, u] and Avogadro's constant is $N_A = 6.022 \times 10^{23}$ mol^{-1}. By definition, one mole is the amount of substance that contains

as many elementary entities as there are atoms in 12 g of carbon-12 [10]. One mole of carbon-12 is 12.00000 grams. The atomic mass unit, u, is defined as 1/12 the mass of a carbon-12 atom, thus, carbon-12 is also 12.00000 u. For example, the average atomic mass of hydrogen is 1.00794 u, and oxygen is 15.9994 u. The molecular mass of water, H_2O, is 2×1.00794 u + 15.9994 u = 18.01528 u. Thus, one mole of water has a mass of 18.01528 g. Using Equation 2.4 gives the mean molecular mass of water as $m = 2.9916 \times 10^{-26}$ kg.

The mean molecular mass of dry air is 0.02896443 kg mol^{-1}. As mentioned above, the mean molecular mass of water is 0.01801528 kg mol^{-1}. If T = 260 K, the average temperature of the atmosphere, then Equation 2.3 results in H(dry air) = 7.6 km, and H(water) = 12.2 km. While the theoretical scale height of dry air agrees well with experimental measurements, the scale height of water as determined from radiosonde data in §4.5 is $\sim$ 0.3 — 2.1 km. This large discrepancy is due to the complexity of water and that it exists in three phases at atmospheric temperatures. This will be discussed further in Chapter 4.

At infrared wavelengths centred around the 20 μm region, the rotational spectral transitions of water vapour are the dominant features observed in our atmosphere [16]. IRMA is designed to measure directly this emission due to water vapour and via an atmospheric model infer the column abundance present along its line-of-sight.

The Earth offers many locations of extreme climate. A location offering a combination of these extremes would have the most favourable conditions for astronomical observing. For example, a desert might be selected for its local dryness, however, if the desert was at low altitude there would still be a relatively thick atmosphere overhead, and potentially a high quantity of water vapour above it. Or, a location found at high altitude

might not be appropriate due to high amounts of precipitation. The Atacama desert is located on a plateau at high elevation in the cold, desolate Andean tableland in northwestern Argentina and adjacent regions of Chile. It has the advantageous combination of being both high and dry. An extremely cold place, such as Antarctica, also has the benefits of being both very dry and quite high (∼3000 m). Antarctica is the driest place on Earth since most of the water in the atmosphere above has precipitated out. Elevation no longer becomes as important of a concern when there is little water vapour in the atmosphere. There are numerous challenges associated with situating an observatory in Antarctica, not the least of which are the extremely low temperatures, lack of infrastructure, geographical distance from major population centres, and maintenance of structures and equipment in the hostile, almost lifeless, environment, however, the benefits far outweigh the difficulties imposed by the location. In addition to being both high and dry, Antarctica has the added benefits of having 3+ months of continual darkness for observing. According to the 1994 report edited by M. Burton [24], the Antarctic plateau is the most favourable terrestrial site for astronomical development due to its dark sky, hyper-dry, steady, and clear air, minimal interference from man-made sources, and geographical considerations.

The goal of IRMA deployment at the proposed TMT sites is to measure PWV and determine the atmospheric opacity over a representative period of time. The long range plan is to present a historical archive of site specific water columnar abundance to aid in the decision making process for the TMT Site Selection Committee.

2.5 Summary

The scientific driver for building a large telescope is to have greater spatial resolution at longer wavelengths. The atmosphere is partially opaque at infrared wavelengths depending on the amount of precipitable water vapour present above the site. Sites with qualities that are beneficial to astronomic observing have low PWV and are often found to be at high altitude, thus above a large portion of the atmosphere. The next chapter will briefly introduce radiative transfer theory, spectroscopy, and its applications within atmospheric modeling.

Chapter 3

Introductory radiative transfer

3.1 Overview

Radiative transfer is defined as the process by which radiation passes through a medium that may contain any combination of scatterers, absorbers, and emitters. While the ancient Greeks began the process of reasoning known today as science, early work on radiative transfer began with Lord Rayleigh's investigations in 1871 on the nature of scattering by air molecules [25]. Simple radiative transfer was first formulated by Schwarzschild in 1906 in his work describing radiative equilibrium of a grey stellar atmosphere under conditions of local thermodynamic equilibrium (LTE) [26]. Since that time, sophisticated numerical solutions to radiative transfer problems have been developed, initially for single layer, and single wavelength applications. While seemingly inapplicable to our multi-layer multi-chromatic atmosphere, the simplicity of the single layer monochromatic case allows for fast computation when modeling atmospheres.

One of the simplest radiative transfer models is the Schwarzschild equation for a single atmospheric layer, with constant pressure, temperature and density, for one specific wavelength, effectively Beer's law [27] with emission taken into account. It it possible to expand this simple instance to represent a complex atmosphere where all of these parameters vary across the height of the atmosphere. This model would include many layers, and be computed over many wavelengths. Studying the effects of having multiple absorbers, can only be calculated assuming the interactions are independent from each other. Moreover, when determining the spectral emission from a molecule, it is necessary to account for contributions to emission away from the line centre which arise from the line profile.

This chapter will discuss the key points of radiative transfer, an introduction to molecular rotational spectroscopy, the characteristics of spectral line profiles, and the fundamentals of atmospheric modeling as applied to IRMA through the accurate simulation of test measurement sites.

3.2 Elements of radiometry

What follows is a brief introduction to the radiometric concepts employed with BTRAM and IRMA. A more thorough development can be found in references [1] and [3].

Radiometry is the precise measurement of an amount of electromagnetic radiation detected over a specified wavelength or frequency range expressed as radiant power in Watts. This radiation can be referred to in a variety of ways. Table 3.1 highlights the common radiometric terms and their associated units. All radiometric quantities can be *spectral*, meaning they are measured per unit wavelength or per unit wavenumber interval, denoted by subscript λ [m] or σ [cm^{-1}], respectively. Wavenumber, σ, as used in this the-

Table 3.1: Radiometric quantities and associated units

Radiometric Quantity	Symbol	Units
Spectral energy	E_σ	J $(\text{cm}^{-1})^{-1}$
Spectral power	Φ_σ	W $(\text{cm}^{-1})^{-1}$
Spectral intensity	I_σ	W sr^{-1} $(\text{cm}^{-1})^{-1}$
Spectral radiance	L_σ	W m^{-2} sr^{-1} $(\text{cm}^{-1})^{-1}$

sis, has units of cm^{-1}. The wavenumber was first used in the analysis of atomic spectra by Johannes Rydberg in the 1880's. Fourier Transform Spectroscopy (FTS) was proposed shortly thereafter, but was not fully developed until the 1950's with the advent of computers. Since a Fourier transform performed on data as a function of position [cm] yields a reciprocal spectrum [cm^{-1}], the wavenumber was found to be a convenient unit for this work. Wavenumber is proportional to inverse wavelength, and thus is the spatial analogue of frequency.

There is a natural progression between the following four radiometric quantities: energy, power, intensity and radiance. The first, spectral energy, E_σ, is the energy contained in the radiation field per unit wavenumber [J $(\text{cm}^{-1})^{-1}$]. Spectral power or flux, Φ_σ, is the spectral energy passing a fixed location per unit time [W $(\text{cm}^{-1})^{-1}$]. Spectral intensity, I_σ, is the spectral power per unit solid angle [W sr^{-1} $(\text{cm}^{-1})^{-1}$]. Lastly, spectral radiance, L_σ, is the spectral intensity per unit projected source area [W m^{-2} sr^{-1} $(\text{cm}^{-1})^{-1}$]. The concept of solid angle, Ω, measured in steradians, sr, is used to describe two-dimensional angular spans in three-dimensional space, analogous to the way in which the angle, θ, in radians, describes angles in a plane. A solid angle of 4π sr covers all directions, representing the full sphere of emission from an emitting point-source. For example, the sun radiates into a solid angle of 4π steradians.

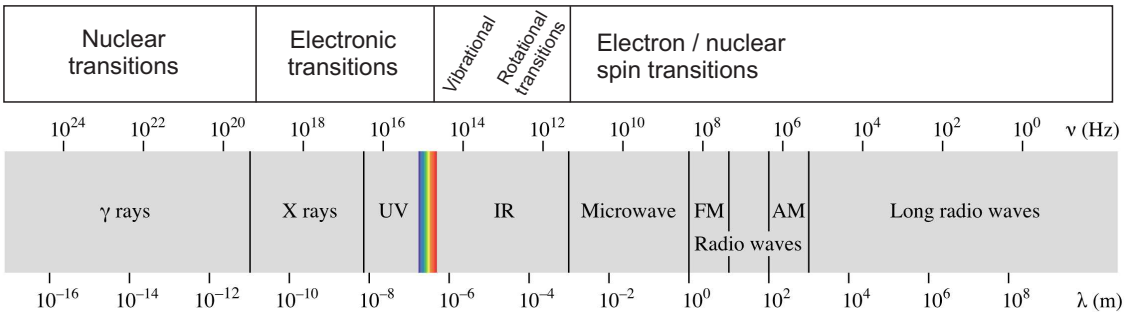

Figure 3.1: The electromagnetic spectrum and the types of transitions associated with each different energy/frequency range.

3.3 Introduction to spectroscopy

There are multiple ways that a molecule, atom, or ion can absorb and emit electromagnetic radiation, thus producing the measurable and unique spectrum of radiant energy versus frequency (or wavelength). In order of decreasing energy, the physical mechanisms leading to energy transitions include nuclear transitions (radioactivity/gamma radiation), electronic transitions (X-rays, ultraviolet, and visible radiation), vibrational transitions (near-infrared radiation), rotational transitions (far-infrared radiation), and electron/nuclear spin transitions (radio waves); see Figure 3.1. The energy associated with rotation of a molecule is much less than the energy associated with vibration. The frequencies at which a molecule will either rotate or vibrate will depend intrinsically on the masses and locations of the atoms in the molecule and the respective force constants in their chemical bonds. Heavier molecules require more energy to rotate and vibrate, so they tend to do both relatively slowly, at lower frequency. Lighter molecules require less energy to rotate or vibrate, so tend to do both more quickly, at higher frequency. Equation 3.1 shows the proportionality relationship between energy and frequency. A higher energy difference

translates directly to a higher frequency, and vice-versa.

Spectroscopy is the study of electromagnetic radiation and its frequency dependent interactions with matter. It is a method of determining the chemical composition of materials by looking at their spectrum either in emission or absorption. Through this, spectroscopy can be used to determine the composition and physical conditions of distant stars and galaxies. While spectroscopic observations at visible wavelengths can be used to identify atoms, in the case of molecules, the infrared region, also known as the fingerprint region provides a far more powerful diagnostic capabilities due to the complexities of the allowed rotational and vibrational transitions.

Atoms in their ground state can be excited (have an electron increase its quantum number) through the addition of unique and discrete amounts of energy. For each of these specific transitions there will be an associated photon of fixed frequency with exactly the energy required. The same processes also work in reverse. An electron dropping from an upper excited state, E_{n}, to a lower state, E_{m}, will emit a quantum of energy as a photon of a given frequency, described by:

$$\Delta E_{\mathrm{nm}} = E_{\mathrm{n}} - E_{\mathrm{m}} = h\,\nu = h\,c\,\sigma \qquad [\mathrm{J}]\ , \tag{3.1}$$

where ΔE_{nm} is the photon energy [J], $h = 6.626068 \times 10^{-34}$ [$\mathrm{m^2\ kg\ s^{-1}}$] is Planck's constant, ν is the photon frequency [$\mathrm{s^{-1}}$], $c = 2.9979 \times 10^{8}$ [$\mathrm{m\ s^{-1}}$] is the speed of light in a vacuum, and σ is wavenumber [$\mathrm{cm^{-1}}$].

This difference in rates of rotation and vibration serves to separate, spectrally, lighter molecules from heavier ones. For example, a heavy molecule will have a larger reduced mass, and thus larger moment of inertia I, resulting in a smaller spacing between adjacent rotational energy levels, i.e. the energy levels will be more densely packed than

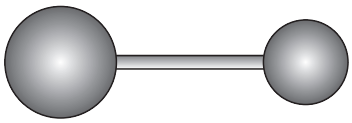

Figure 3.2: A diatomic molecule.

those of a lighter molecule. Water, being one of the lightest rotators commonly present in our atmosphere, has rotational energy levels with large interlevel spacing, leading to rotational transitions at higher frequencies. Indeed frequencies at or above which other common atmospheric molecules do not have any measurable rotational transitions because the associated states are not populated. Moreover, the rotational transitions of water occur around 20 μm, just below the energy levels where molecules begin to exhibit their vibrational transitions. For this reason, 20 μm is the ideal spectral region to measure water vapour. As an aside, 20 μm also happens to be near the peak of the Planck curve for atmospheric temperatures, discussed in §3.6.

For a molecule to have allowable rotational transitions, it must possess a permanent electric-dipole moment [27]. For this reason, symmetric molecules, such as O=C=O, or homopolar molecules, such at N_2, have no pure rotational transitions. A molecule can also have a permanent magnetic-dipole moment, but transitions attributed to the magnetic-dipole are much weaker [27].

3.3.1 Rotational spectroscopy

Water is an asymmetrical molecule requiring a complex model for spectroscopic analysis. Thus, rather than introducing the concepts of rotational spectroscopy using water I have chosen carbon monoxide (CO), a simple diatomic molecule possessing rotational transitions, which also happens to be is present in the Earth's atmosphere. CO is a het-

eronuclear diatomic molecule, as depicted in Figure 3.2. In quantum mechanics, the simplest approximation for the rotation of a diatomic molecule is obtained through the linear rigid rotor model. The term rigid is used here because it is assumed that the connection between the masses is both inflexible and massless, implying no vibration or significant contribution to the moment of inertia of the system. The reduced mass for a linear rigid rotor is given as:

$$\mu = \frac{m_1\, m_2}{m_1 + m_2} \qquad [\text{kg}] \ , \tag{3.2}$$

where m_1 and m_2 are point masses. This model can be used to predict the rotational energy levels, $E(J)$, of a diatomic molecule using only the measured atomic masses and their separation. Rotational energy depends primarily on the moment of inertia of the molecular system. The moment of inertia, I, of any molecule about any axis through the centre of gravity is [28]:

$$I = \sum_i m_i\, r_i \qquad [\text{kg m}^2] \ , \tag{3.3}$$

where m_i and r_i are the mass and distance of the i^{th} atom with respect to the centre of gravity of the system. For a diatomic molecule, Equation 3.3 reduces to:

$$I = \mu\, R^2 \qquad [\text{kg m}^2] \ , \tag{3.4}$$

where μ is the reduced mass of the molecule and R is the internuclear separation.

The angular momentum for this simple rigid rotor model is given by [27]:

$$P_J = \sqrt{J\,(J+1)}\,\hbar \qquad [\text{J s}] \ , \tag{3.5}$$

where J is a rotational quantum number ($J = 0, 1, 2, ..$), and $\hbar = h/2\pi$ where h is Planck's constant. Due to the space quantization of rotational angular momentum, the z component

of P_J is given by [27]:

$$(P_J)_z = M_J \hbar \qquad [\text{J s}] \quad , \tag{3.6}$$

where $M_J = J, J-1, ..., -J$. As a result, the degeneracy of each rotational energy level is $2J+1$.

It is possible to describe the space and time-dependence of a non-relativistic, quantum mechanical system using the Schrödinger equation. It is the quantum mechanical analogue of Newton's second law of motion, $\vec{F} = m\,\vec{a} = \dfrac{\mathrm{d}(m\vec{v})}{\mathrm{d}t}$. Solving the Schrödinger equation for the linear rigid rotor system results in a quantized formulation for the rotational energy given by Equation 3.7 [29]:

$$E(J) = \frac{h^2}{8\,\pi^2\,I}\,J\,(J+1) \qquad [\text{J}] \quad . \tag{3.7}$$

The rotational constant, B, and term value, $F(J)$, are defined as follows:

$$B = \frac{h}{8\,\pi^2\,c\,I} \qquad [\text{cm}^{-1}] \quad , \tag{3.8}$$

$$F(J) = \frac{E(J)}{h\,c} = B\,J\,(J+1) \qquad [\text{cm}^{-1}] \quad , \tag{3.9}$$

where J is the rotational quantum number.

The rotational constant of a molecule depends solely on the moment of inertia of the molecule. This unique dependence of B on reduced mass and bond length, allows for the identification of differing masses by analysis of subtle differences in the transition frequencies of isotopically substituted species. The isotope with heavier mass will have slightly lower rotational energy levels than its non-isotopic sibling. Through this relation, with a knowledge of the internuclear separation, measurements of B allow for the precise determination of the reduced mass of a molecule, and represents a very powerful structural diagnostic and isotopic identification technique.

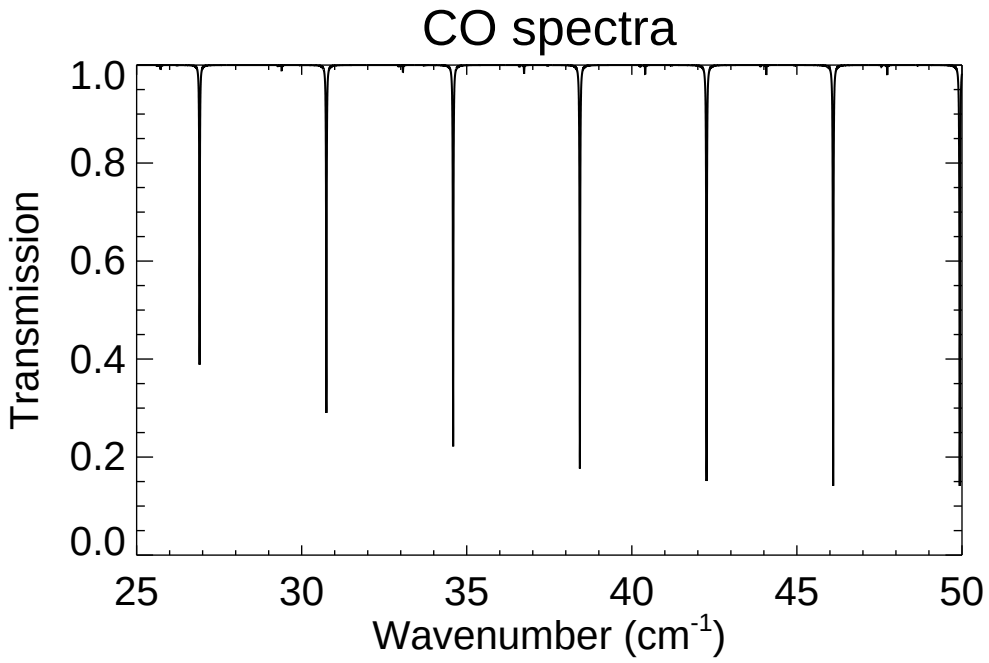

Figure 3.3: Simulated rotational spectrum for 10 kPa of CO and its isotopes at 273.15 K, in a 0.1 m gas cell, for $\sigma = 25$ — 50 cm^{-1}, at 0.001 cm^{-1} resolution.

Although Equation 3.7 specifies the rotational energy levels in Joules, in practice, frequencies are measured as opposed to energies. For this reason, energy levels, $E(J)$, can be converted to term values, $F(J)$, using Equation 3.9 with dimensions of either frequency or wavenumber, by dividing $E(J)$ by h or $h\,c$ respectively.

The moment of inertia of a molecule, I, is represented by a tensor of rank 2. Geometrically, I is defined by three mutually orthogonal axes A, B, and C, whose origin is at the centre of mass of the molecule. This is referred to as the principle axis system [27]. A diatomic molecule can be oriented in such a way that, due to symmetry, two components of I are equal, i.e. $I_A = I_B \neq I_C$. This symmetry leads to a relatively simple set of rotational transitions, as shown in the simulated spectrum of CO in Figure 3.3. The spectrum shown includes typical CO, $^{12}C^{16}O$, and three isotopes, $^{13}C^{16}O$,$^{12}C^{17}O$, and

$^{12}C^{18}O$. The transmittance plots were made with BTRAM v.3.3, using a simulated gas cell of length $\ell = 0.1$ m, temperature $T = 273.15$ K, and pressure $P = 10$ kPa. The spectral range was set to 25 — 50 cm^{-1} (400 — 200 μm), with a resolution of 0.001 cm^{-1}.

3.3.2 Transition energies and frequencies

The rotational energy levels for $^{12}C^{16}O$ can be computed for $J = 8$, 9, and 10 using Equation 3.7. The calculation requires the following set of parameters: mass of ^{12}C = 12.000000 [g mol^{-1}], mass of ^{16}O = 15.994915 [g mol^{-1}] [30], and bond length $R = 1.1283$ Å. Conversion from units of [g mol^{-1}] to [kg] involves first conversion from [g] to [kg], then division by Avogadro's number, $N_A = 6.022 \times 10^{23}$ [mol^{-1}]. Having calculated the reduced mass and moment of inertia from the above parameters, the resulting rotational energy levels are:

$$E(J) = 3.83645 \times 10^{-23} \times J(J+1) \quad [\text{J}] \quad ,$$

$$E(8) = 2.76224 \times 10^{-21} \quad [\text{J}] \quad ,$$

$$E(9) = 3.45281 \times 10^{-21} \quad [\text{J}] \quad ,$$

$$E(10) = 4.22010 \times 10^{-21} \quad [\text{J}] \quad .$$

Figure 3.4 shows how the rotational energy levels increase (and diverge) with increasing rotational quantum number. The rotational energy levels can also be expressed as wavenumbers by using Equation 3.9:

$$F(8) = 139.056 \quad [\text{cm}^{-1}] \quad ,$$

$$F(9) = 173.820 \quad [\text{cm}^{-1}] \quad ,$$

$$F(10) = 212.447 \quad [\text{cm}^{-1}] \quad .$$

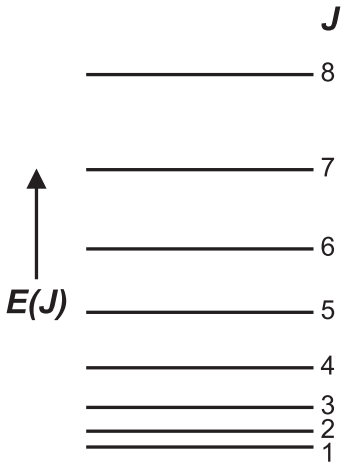

Figure 3.4: A set of rotational energy levels $E(J)$ for increasing rotational quantum number, J.

The difference between energy levels when expressed as term values, $F(J)$, gives the frequency of the spectral transition, $\sigma(J+1 \rightarrow J)$. The spacing between the transitions is an integer multiple of twice the rotational constant, $2B$:

$$\sigma(J+1 \rightarrow J) = F(J+1) - F(J) = 2\,B\,(J+1) \qquad [\mathrm{cm}^{-1}] \quad , \tag{3.10}$$

Thus, using Equation 3.10 and the $F(J)$ results above, it is possible to determine the frequency of the spectral transitions, for example:

$$\sigma(9 \rightarrow 8) \quad = F(9) - F(8) = 173.820 - 139.056 = 34.764 \quad [\mathrm{cm}^{-1}] \quad , \tag{3.11}$$

$$\sigma(10 \rightarrow 9) \quad = F(10) - F(9) = 212.447 - 173.820 = 38.627 \quad [\mathrm{cm}^{-1}] \quad . \tag{3.12}$$

The accepted frequencies* for these transitions are 34.58467 and 38.42610 cm^{-1} from the JPL spectral database [31]. The reason for the discrepancy between these values is that the initial assumption of a rigid rotor is incorrect. As rotational energy increases, the bond length varies as a function of rotational energy. Correcting this requires the addition of

*Uncertainty for these two values are on the order of 10^{-8} cm^{-1}.

higher-order distortion terms to the rotational energy expression:

$$F(J) = B\,J\,(J+1) - D\,(J\,(J+1))^2 + H\,(J\,(J+1))^3 + L\,(J\,(J+1))^4 ... \ , \tag{3.13}$$

where D, H and L are distortion constants [27]. For the case of CO, including the first distortion constant, $D = 6.12108375 \times 10^{-6}$ cm^{-1} [27], along with the rotational constant for the vibrational ground state, $B = 1.92252869$ cm^{-1} [27], the results are as follows:

$$\sigma(J+1 \rightarrow J) = 2\,B\,(J+1) - 4\,D\,(J+1)^3 \qquad [\text{cm}^{-1}] \ , \tag{3.14}$$

$$\sigma(9 \rightarrow 8) = 34.58767 \qquad [\text{cm}^{-1}] \ , \tag{3.15}$$

$$\sigma(10 \rightarrow 9) = 38.42609 \qquad [\text{cm}^{-1}] \ . \tag{3.16}$$

Adding the first distortion term reduced the difference between the accepted and calculated value for $\sigma(9 \rightarrow 8)$ for CO from $0.519\% \rightarrow 0.00867\%$. Further reduction is possible by including the higher order correction terms.

The $2B$ spacing is observed between transitions for the same isotope, shown as the horizontal black, red, blue, and green lines in From Figure 3.5. The spacings are different for each isotope, due to the differences in the rotational constant, B, for each isotope.

Having examined the transition properties of a diatomic molecule, let us turn our attention to water. A water molecule possesses none of the symmetry that allowed CO to have such a simple rotational spectrum. Water is an asymmetric top, meaning $I_A \neq I_B \neq I_C$, resulting in the complicated set of rotational transitions shown in the simulated water vapour spectrum in Figure 3.6.

Table 3.2: Transition data for CO and its isotopes from the JPL molecular spectroscopy catalogue [31].

```
          28001  CO
   26.90701 0.00000 -2.6716 2   80.7354 15 -28001 101 7           6
   30.74793 0.00000 -2.5590 2  107.6424 17 -28001 101 8           7
   34.58767 0.00000 -2.4751 2  138.3904 19 -28001 101 9           8
   38.42610 0.00000 -2.4156 2  172.9780 21 -28001 10110           9
   42.26305 0.00000 -2.3773 2  211.4041 23 -28001 10111          10
   46.09839 0.00000 -2.3581 2  253.6672 25 -28001 10112          11
   49.93197 0.00000 -2.3561 2  299.7656 27 -28001 10113          12
          29001  C-13-O
   25.72393 0.00000 -2.7187 2   77.1850 15  29001 101 7           6
   29.39610 0.00000 -2.6034 2  102.9089 17  29001 101 8           7
   33.06719 0.00000 -2.5165 2  132.3050 19  29001 101 9           8
   36.73707 0.00000 -2.4535 2  165.3722 21  29001 10110           9
   40.40561 0.00001 -2.4115 2  202.1092 23  29001 10111          10
   44.07268 0.00001 -2.3881 2  242.5149 25  29001 10112          11
   47.73813 0.00001 -2.3816 2  286.5875 27  29001 10113          12
          29006  CO-17
   26.22750 0.00000 -2.6982 2   78.6962 15  29006 101 7           6
   29.97150 0.00000 -2.5841 2  104.9237 17  29006 101 8           7
   33.71438 0.00000 -2.4984 2  134.8952 19  29006 101 9           8
   37.45601 0.00000 -2.4369 2  168.6096 21  29006 10110           9
   41.19624 0.00001 -2.3965 2  206.0656 23  29006 10111          10
   44.93494 0.00001 -2.3748 2  247.2618 25  29006 10112          11
   48.67197 0.00001 -2.3702 2  292.1968 27  29006 10113          12
          30001  CO-18
   25.62611 0.00000 -2.7226 2   76.8914 15  30001 101 7           6
   29.28432 0.00000 -2.6071 2  102.5175 17  30001 101 8           7
   32.94147 0.00000 -2.5199 2  131.8018 19  30001 101 9           8
   36.59741 0.00000 -2.4567 2  164.7433 21  30001 10110           9
   40.25203 0.00001 -2.4143 2  201.3407 23  30001 10111          10
   43.90518 0.00001 -2.3906 2  241.5927 25  30001 10112          11
   47.55673 0.00001 -2.3837 2  285.4979 27  30001 10113          12

Legend:
  FREQ, ERR, LGINT, DR,  ELO, GUP, TAG, QNFMT,  QN',  QN"
(F13.4,F8.4, F8.4,  I2,F10.4,  I3,  I7,    I4,  6I2,  6I2)

FREQ:  Frequency of the line in cm^-1.
ERR:   Estimated or experimental error of FREQ in cm^-1.
LGINT: Base 10 logarithm of the integrated intensity in units of nm^2 MHz at 300 K.
DR:    Degrees of freedom in the rotational partition function
ELO:   Lower state energy in cm^{-1} relative to the ground state.
GUP:   Upper state degeneracy.
TAG:   Species tag or molecular identifier.
QNFMT: Identifies the format of the quantum numbers
QN':   Quantum numbers for the upper state.
QN":   Quantum numbers for the lower state.
```

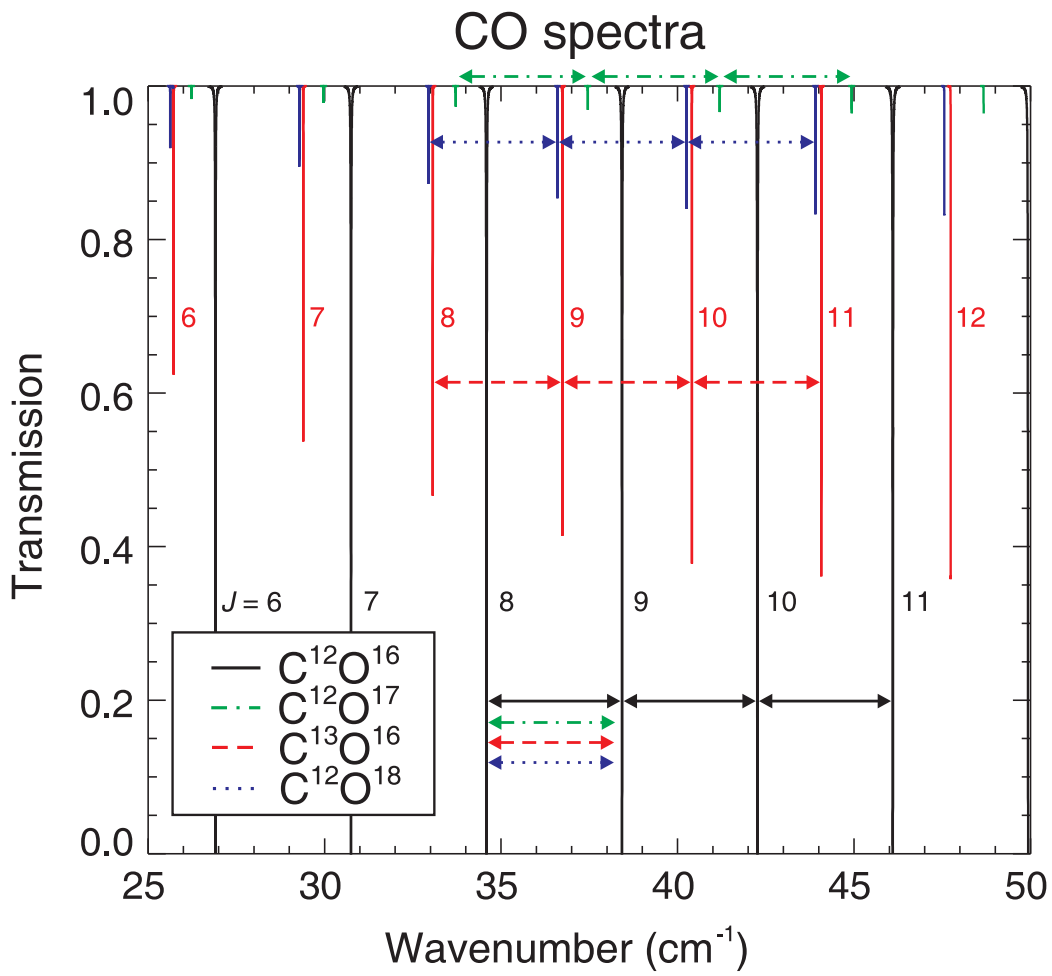

Figure 3.5: Detailed rotational spectrum for 1 kPa of CO at 273.15 K, in a 5 m gas cell, for $\sigma = 25$ — 50 cm^{-1}, at 0.0001 cm^{-1} resolution.

3.3.3 Transition intensities

Knowing the frequency at which a rotational transition occurs is only one part of the puzzle. The intensity of each transition must also be known to accurately simulate the rotational spectrum of a given molecule. Transition intensity is proportional to the Einstein A_{nm} coefficient and depends on the population of the upper state, N_n, of a transition [27]. Emission and absorption and their relationships with the Einstein coefficients will be discussed in the following section.

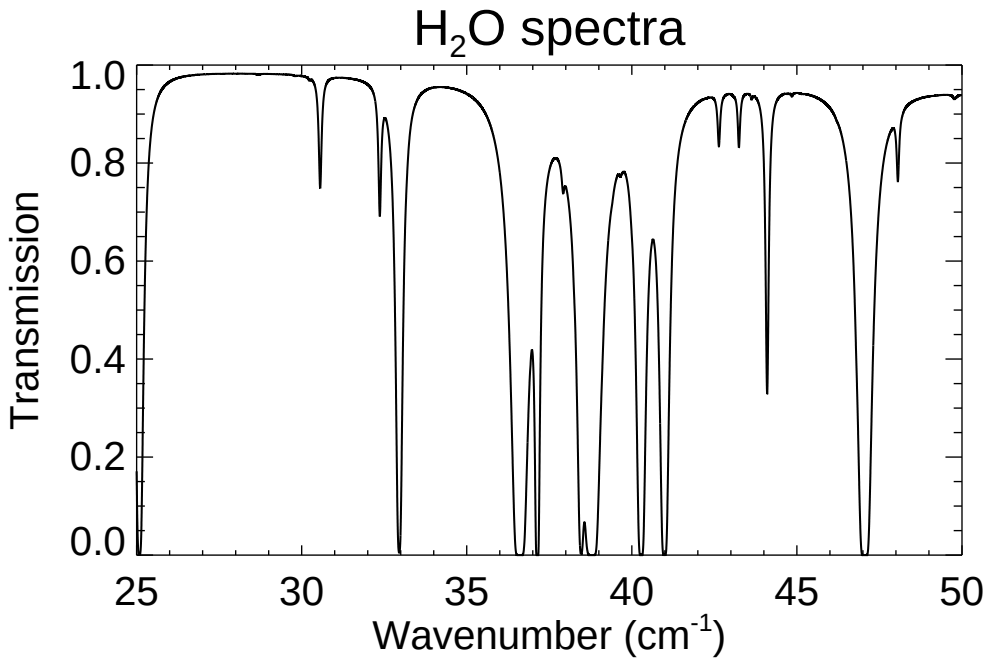

Figure 3.6: Simulated rotational spectrum for 10 kPa of H_2O and its isotopes at 273.15 K, in a 0.1 m gas cell, for $\sigma = 25$ — 50 cm^{-1}, at 0.001 cm^{-1} resolution.

3.3.4 Transitions and Einstein coefficients

There are three processes through which energy can be exchanged between two time-independent states, where E_n represents an upper excited state, and E_m represents a lower state. These three processes are induced absorption, spontaneous emission, and induced or stimulated emission. In induced absorption, an atom absorbs a quantum of radiation and is excited from the m to n state. The rate of change of population N_n of state n due to induced absorption is expressed as:

$$\frac{dN_n}{dt} = N_m \, B_{mn} \, \rho_\sigma(T) \qquad [\mathrm{s}^{-1}] \quad , \tag{3.17}$$

where B_{mn} is an Einstein coefficient, and $\rho_\sigma(T)$ is the spectral energy density whose dependence on wavenumber and temperature is given by [27]:

$$\int \rho_\sigma(T)\, d\sigma = \int \frac{8\,\pi\,h\,c\,\sigma^3}{\exp\left(\dfrac{h\,c\,\sigma}{k_B\,T}\right) - 1}\, d\sigma \qquad [\text{J m}^{-3}] \quad . \tag{3.18}$$

The spectral energy density function is geometrically related to the Planck function, $B_\sigma(T)$, given by Equation 3.42 to be discussed in §3.6, by:

$$\int \rho_\sigma(T)\, d\sigma = \int \frac{4\pi}{c} B_\sigma(T)\, d\sigma \qquad [\text{J m}^{-3}] \quad . \tag{3.19}$$

Induced or stimulated emission has a similar expression for population change, given by:

$$\frac{dN_n}{dt} = -N_n\, B_{nm}\, \rho_\sigma(T) \qquad [\text{s}^{-1}] \quad , \tag{3.20}$$

where B_{nm} is the Einstein coefficient for this process, with $B_{nm} = B_{mn}$. Spontaneous emission has no dependence on the spectral energy density term, it is given by:

$$\frac{dN_n}{dt} = -N_n\, A_{nm} \qquad [\text{s}^{-1}] \quad , \tag{3.21}$$

where A_{nm} is the Einstein coefficient associated to spontaneous emission. A_{nm} is also related to the natural spectral line broadening mechanism to be discussed in §3.4.

In any given situation all three processes are possible. For a system that has reached equilibrium, the net change in population can be expressed as:

$$\frac{dN_n}{dt} = (N_m - N_n)\, B_{nm}\, \rho_\sigma(T) - N_n\, A_{nm} \qquad [\text{s}^{-1}] \quad , \tag{3.22}$$

At equilibrium, the populations of N_n and N_m are related through the Boltzmann distribution as:

$$\frac{N_n}{N_m} = \frac{g_n}{g_m} \exp\left(-\frac{\Delta E_{nm}}{k_B\,T}\right) \quad , \tag{3.23}$$

where g_n and g_m are the degeneracies of states n and m. Through substitution of Equations 3.18 and 3.23 into Equation 3.22, one can express A_{nm} in terms of B_{nm}:

$$A_{nm} = 8\,\pi\,h\,c\,\sigma^3\,B_{nm} \qquad [\mathrm{s}^{-1}] \quad . \tag{3.24}$$

Equation 3.24 shows that spontaneous emission increases rapidly relative to induced emission as σ increases. The operation of lasers is based entirely on induced emission, this equation shows the process of lasing is more readily achievable for lower frequency radiation. The first lasers were referred to as masers, since they operated at lower, microwave frequencies.

Having described the Einstein coefficients and their role in emission and absorption processes, they have yet to be associated with transition intensity. This is done through the transition moment, $\mathbf{R}^{nm}$. The transition moment is a vector quantity expressed as:

$$\mathbf{R}^{nm} = \int \psi_n^*\,\vec{\mu}\,\psi_m\,d\tau \qquad [\mathrm{C\ m}] \quad , \tag{3.25}$$

where ψ_n and ψ_m are the wavefunctions of the upper and lower states, and $\vec{\mu}$ is the electric dipole moment operator, $\vec{\mu} \equiv \sum_i q_i \mathbf{r}_i$, where q_i is the charge, and $\mathbf{r}_i$ is the position vector of the i^{th} particle. Transition intensity is proportional to the transition probability, which is the square of the transition moment. This transition probability is related to the Einstein B_{nm} coefficient through the following:

$$B_{nm} = \frac{8\,\pi^3}{(4\,\pi\,\epsilon_0)\,3\,h^2}|\mathbf{R}^{nm}|^2 \qquad [\mathrm{s}^{-1}\ \mathrm{J}^{-1}\ \mathrm{m}^3] \quad . \tag{3.26}$$

Transition intensity proportionality can thus be traced from $\vec{\mu}$ to $|\mathbf{R}^{nm}|^2$ to B_{nm} and finally to A_{nm}, the Einstein coefficient associated with spontaneous emission.

There are conditions, known as rotational selection rules, for which $\mathbf{R}^{nm}$ in non-zero, implying that the associated transition has a non-zero intensity. These rotational

selection rules state that a molecule must possess a permanent dipole moment ($\vec{\mu} \neq 0$), that $\Delta J = \pm 1$, and that $\Delta M_J = 0, \pm 1$. However, the selection rule related to ΔM_J only increases the degeneracy, as discussed in §3.3.1, in the presence of an external electromagnetic field. Thus, through these selection rules and the above formulations, it is possible to determine which transitions will exist. To determine the relative intensity of the transitions, in addition to the individual line strengths, the relative populations of the corresponding energy levels must be known.

3.3.5 Intensities and populations

In the case of emission, transition intensities are related to the population of the upper state of the transition. In the general case, the population N_i of the i^{th} level, relative to the ground state N_0, is given by the Boltzmann distribution which can be expressed as Equation 3.23. The Boltzmann distribution for energies is expressed as:

$$\frac{N_i}{N} = \frac{g_i \, e^{-E_i/k_B \, T}}{\sum\limits_i g_i \, e^{-E_i/k_B \, T}} = \frac{g_i \, e^{-E_i/k_B \, T}}{Z} \quad , \tag{3.27}$$

where E_i is the energy of the i^{th} state, T is temperature, g_i is the degeneracy of the state, N_i is the number of particles with the same E_i energy level. N is the total number of particles. The denominator is the partition function $Z = \sum\limits_i g_i \, e^{-E_i/k_B \, T}$. Z represents the sum of all states and is used to determine the probabilities of how the particles are partitioned amongst the different possible energies.

Equation 3.27 can be used to determine the population of the J^{th} rotational energy level. The degeneracy of the $J = 0$ ground state is 1, implying $g_J = 1$, while the degeneracy of the J^{th} level is $2\,J + 1$, implying $g_0 = 2\,J + 1$. The population of the J^{th} level relative to

the population in the ground state ($J = 0$) results from the ratio of N_J to N_0:

$$\frac{N_J/N}{N_0/N} = \frac{g_J\, e^{-E(J)/k_B\,T}/Z}{g_0\, e^{-E(0)/k_B\,T}/Z} \quad , \tag{3.28}$$

$$\frac{N_J}{N_0} = (2J+1)\, \exp\left(\frac{-\Delta E_{J\,0}}{k_B T}\right) \quad . \tag{3.29}$$

The factor of $(2J + 1)$ increases linearly with J, whereas the exponential term decreases rapidly. The resulting behaviour of the distribution is such that N_J/N_0 increases at low J values, until the exponential term dominates at higher J values, asymptotically returning N_J/N_0 to zero. The population has a maximum, and thus maximal intensity, at energy level $J = J_{\max}$, with integer value nearest to:

$$\frac{d(N_J/N_0)}{dJ} = 0 \ , \tag{3.30}$$

leading to

$$J_{\max} = \sqrt{\frac{k_B T}{2hB}} - \frac{1}{2} \ , \tag{3.31}$$

when B is expressed in units of frequency. Thus, from Equation 3.29, and the previous section on Einstein coefficients, the relative intensities of spectral lines have been shown to depend almost exclusively on temperature, and some intrinsic properties related to rotational selection rules, transition probabilities, and the Einstein B coefficients. Of these factors, all are independent of the environment except for temperature. This is important to note since §3.4 will described how the line width, and thus line shape, of a spectral transition depends upon the temperature and the pressure of the surrounding environment.

Thus far, only the transitions of a diatomic molecule have been explored and modeled. When the system of description is extended to include triatomic molecules the equations required become far more complicated. While water would seem to be a relatively simple molecule, the complexities arising from being a non-linear triatomic molecule are not

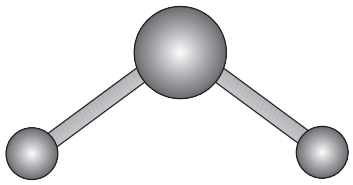

Figure 3.7: A non-linear triatomic molecule.

trivial. The reduced symmetry of a water molecule, expressed as $I_A \neq I_B \neq I_C$, result in the complicated set of rotational transitions shown in the simulated water vapour spectrum in Figure 3.6. It is due to this complexity that BTRAM [12] does not attempt to determine the frequencies or line strengths for water vapour rotational transitions from first principles. Instead, it relies upon the necessary frequency and line strength information catalogued in the HITRAN [15] molecular database for the water vapour transitions in the region defined by the parameters of the simulation.

In summary, the frequencies of the rotational transitions of a molecule can be calculated using Equation 3.13. The relative intensity of the transitions can be determined according to the energy level populations calculated using Equation 3.29 and from the transition probabilities. In practice, emission or absorption occur not at one frequency, but over a range of frequencies determined by broadening caused by conditions of the local environment, notably the temperature and pressure of the gas. This broadening, and the resulting spectral line profiles is described in the following section.

3.4 Line shapes

When measuring a spectral line with a spectrometer, many factors determine the shape of the observed line. These include natural characteristics, features of the physical environment (temperature and pressure), and instrumental effects. Ideally a molecule would emit all of its energy at a single frequency. However, in reality there are a number of factors that result in this emission being spread over a range of frequencies. Experimentally, absorption or emission features with infinitesimal line-widths are not observed. What is observed are continuous line profiles with well defined line shapes.

Lineshape functions can be of two general types; homogeneous, and inhomogeneous. A homogeneous lineshape occurs when all molecules in the system are interacted with equally, and thus have identical lineshapes, resulting in a Lorentzian profile. Inhomogeneous lineshapes are created by a set of molecules with lineshapes arising from non-identical interactions, resulting in a Gaussian profile [27].

Apart from instrumental effects, the three physical processes that determine the shape of a radiative transition are natural broadening, broadening due to temperature, and broadening due to pressure. The most fundamental of these mechanisms is natural broadening. This is a quantum mechanical property due to the Heisenberg uncertainty principle, expressed as [27]:

$$\Delta E \Delta t \leq \frac{\hbar}{2} \rightarrow \Delta t \leq \frac{\hbar}{2\Delta E} \rightarrow \Delta t \leq \frac{1}{4\,\pi\,\Delta\nu}\ , \tag{3.32}$$

This fundamental principle states that the product of the energy-time uncertainty is constant. The implication here is that an uncertainty in the time-occupation of an energy level, the lifetime, is directly translated into an uncertainty in that energy level. This ΔE

is equivalent to $\Delta\nu$ through Equation 3.1. Thus, a finite duration necessitates a spectral spread. The mean value of this duration is the inverse of the Einstein A_{nm} coefficient introduced in §3.3.4. Since all atoms of one species would exhibit this property equally, natural broadening is said to be homogeneous, and thus described by a Lorentzian profile; all spectral lines have this intrinsic shape. However, typical halfwidths of natural broadening for rotational transitions are on the order of 10^{-14} cm^{-1} which are challenging to measure in practice and can be neglected in this study [28].

The sources of broadening that must be considered in atmospheric modeling are due to environmental conditions, namely temperature and pressure. Doppler broadening is due to the statistical distribution of velocities of the atoms (or molecules) in the gas emitting radiation. Depending on whether the motion of each atom is towards or away from the observer, the associated photon it emits will either be red or blue-shifted by the Doppler effect, expressed as [28]:

$$\sigma \ = \sigma_0 \left(1 - \frac{v}{c}\right)^{-1} \qquad [\text{cm}^{-1}] \ , \tag{3.33}$$

where σ is the measured frequency of the transition, σ_0 is the actual frequency of the transition, v is the velocity of the atom, and c is the speed of light. Since the atomic velocities will exhibit a Maxwell-Boltzmann distribution, there will be a spread to σ, resulting in the spectral broadening. The higher the gas temperature, the wider the distribution of atomic velocities, thus the broader the emitted spectral line. Since each atom will have a unique velocity and thus emit a unique frequency photon, the overall effect of Doppler broadening is said to be inhomogeneous, resulting in the Gaussian line shape given by [28]:

$$f_D(\sigma - \sigma_0) = \frac{1}{\alpha_D}\sqrt{\frac{\ln 2}{\pi}} \exp\left[-\ln 2 \left(\frac{\sigma - \sigma_0}{\alpha_D}\right)^2\right] \qquad [\text{cm}^{-1}] \ , \tag{3.34}$$

$$\alpha_D \equiv \sigma_0 \sqrt{\frac{2 \ln 2 \; k_B T}{mc^2}} \qquad [\mathrm{cm}^{-1}] \quad , \tag{3.35}$$

where σ is frequency, σ_0 is frequency of the line centre, and α_D is the Doppler half-width at half-maximum (HWHM) width.

The other environmental factor which affects the line shape is pressure. Molecules in an atmosphere are not isolated, and therefore will collide with other molecules (or the boundary of the container if being studied in a gas cell.) Collisions broaden the spectroscopic linewidths by shortening the lifetime of the excited states. Again, this uncertainty in the time-occupancy of the energy levels (duration) translates to a spectral spread as it had for the natural broadening mechanism. This effect is homogeneous since at equilibrium all molecules are assumed to experience collisions caused by equal pressures, and thus have an identical pressure-broadened lineshape for a particular transition [27]. It is characterized by the Lorentz profile given by:

$$f_L(\sigma - \sigma_0) = \frac{1}{\pi} \frac{\alpha_L}{(\sigma - \sigma_0)^2 + \alpha_L^2} \qquad [\mathrm{cm}^{-1}] \quad , \tag{3.36}$$

$$\alpha_L \equiv \frac{1}{2\pi\tau} \qquad [\mathrm{cm}^{-1}] \quad , \tag{3.37}$$

where α_L is the Lorentz HWHM, and τ is the average lifetime of the excited state. The Lorentz width is only proportional to τ^{-1}, no other physical factors are involved. The fundamental difference between the Doppler and Lorentz profiles is in the shape of the wing structure, shown in Figure 3.8. The Doppler profile has a relatively large amplitude with narrow wings, while the opposite is true for the Lorentz profile. The Doppler and Lorentz line profiles both represent particular properties of the atmosphere. Each of them is dominant under different conditions. Lorentz dominates at lower altitudes, see Figure 3.9, where pressure is higher, and Doppler dominates at higher altitudes, where pressure is

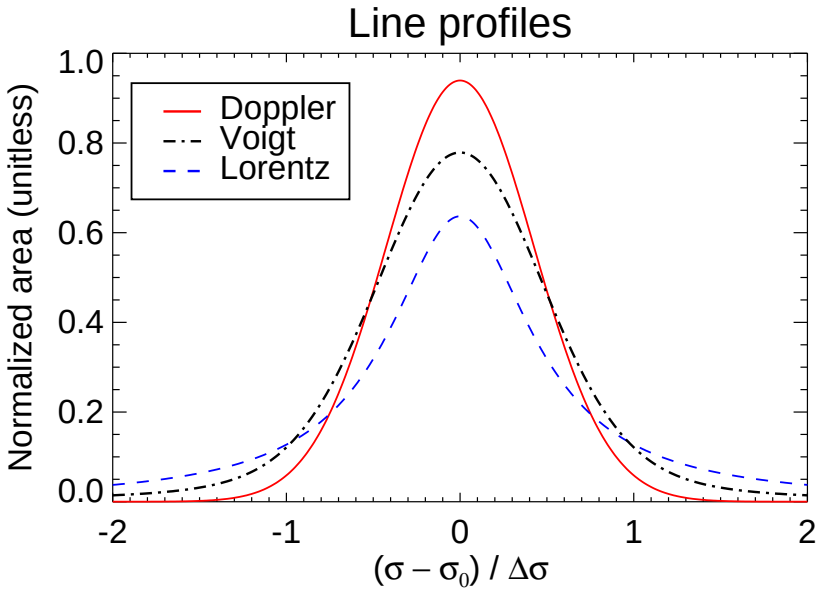

Figure 3.8: Doppler, Voigt and Lorentz profiles with normalized area and equal half-widths. The example Voigt profile represents an intermediate set of environmental conditions between the two extremes of temperature dependence and pressure dependence, represented by the Doppler and Lorentz profile respectively.

much lower.

To accommodate both the effects of temperature and pressure, the Voigt profile is frequently used [27]. The Voigt profile is a convolution of the Doppler and Lorentz profiles expressed as:

$$f_V(\sigma - \sigma_0) = \frac{1}{\alpha_D}\sqrt{\frac{\ln 2}{\pi}}\,\frac{y}{\pi}\int_{-\infty}^{\infty}\frac{\exp\left(-t^2\right)}{y^2+(x-t)^2}\,dt \qquad [\mathrm{cm}^{-1}]\ , \tag{3.38}$$

where the ratio of the Lorentz to Doppler widths is $y = \dfrac{\alpha_L}{\alpha_D}\sqrt{\ln 2}$, and $x = \dfrac{\sigma-\sigma_0}{\alpha_D}\sqrt{\ln 2}$ is related to the wavenumber scale in units of Doppler width. At the high pressure limit ($y \to \infty$), or low pressure limit ($y \to 0$), the Voigt profile asymptotically follows the Lorentz or Doppler profiles, respectively, as can be seen from its behaviour in Figure 3.9. The figure typifies the differences between Lorentzian and Doppler broadening effects as influenced by the conditions within our atmosphere. The Lorentz profile is dominant at low altitudes where the pressure is higher, whereas the Doppler profile dominates at higher altitude where

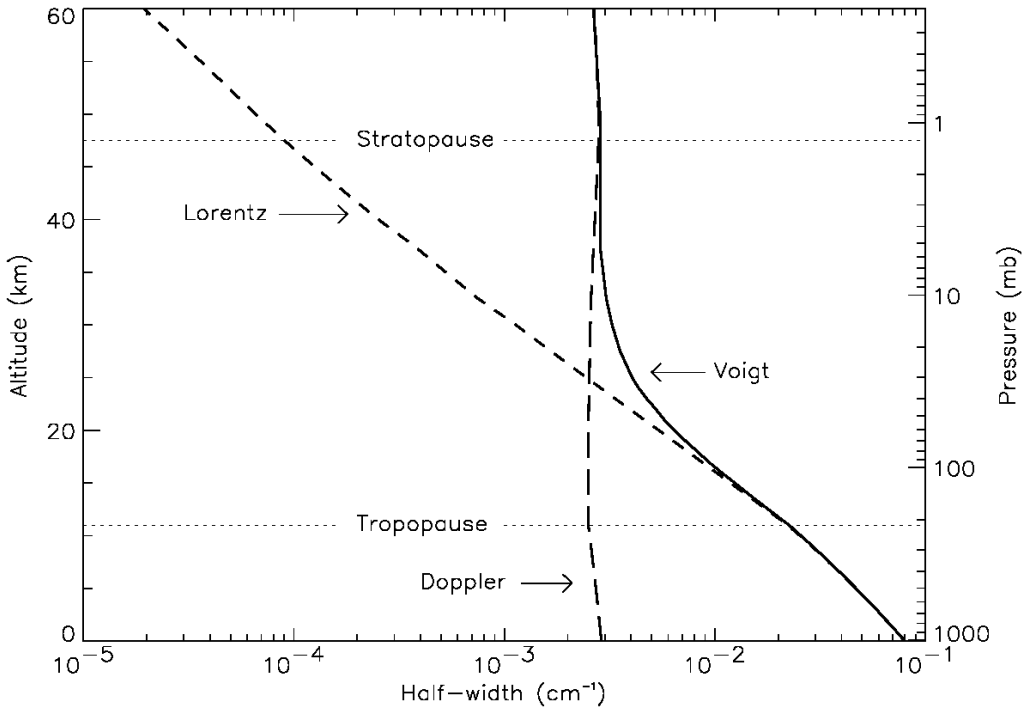

Figure 3.9: Approximate altitude dependence from 0 to 60 km of the Lorentz, Doppler, and Voigt half-widths for the 1976 U.S. Standard Atmosphere [32]. Figure from Larar *et al*, 2002 [33].

pressure is significantly reduced (>30 km). While this is a plot of the profile half-widths, it does show the overall relationship between the three profiles with respect to pressure and altitude in the case of the Earth's atmosphere.

Finally, the impact of the spectrometer itself needs to be considered when designing an experiment to measure the atmospheric emission spectrum. For example, measurement with a grating will add a rectangular instrumental line profile to the measurement, a Fabry-Perót interferometer (FPI) adds an Airy instrumental line profile [34], and a Fourier Transform Spectrometer (FTS) adds a sinc profile to the measurement [35].

In summary, the mechanisms that need to be included when considering the resultant form of a physical spectral line are: environment conditions (temperature and pressure), and instrumental effects. Line modeling requires knowledge of how and when each specific

process dominates. Conversely, through high resolution measurements of an isolated spectral line profile it is possible to deduce some of the physical conditions (P, T, ρ) of the emitting region in question.

3.5 Atmospheric Modeling

As our understanding of the dynamic processes that shape our environment grows, the better our position to predict, enact positive change, and prepare for the inevitabilities of the weather within our environment. Atmospheric modeling is an integral aspect of this process.

Detailed atmospheric modeling became possible with the advent of computers, particularly with the US Military and their simulating software FASCODE [13]. The purpose of the FASCODE simulation was to identify the characteristic spectral signatures of possible exhaust trails of aircraft, rockets, or missiles, with the intention of identification as friend or foe. For this to be possible they needed to understand the backdrop upon which they were trying to identify these specific features. Thus, the birth of modern atmospheric modeling. In order to accurately model an atmosphere many details must be known about its structure and composition, see Figure 3.10, specifically the relationships between temperature, pressure, density, mixing rations, and altitude. Atmospheric profiles can be created through statistical analysis of radiosonde data, described more fully in §4.3. Once the abundance of the molecules of species contributing to emission are known for a particular parcel of atmosphere, their spectral transitions can be calculated. This calculation requires parameters from a molecular database such as transition frequency, line strengths, air-broadened half-widths, and self-broadened half-widths. These parameters are contained

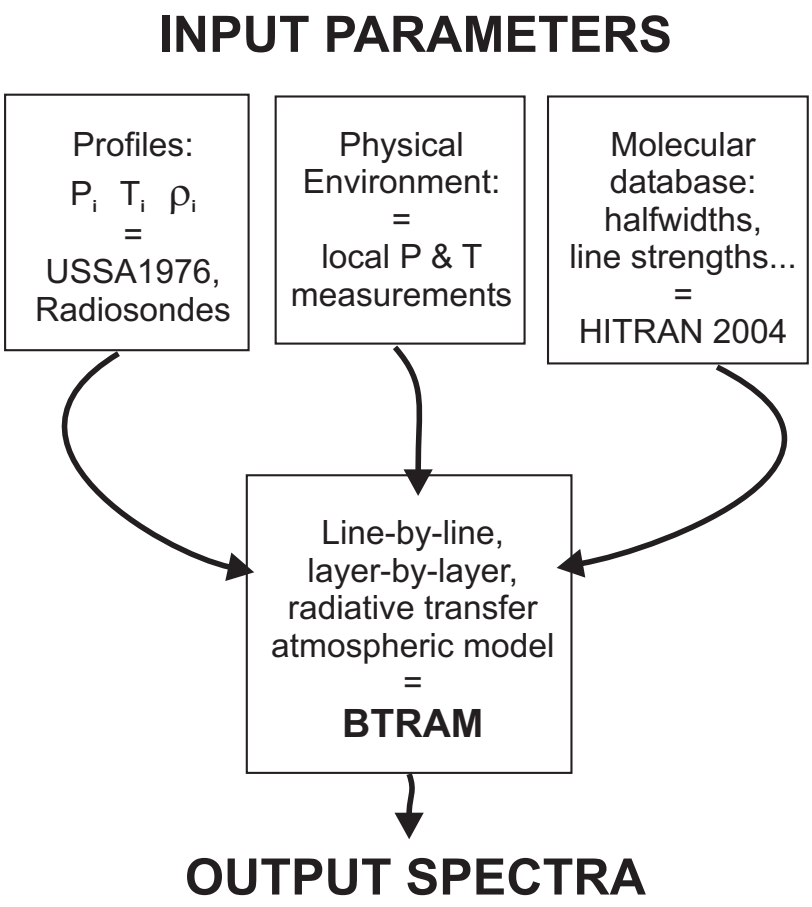

Figure 3.10: Input parameters and resources necessary for atmospheric modeling.

in HITRAN 2004 spectral line database [15]. With these three sets of information, the physical environment, atmospheric profiles, and the molecular database, it is possible to construct a relatively accurate representation of the atmosphere above any given location on the Earth.

The basis for relationships between pressure, temperature and altitude is the assumption of local hydrostatic equilibrium and thermal equilibrium expressed in the equations for the barometric law (Equation 2.2) and that of scale height (Equation 2.3). Hydrostatic equilibrium occurs when compression due to gravity is balanced by a pressure gradient

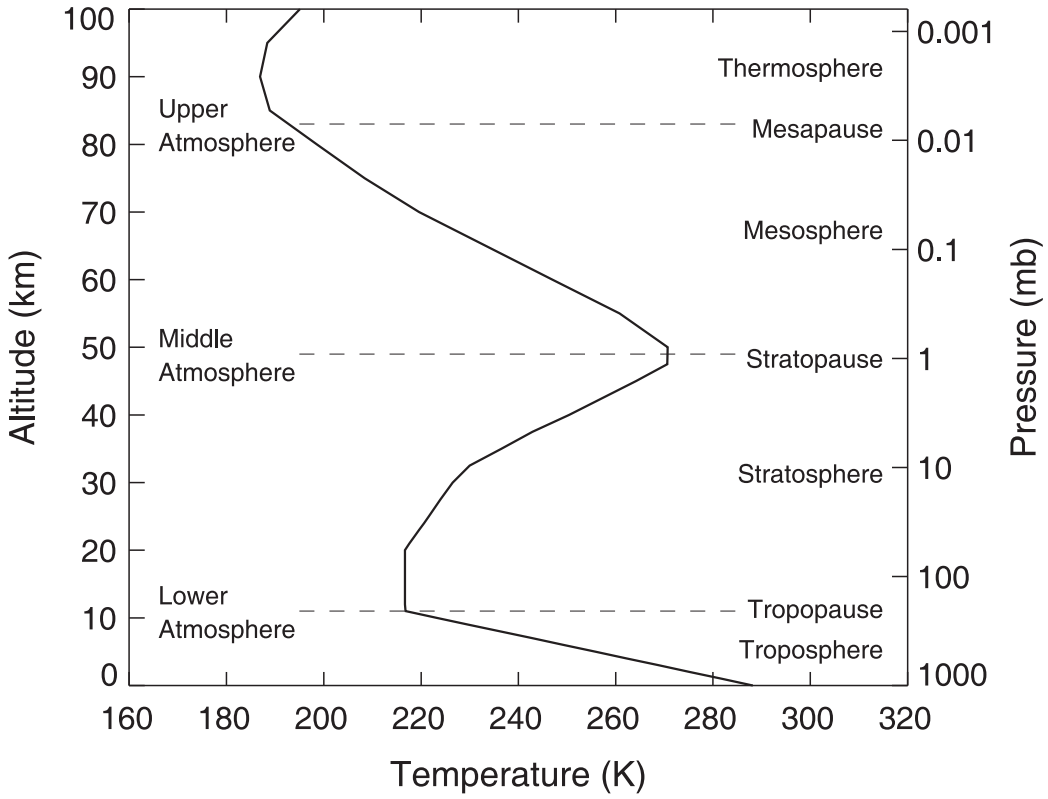

Figure 3.11: Temperature profile from the U.S. Standard Atmosphere 1976 [32]

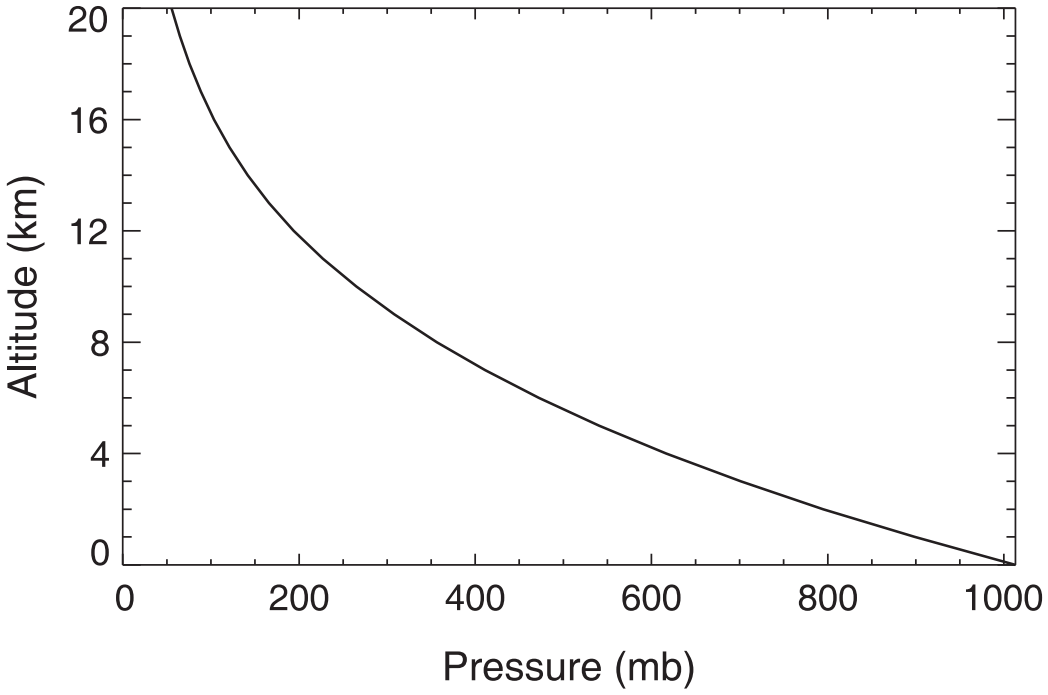

Figure 3.12: Pressure profile from the U.S. Standard Atmosphere 1976 [32]

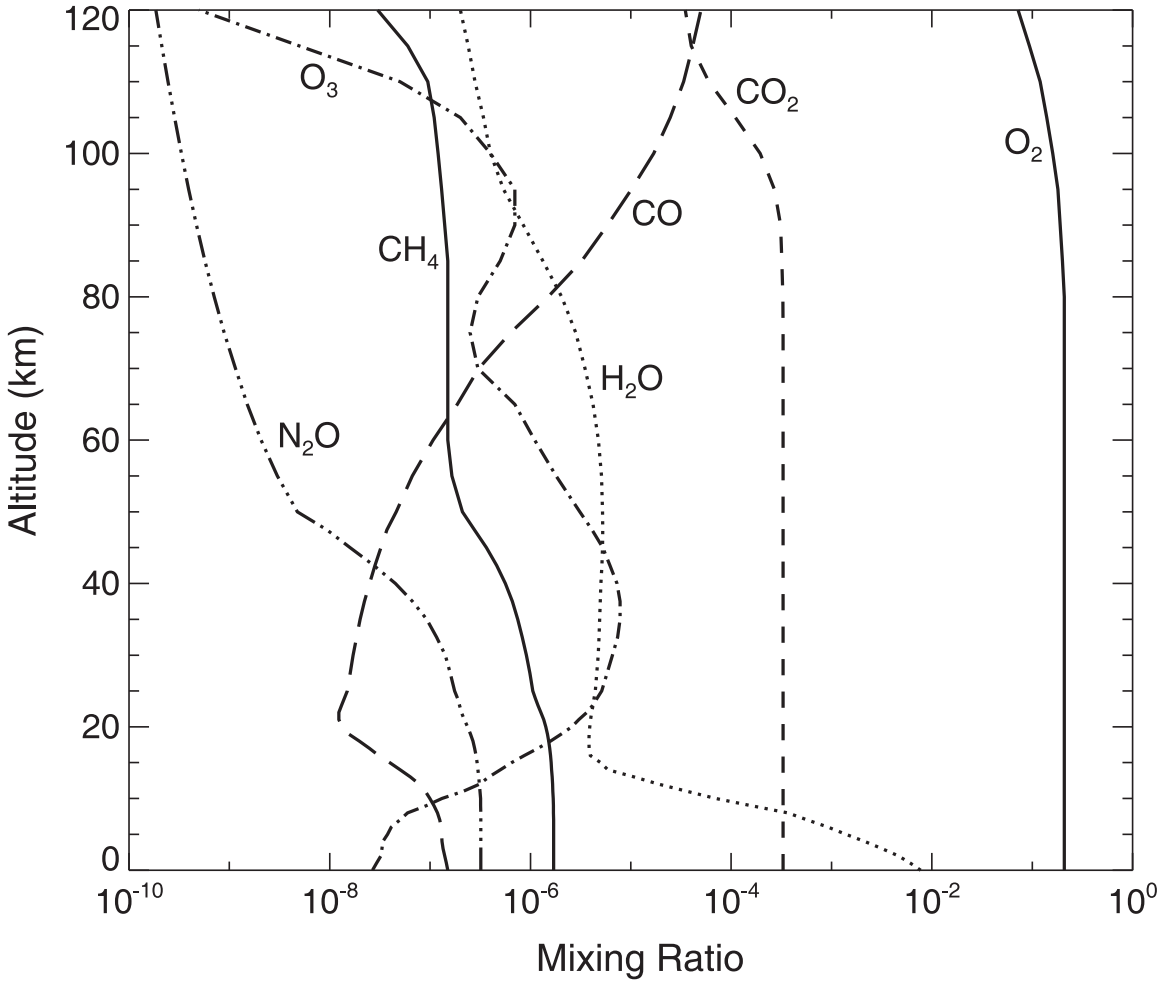

Figure 3.13: Representative vertical mixing ratios from the U.S. Standard Atmosphere 1976 [32]

force in the opposite direction. The balance of these two forces is known as the hydrostatic balance. When hydrostatic equilibrium is assumed, atmospheric processes become easier to manage and describe.

The U.S. Standard Atmosphere 1976 (USSA1976) temperature profile for Earth is shown in Figure 3.11. The USSA1976 pressure profile is shown in Figure 3.12.

The physical composition of molecules in the atmosphere, their relative abundances and their spatial distribution, as seen in the mixing ratio profiles in Figure 3.13, are necessary

for the accurate modeling of an atmosphere. This information is contained in a data set referred to as an atmospheric profile. FASCODE had pre-built seasonally specific profiles for a variety of latitudes [13]. The full list of FASCODE atmospheric profiles is listed in §1.4. The drawback to this approach is that generic profiles do not represent specific location to a sufficiently high level of detail possible with a custom created profile. Hence the need to create site specific profiles based on radiosonde data, as will be addressed in Chapter 4.

Now that the distribution and physical characteristics of the atmospheric layers is defined, it is necessary to deal with the properties of the molecules themselves. Spectral line data parameters are required to calculate the absorption/emission features of the molecules. A spectral database such as HITRAN 2004 Version 12.0 [15] offers this. It contains 1,734,469 spectral lines for 37 molecules including all their principle isotopes. All physical quantities and data for these spectral lines are documented for a temperature of 296 K and must be adjusted for typical atmospheric temperatures.

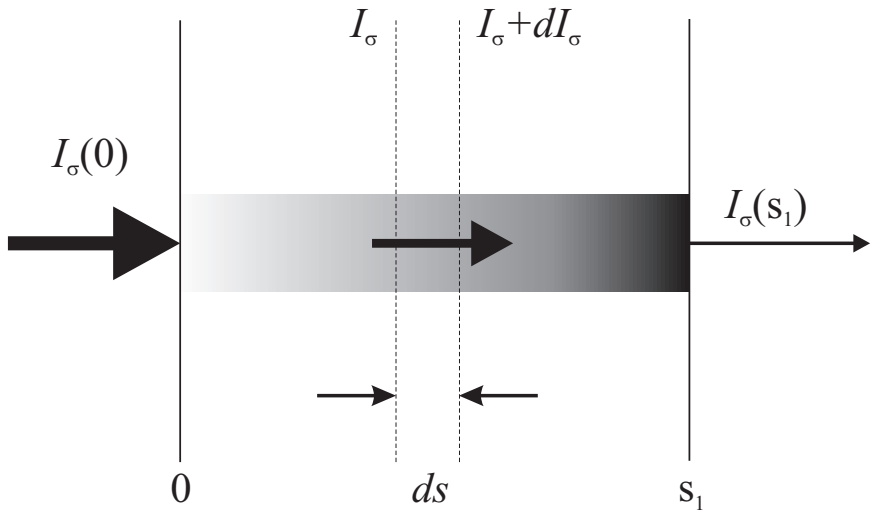

Figure 3.14: Depletion of the radiant intensity in traversing an extinction medium

3.6 Radiative transfer

As mentioned in §3.1, the simplest example of radiative transfer involves one layer composed of a single species, at constant P and T, irradiated by energy of a single frequency. From this simple foundation, the more complex form of a multi-layer, multi-wavelength, multi-species atmospheric model can be created, as is the case with BTRAM [12].

Figure 3.14, represents the general case of a single layer of well-mixed atmospheric medium with incident frequency dependent radiation, $I_\sigma(0)$, from a source on the left. As it passes through the atmospheric medium it will be modified by dI_σ over the interval ds. This modification can take the form of frequency specific absorption by the atmosphere, thereby reducing the incident radiation at those select frequencies. Or the modification can come from frequency specific emission from the atmosphere, thereby adding to the incident radiation at select frequencies. After this modification, the radiation leaves the atmosphere at s_1 and the observer on the right measures the out-coming radiation as $I_\sigma(s_1)$. Thus, the

resulting radiation exiting the atmosphere will be a combination of the absorption modified incident radiation and the emission of the atmosphere itself. The process outlined in Figure 3.14 is fully described by the Schwarzschild equation [36]:

$$I_\sigma(s_1) = I_\sigma(0)\, e^{-\tau_\sigma(s_1,0)} + \int_0^{s_1} B_\sigma(T_s)\, e^{-\tau_\sigma(s_1,s)}\, k_\sigma\, \rho\, ds \quad . \tag{3.39}$$

The first part of the equation represents the absorption due to the atmosphere over the interval $s = [0, s_1]$. This absorption is expressed here as a fractional transmission, $e^{-\tau}$, where τ is opacity, defined as:

$$\tau_\sigma(s_1, 0) = \int_0^{s_1} \sum_i k_{\sigma_i}\, \rho_i\, ds \quad , \tag{3.40}$$

where the integration range represents the distance through the medium, and the summation over i accounts for the i different atmospheric molecular species being included. The frequency dependent absorption coefficient is k_σ. The density of the absorber is given by ρ. Thus, the opacity of any given medium is expressed as the integral over the depth, or distance through a medium, of the absorber abundance, and the absorption coefficient.

The (mass) absorption coefficient of a spectral line can be expressed as:

$$k_\sigma = S\, f(\sigma - \sigma_0) \qquad [\mathrm{m}^2\ \mathrm{kg}^{-1}] \quad , \tag{3.41}$$

where S is the integrated absorption coefficient, or line strength, defined as $S = \int_0^\infty k_\sigma\, d\sigma$, σ_0 is the line center, and $f(\sigma - \sigma_0)$ is the normalized broadening profile discussed in §3.4.

In Figure 3.14, the increasing opacity of the medium is depicted as the gradually darkening band that starts as transparent, and ends at the right as black (opaque). The relative transmissions of the radiation in this simple case is shown graphically as the thickness of the arrows. Again, the amplitude of the incident radiation is high, gradually decreasing to the small amount of out-going radiation.

The second part of the Schwarzschild equation, Equation 3.39, represents the emission due to the atmosphere itself. The $B_\sigma(T_s)$ term represents atmospheric blackbody radiation. Blackbody radiation, described by the Planck function, refers to the spectral distribution of radiation emitted from matter at a given temperature [27]:

$$B_\sigma(T) = \frac{2\,h\,c^2\,\sigma^3}{\exp\left(\frac{h\,c\,\sigma}{k_B\,T}\right) - 1} \qquad [\text{W m}^{-2}\ \text{sr}^{-1}\ (\text{cm}^{-1})^{-1}] \quad . \qquad (3.42)$$

Figure 3.15 shows the Planck curve for several temperatures. These curves are continuous, however, in the case of emission from a gas, the Planck curve merely provides the maximal envelope that saturated emission could reach at any given frequency for any given temperature. The actual emission will be driven by the spectroscopic factors introduced in §3.3. Since, within the integral, the $B_\sigma(T)$ term acts as a broadband source of radiation, the spectral dependencies characteristic of the atmosphere must be applied. This is done with the spectrally dependent scaling factors: transmittance, $e^{-\tau}$, and absorption coefficient, k_σ.

To better demonstrate the properties of Equation 3.39, let us look at the two limiting examples: the optically thin case, $\tau \approx 0$, and the optically thick case, $\tau \gg 1$. For the case where the atmosphere is optically thin, the opacity terms would be negligible. Expansion of the integral in Equation 3.39 results in a $(1-e^{-\tau})$ term. If $\tau \to 0$, the integral also goes to 0, as $(1-e^{-\tau}) \to (1-e^{0}) \to (1-1) = 0$. Low opacity, implies negligible amounts of matter capable of absorbing/emitting, and therefore negligible atmospheric emission. The negligible absorption would not significantly reduce the incident radiation term either. As expected, when the atmosphere is optically thin one essentially sees right through it.

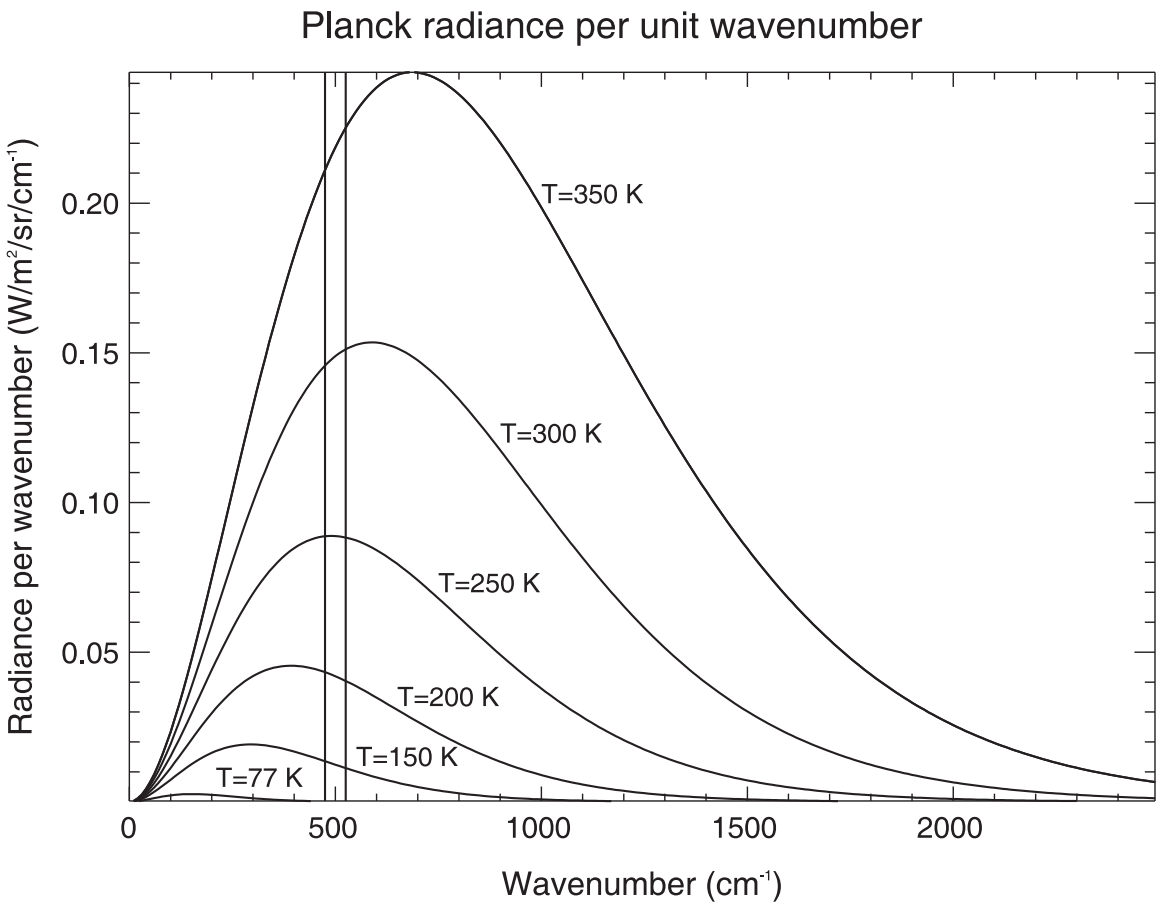

Figure 3.15: Planck (blackbody) emission between 0 and 2500 cm^{-1} for a set of temperatures. The curve for $T = 250$ K, which corresponds to an average value for effective sky temperature, peaks near 500 cm^{-1}, the spectral region IRMA is designed to operate in.

In the case where the atmosphere is optically thick, the opacity term would be very large. A large opacity results in the fractional transmission term, $e^{-\tau}$, going to zero, i.e. $e^{-\infty} \rightarrow 0$. This factor of zero eliminates the $I_\sigma(0)$ in the first term, implying all incident radiation is absorbed by the atmosphere. Due to this large opacity, the only radiation visible to the observer would be emission originating from within the atmospheric emission itself, which would take the form of the Planck curve, $B_\sigma(T)$, in this limiting, optically thick case. The observer would be able to measure to a specific optical depth, and see no atmosphere beyond that depth.

Using Equation 3.39, it is now possible to fully model the radiative transfer within an atmosphere. Before doing so, it is possible to reduce the complex system of a planetary atmosphere for example into more manageable components. Imagine a column of atmosphere with thermal and hydrostatic equilibrium, as described in §2.4. The atmosphere is first divided into horizontal layers containing unique temperatures, pressures, and abundances of molecules. This process is further simplified through application of the Curtis-Godson approximation [37]. The approximation states that for a fixed path length through a medium the path-dependent pressure, $P(z)$, can be represented by the mean pressure, $\bar{p}$ over that path length, defined by:

$$\bar{p} = \frac{\int pc\rho dz}{\int c\rho dz} \qquad \text{[Pa]} \quad , \tag{3.43}$$

where c is the fractional concentration (by mass) of absorber, also known as a mass mixing ratio. This equation effectively weights the pressure according to the density of the absorber as a function of altitude.

Using Equation 3.39, one calculates the radiation leaving a layer in terms of the radiation incident upon the layer and the radiation emitted from the material in the layer itself. Through the process of summing the cumulative radiation over the full span of layers, and all frequencies, the total radiation-matter interaction of the atmosphere can be simulated. This is referred to as the spectral line-by-line, atmospheric layer-by-layer (LBL/LBL) method.

The complexities that arise when doing LBL/LBL come from the additive effect of the output from one layer becoming the input to the next layer. Starting from the top of the atmosphere and working down towards the surface can be summarized as follows. The top-most layer is assumed to have no incoming radiation, i.e. $I_0 = 0$. In reality, there

would be incoming radiation from astronomical objects, however, the radiation at 20 μm is negligible for all objects other than the sun or moon. The ubiquitous cosmic background can also be ignored because it is at microwave frequencies, well outside the measurement range of the MCT photoconductive detector in the IRMA instrument. Even though the top-most layer has no incoming radiation, it will be at some temperature T, for which there will be blackbody radiation. Thus, the bottom output of this top-most layer will only be its blackbody emission spectrum, $I_1 = B_1$. Now, the second layer has the blackbody emission of the top layer as its incident radiation, in addition to its own blackbody emission. This pattern repeats itself all through the set of layers.

To summarize, the model atmosphere is divided into discrete elements referred to as layers. Each layer has a temperature profile, pressure profile, and molecular abundance distribution. Using the Curtis-Godson approximation, mean values can be determined for each of these parameters specific to each layer. The model is created by stepping through the atmosphere, layer by layer, and calculating the frequency dependent absorption, or opacity due to each absorbing species in the system. These frequency dependent opacities are then summed across all layers. The ability to sum opacities rather than multiplying transmittances results in faster computation. Consider the example of two layers of atmosphere, given by I_1 and I_2, with input radiation I_0:

$$I_1 = I_0 \exp(-\tau_1) \tag{3.44}$$

$$I_2 = I_1 \exp(-\tau_2) \tag{3.45}$$

$$I_2 = I_0 \exp(-\tau_1) \exp(-\tau_2) \tag{3.46}$$

$$I_2 = I_0 \exp(-[\tau_1 + \tau_2]) \tag{3.47}$$

$$\vdots \tag{3.48}$$

$$I_N = I_0 \exp\left(-\sum_i^N \tau_i\right) \tag{3.49}$$

Equation 3.49 shows the computational value of using the opacity formulation for a LBL/LBL approach. As the frequency-dependent opacity of each layer is computed, it is literally added to the stack of previously computed opacities, until the total contribution from all atmospheric layers over all frequencies have been tabulated. The resulting spectra is the cumulative absorbtion and emission of all spectral transitions occurring within the region being mapped. This is the process used in a line-by-line, layer-by-layer (LBL/LBL), radiative transfer atmospheric model.

If high spectral resolution is required the contributions of each spectral line must be individually calculated. This is known as the line-by-line method. As noted earlier, each line will have a given profile and its wings will affect all neighbouring lines. The atmospheric model used in this study uses the Voigt profile. The wings of the spectral line profile contribute to all spectral lines falling within the wing profile. This wing size overlap is generally taken to be 25 wavenumbers, beyond which the contribution has been found to be minimal [3]. Considering that there may be thousands of lines within a given region this process quickly becomes computationally intensive. Fortunately, present day computers have the processing power and memory available to efficiently do this, allowing high resolution spectra to be computed on a standard desktop computer in a matter of minutes. When BTRAM was used to compute one high resolution spectrum the process took $\sim$3 minutes. However, when the process was extended to creating an entire atmospheric flux lookup table for IRMA, the same high resolution spectrum was calculated, but then

one parameter was varied, and another spectra was produced for the new parameter set. This iterative process could take many days to complete depending on how extensive the set was of parameters being varied.

It is important to note that line-by-line, layer-by-layer computationally intensive methods are not the only ways to simulate the radiative transfer through an atmosphere. Before computers were sufficiently advanced, there were clever analytical methods used to tackle these problems. One such method is called the correlated-k distribution [38]. It gives information about the values of the k_ν absorption coefficients over the band. It is a statistical approach that can be useful if all that is desired is information about the entire band. It can not give detail about specific absorption features, they are lost in the statistical results. However, recall that instruments in the near-past did not have anywhere near the resolution available in instruments today. Simply predicting or being able to analyse the qualities of an entire band was more than sufficient at the time. The notion of producing a detailed model at that time was more of an academic exercise than something useful to try to compare with experimental data.

3.7 Summary

This chapter has reviewed some of the key elements of radiative transfer theory which are embodied in the atmospheric modeling program BTRAM [12]. Our group developed BTRAM to accurately model the atmosphere for specific locations, initially this had been Mauna Kea, but has been extended to include several sites in Chile, Mexico, and Antarctica. BTRAM is a LBL/LBL atmospheric radiative transfer model based on the HITRAN 2004 molecular database [15]. When studying an atmosphere at relatively high

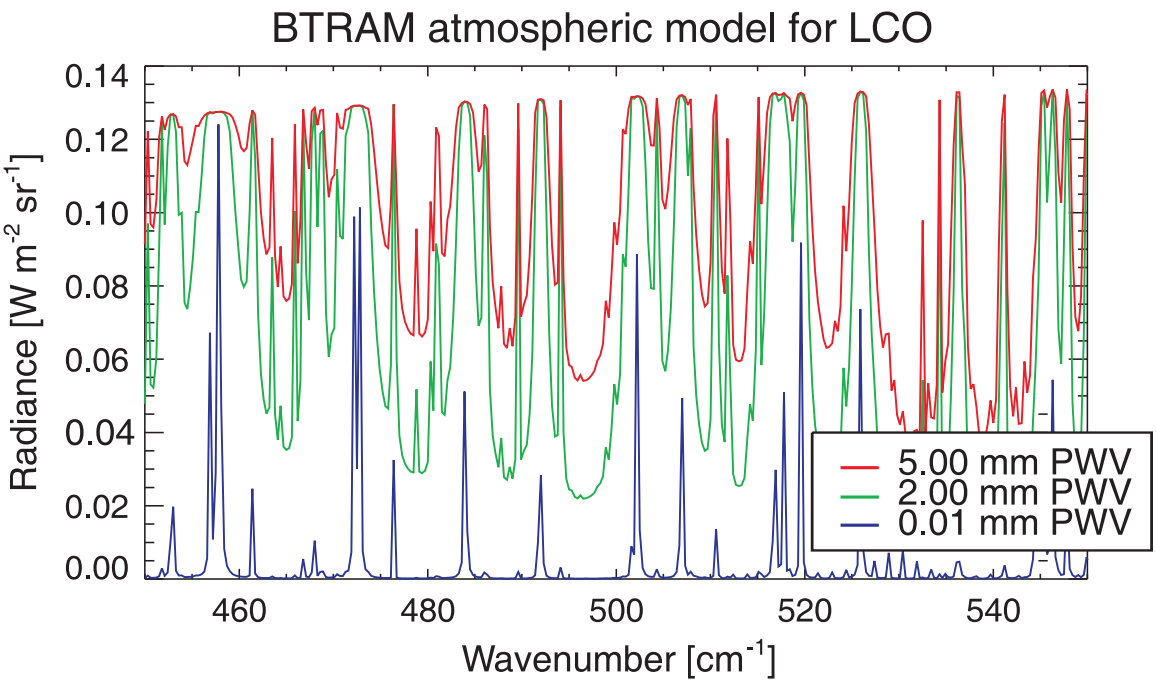

Figure 3.16: Simulated atmospheric flux spectrum for PWV = 0.01, 2.00 and 5.00 mm. The water emission lines begin to saturate to the Planck envelope at relatively low PWV. IRMA is most sensitive below this saturation limit.

resolution, the differences between using a generic representative model, and a site-specific model based on local radiosonde data, are directly measurable. Thus, site-specific, simulated atmospheric flux, as shown in Figure 3.16, are necessary if one is trying to identify, and minimise, any systematic effects introduced to the measurement through the model.

The process of creating flux-to-PWV models requires the creation of data cubes. These data cubes are created through a batch processing mode that has been implemented in BTRAM. Figure 3.16 shows the simulated atmospheric flux for PWV = 0.01, 2.00 and 5.00 mm. The water emission lines begin to saturate to the Planck envelope at relatively low PWV. IRMA is most sensitive at low PWV because the variation in flux with respect to PWV decreases as the water vapour lines saturate.

Site-specific atmospheric modeling has been incorporated into BTRAM through the use of configurable atmospheric profiles. These profiles can be created through the statistical analysis of radiosondes, as will be described in §4.3. Parametric studies have been performed to determine the particular influence each atmospheric parameter has on the resulting PWV output data. These studies will be discussed in further detail in §4.6. In the following chapter I will present results from modeling atmospheres and PWV sensitivity studies based on uncertainties in the model input parameters.

Chapter 4

Atmospheric modeling

All remote sounding instruments require an accurate instrument model, atmospheric model, and retrieval algorithm to properly interpret measurements. The accuracy of the PWV measurements made by IRMA depend both on the accuracy of the experiment itself, and the accuracy of the atmospheric model. Any error in the model will propagate through to the final PWV measurement value. For this reason it is necessary to understand the sensitivity of each parameter to error, i.e. what does $\pm 10\%$ uncertainty in a given parameter mean in terms of the resulting uncertainty in PWV? Since, in general, there will be no real-time radiosonde data describing the atmosphere at the instant the PWV measurement is made, it is necessary to rely on a statistical approach using data from radiosondes. Radiosondes, informally referred to as weather balloons, are discussed in §4.3. To create site-specific atmospheric profiles, I have accessed the archival radiosonde data pertaining to the sites being studied, and have calculated statistically representative input parameters and profiles for use in our atmospheric model.

4.1 Overview

Atmospheres are complex assemblies of molecules at varying pressures and temperatures. It is possible to simplify the system through the use of generalizing assumptions. The atmosphere is assumed to be in local hydrostatic equilibrium (LPE) and local thermal equilibrium (LTE) which implies no net vertical motion, essentially a static atmosphere with the molecules well-mixed. Atmospheric parameters can be further reduced through application of the Curtis-Godson approximation which states that average parameter values within each layer can approximate that layer in its entirety [37]. These conditions do not account for possible horizontal motion, however, if the atmosphere is stratified and in LTE and LPE, any winds or strictly horizontal motion would not be measurable since all material in the layer would be equivalent.

In this chapter, the process of creating a site-specific atmospheric model will be described. A sensitivity analysis of the model parameters will also be explored in §4.6.

4.2 Atmospheric profiles

An atmospheric profile is a collection of data that accurately describes an atmosphere. The profiles used in BTRAM [12] are based on the data and formatting used by FASCODE [13], see §1.4 for a full listing of profiles included with BTRAM. They take the form of a table of values for altitude, pressure, temperature, and densities in the form of mass mixing ratios of gases present in the atmosphere. Figures 3.11 and 3.12 show the temperature and pressure versus altitude profiles from the U.S. Standard Atmosphere 1976, respectively. Figure 3.13 shows the mass mixing ratios for N_2O, O_2, CO_2, CH_4, H_2O, CO,

and O_3 used in the USSA1976 [32]. As described in §3.3, while N_2 is the most abundant gas in the atmosphere, it is a homopolar molecule, and therefore does not possess a permanent electric dipole moment, nor any significant rotational transitions. Although, the same can be said of O_2, its profile is included because it is a fundamental component of atmospheric chemistry. Of the methods that exist to measure the composition and properties of the atmosphere, the only practical, global source of data to create atmospheric profiles is a series of radiosondes, discussed in the following section.

4.3 Radiosonde analysis

A radiosonde is a balloon borne suite of meteorological instruments that make *in situ* atmospheric measurements of pressure, temperature, wind speed, and dew point or relative humidity at altitudes up to 20 or 30 km [39]. From these data, pressure versus altitude, or temperature versus altitude plots can be constructed, allowing adiabatic lapse rate and scale height of water to be determined, described further in §4.4 and §4.5.

Radiosondes are the best candidates for providing site-specific atmospheric models. While a radiosonde may not be launched directly from the site being studied, radiosondes are launched from airports around the world, usually twice a day, at 0h and 12h UT. These radiosonde launches create a network of global coverage, whose vast data archives [40] allow statistical analyses to be performed. These publicly available radiosonde data are a great resource to anyone studying atmospheres. The more that can be known about the exact geographical location being studied the better the resulting model. Radiosonde data are actual measurements of atmospheric conditions. Knowing these parameters to high precision and as close as possible to the location in question is important. For three of the Chilean

sites being studied by the TMT site selection committee, the closest radiosonde launch location is Antofagasta, Chile, at 23.43° S 70.43° W. The mean distance from Antofagasta to any of the three sites is ∼185 km. This brings up the question of applicability of the radiosonde data. Is 185 km close enough to be physically meaningful? It is hoped that since the radiosonde data is within a few hundred kilometers it should represent the gross characteristics of the region. For instance, the radiosondes launched for use at Mauna Kea are launched twice daily from Hilo International Airport, Hawaii. Hilo is ∼50 km away from the observatory locations on Mauna Kea, however, the path the balloons will follow as they rise depends upon the prevailing wind conditions. While this uncertainty in balloon location seems counter to the intent of creating site-specific models from the radiosondes, it is important to note that a model representing a specific region is still much better than a model representing a latitude. This can be further improved upon by representing a series of single seasons for a specific region, i.e. winter at a given location.

As part of this thesis, I accessed the NOAA database of global radiosondes [40] and reprocessed their raw data from first principles to create site-specific atmospheric models, and determine the resulting PWV sensitivity of the model in terms of input parameter uncertainty. The NOAA website radiosonde database is accessible to the public. Technical documents are also available online that detail the radiosonde data formats and the database itself [41]. The radiosonde data available from the NOAA site contain pressure [mbar], height [m], temperature [°C], dew point [°C], wind direction [degrees], and wind speed [$\mathrm{m\,s^{-1}}$]. Wind information is not required in this analysis. An example of typical raw radiosonde data is shown in Table 4.1.

Table 4.1: Sample radiosonde data from the NOAA radiosonde archive [40].

1	2	3	4	5	6	7
LINTYP						
			header lines			
254	HOUR	DAY	MONTH	YEAR	(blank)	(blank)
1	WBAN#	WMO#	LAT D	LON D	ELEV	RTIME
2	HYDRO	MXWD	TROPL	LINES	TINDEX	SOURCE
3	(blank)	STAID	(blank)	(blank)	SONDE	WSUNITS
			data lines			
9	PRESSURE	HEIGHT	TEMP	DEWPT	WIND DIR	WIND SPD
⋮						
254	12	7	AUG	2007		
1	99999	85442	23.43S	70.43W	120	32767
2	100	160	86	33	32767	3
3		SCFA			32767	ms
9	1004	120	106	73	360	15
4	1000	149	104	60	55	10
4	925	792	50	43	160	31
5	924	801	48	39	32767	32767
5	918	855	118	-182	32767	32767
5	914	892	158	-242	32767	32767
5	892	1098	156	-294	32767	32767
5	874	1271	184	32767	32767	32767
4	850	1509	178	32767	130	51
4	700	3132	76	32767	60	26
5	692	3226	74	32767	32767	32767
4	500	5800	-135	-595	275	82
5	458	6458	-189	-629	32767	32767
4	400	7450	-249	-669	275	247
5	374	7935	-269	-679	32767	32767
4	300	9490	-389	-639	275	442

Note: data points with values of `32767` indicate no data, and both atmospheric temperature and dew point are recorded in tenths of degrees.

Figures 4.1 and 4.2 show data from 3003 daily radiosondes launched from Antofagasta, Chile, spanning August 1998 through to May 2007. Both figures plot all the raw radiosonde data, as well as the mean, and mean $\pm$ the standard deviation, σ. Figure 4.1 is the mean pressure profile, with $\sigma_P = 2.75$ mb (or 0.3% of atmospheric pressure). Figure 4.2 is the mean temperature profile, with $\sigma_T = 3.59$ K (or 1.3% of typical base atmospheric temperatures). The pressure profile is well-behaved; the data, mean, and standard deviation are almost indistinguishable on the scale shown. The temperature profile has a significantly larger spread across the data set, yet for the most part the data is still well behaved. Variations between the daily radiosondes is minimal and leads us to accept the mean of these radiosondes as representative of the launch region. The multi-year data set can be subdivided into seasonal sets or even monthly sets. No significant difference has been found between the multi-annual mean and the mean values derived from any subset of the data.

Though the vast amount of semi-local, statistically processed, radiosonde data may, to first-order, seem to solve the puzzle of characterizing the environment around a site, there remains the challenge of knowing how the error in each parameter is propagated. How does the uncertainty in each parameter contribute to the eventual determination of flux and PWV? These parameters include ambient temperature, ambient pressure, adiabatic lapse rate, and the scale height of water vapour. Temperature and pressure can be measured to fairly high precision with locally installed meteorological towers, and thus are of little concern here. Adiabatic lapse rate can be determined from the slope of a temperature versus altitude plot using raw radiosonde data, or statistically derived mean of the data, as shown in Figures 4.3 and 4.4. The linear relationship between temperature decrease and

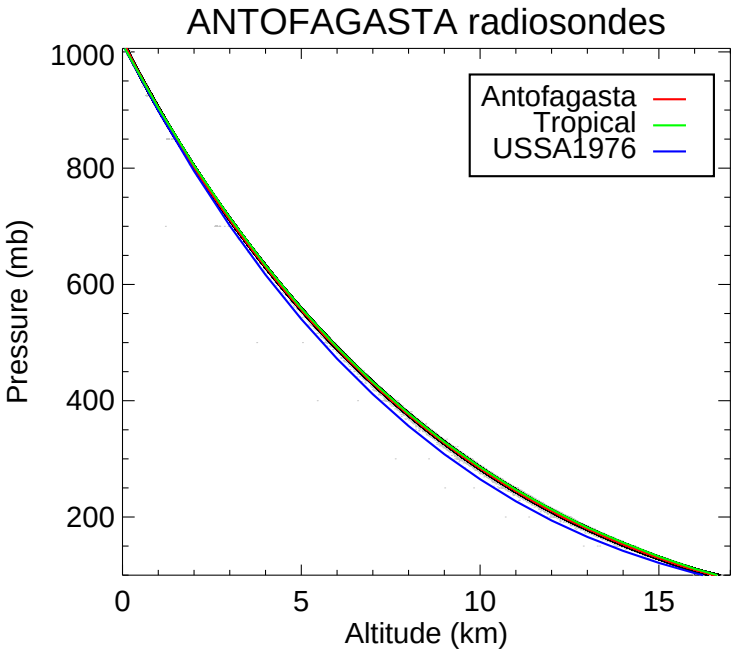

Figure 4.1: Pressure versus altitude data from a set of 3003 radiosondes spanning approximately a 10 year period launched from Antofagasta, Chile [40]. Raw radiosonde data points are plotted (grey), the mean of these data (red) and the ± standard deviation (black). The pressure profiles from both the FASCODE Tropical (green) and U.S. Standard Atmosphere 1976 (blue) are also shown for comparison.

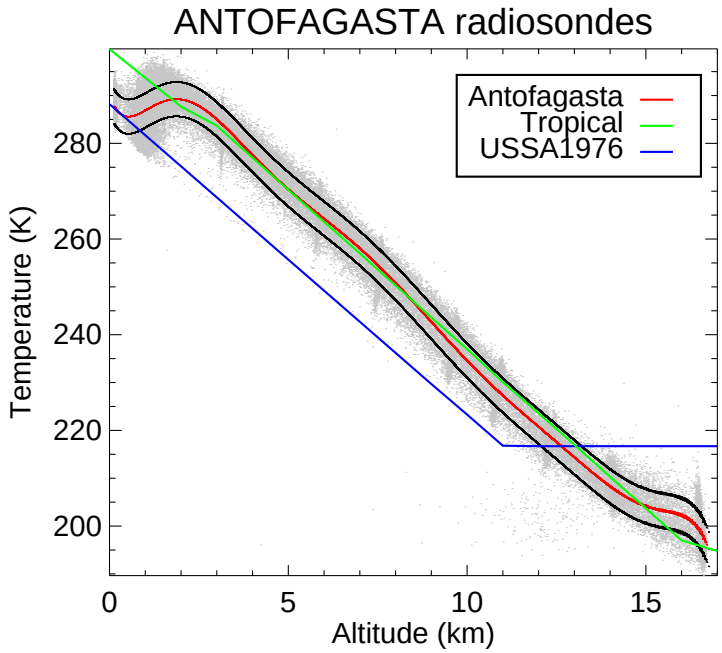

Figure 4.2: Temperature versus altitude data from a set of 3003 radiosondes spanning approximately a 10 year period launched from Antofagasta, Chile [40]. Raw radiosonde data points are plotted (grey), the mean of these data (red) and the ± standard deviation (black). The temperature profiles from both the FASCODE Tropical (green) and U.S. Standard Atmosphere 1976 (blue) are also shown for comparison.

elevation increase is valid from the surface of the Earth through to the tropopause (the temperature inversion boundary where the troposphere* is decoupled from the stratosphere). The altitude of the tropopause varies according to latitude, having heights ranging from ∼8 km at the poles to ∼18 km over the western equatorial Pacific due to the rotation on the Earth and the different amounts of solar radiation incident on the Earth [37]. For comparison, as it effects my proposed Ph.D. studies, Figure 4.5 shows the measured Antarctic tropopause (at Dome C) occurring at ∼ 9 km. In this figure, which is plotted to the same scale to allow for a direct comparison, no linear lapse rate is observed, and furthermore, there is a strong inversion layer just above the surface. Thus, any model employing a lapse rate within the troposphere is inapplicable to Antarctica. A more complex model is required to represent these conditions.

The accuracy of PWV measurements resulting from the IRMA instrument/BTRAM atmospheric model combination are limited by the accuracy of the site-specific atmospheric model. An understanding of how uncertainty in the input parameters propagate through the atmospheric model is essential. One way of achieving this is to systematically vary input parameters and determine how those variances are reflected in the final PWV output of the model. There are four model input parameters to be studied in this way. Base pressure, P and base temperature, T, are both are measured directly at the site, whereas adiabatic lapse rate, Γ, and the scale height of water, H, are statistically derived. The determination of Γ and H from radiosonde data is described in the following two sections.

*The *troposphere*, or turning-sphere, is coupled to the surface, and thus rotates with the Earth.

4.4 Determination of adiabatic lapse rate

The term adiabatic refers to a reversible thermodynamic process that occurs without gain or loss of heat and without a change in entropy. Adiabatic lapse rate, Γ, is the rate of decrease of temperature with increase in altitude [43], given by:

$$-\frac{dT}{dz} = -\left(\frac{T_2 - T_1}{z_2 - z_1}\right) = \frac{g}{c_p} = \Gamma \qquad [\text{K m}^{-1}] \ , \tag{4.1}$$

where c_p is the specific heat capacity of air at constant pressure [J kg^{-1} K^{-1}] and g is the acceleration due to gravity, where $g = 9.80665$ ms^{-2} [44]. For dry air at 273 K, $c_p = 1005.7 \pm 2.5$ [J kg^{-1} K^{-1}] [45], resulting in a calculated lapse rate of $\Gamma = -9.751 \pm 0.024$ K km^{-1}. Measured lapse rates are much less than this with typical values ranging from ~ -5 to -7 K km^{-1}. This difference is sometimes referred to as the wet adiabat, as opposed to the dry adiabat component; the atmosphere should get colder faster, but it does not. All measured lapse rates are lower than the theoretical $\Gamma \approx -10$ K km^{-1} due solely to having a condensable substance mixed into the atmosphere. Water exists in different phases (gas, liquid, and solid) over the temperature range occurring in our atmosphere. Unlike, N_2 and O_2 which do not condense and precipitate in our atmosphere, water does have this property. As elevation increases and the atmosphere gets colder, a critical point is reached at which water vapour will condense and form dimers and eventually droplets of water (or ice crystals). As water condenses and goes through a phase transition, the energy associated with the transition is released back into the atmosphere as latent energy. This serves to warm the atmosphere, effectively allowing it to keep its heat at higher altitudes than possible if it were dry, thus the reason why $\Gamma_{\text{measured}} > \Gamma_{\text{theoretical}}$.

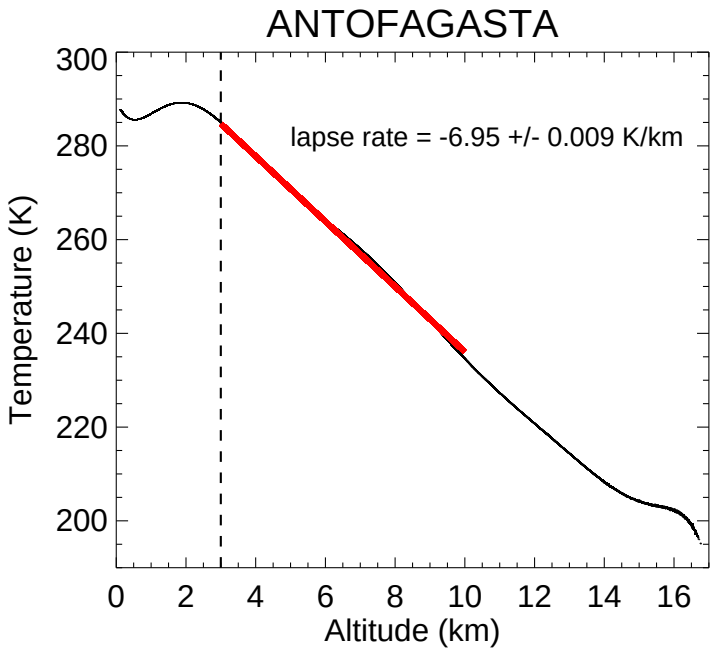

Figure 4.3: Mean temperature versus altitude data set derived from 3003 radiosondes launched from Antofagasta, Chile [40]. The temperature data from 3 – 10 km was fitted to a line, resulting in a value for the lapse rate of $\Gamma = -6.95 \pm 0.009$ K/km. The dotted line denotes the base elevation.

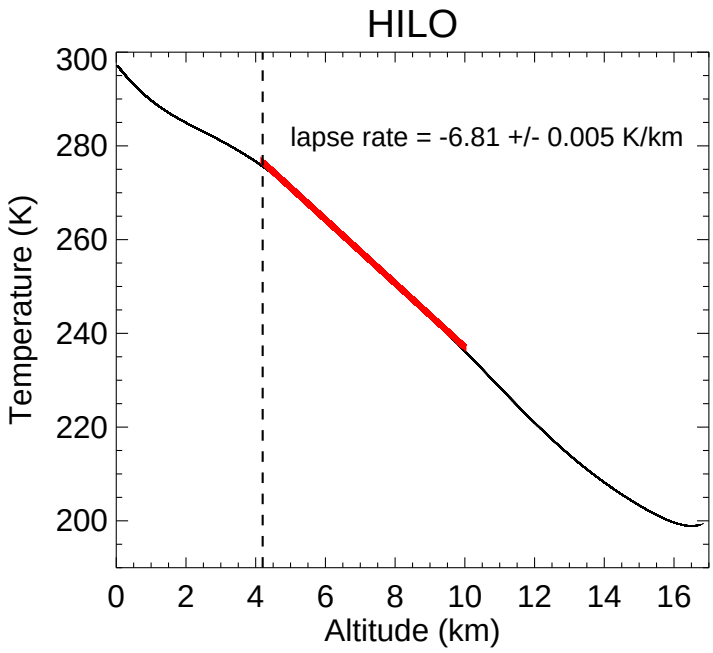

Figure 4.4: Mean temperature versus altitude data set derived from 8623 radiosondes launched from Hilo, Hawaii, USA. [40]. The temperature data from 4.2 – 10 km was fitted to a line, resulting in a value for the lapse rate of $\Gamma = -6.81 \pm 0.005$ K/km. The dotted line denotes the base elevation.

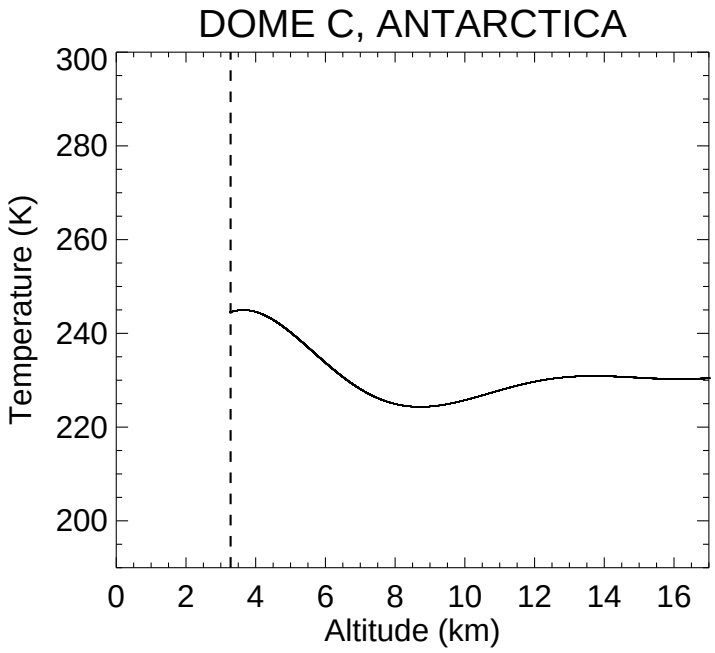

Figure 4.5: Mean temperature versus altitude data set derived from 115 radiosondes launched from Dome C, Antarctica over summer during January 2003, December 2003, and January 2004. Lapse rate can not be easily fitted here due to the strong inversion layer location near the surface, thus a more complicated system for modeling the atmosphere above Antarctica is required. The dotted line denotes the base elevation.

Temperature plays a significant role in atmospheric emission. A simple way to understand this is to think of blackbody emission and its dependence on temperature. If the quantity of atmospheric water vapour is held constant but it is warmed, and therefore has more energy, the water vapour will emit more radiation. It is through this reasoning that adiabatic lapse rate gains its importance because it determines the temperature of the atmosphere within the model. Base temperature (ambient T) is input into the model, and Γ determines the atmospheric temperature from the surface up to the tropopause, above which default temperature values from an atmospheric profile are used. Uncertainty in the lapse rate will have a significant effect due to the potential differences in temperature that it introduces into the model.

Adiabatic lapse rate can be measured directly from statistically averaged radiosonde data, as shown in figure 4.3 for the set of Antofagasta radiosondes resulting in an adiabatic lapse rate measurement of $\Gamma = -6.95 \pm 0.009$ K/km. The set of Hilo radiosondes result in a lapse rate of $\Gamma = -6.81 \pm 0.005$ K/km. While theses values for lapse rate may not represent the exact lapse rate in effect at the time of the PWV measurement, it is reasonable to assume the lapse rates obtained from a spatially and seasonally representative set of radiosondes is statistically close enough for our purposes. The Hilo data set includes January 1994 through to May 2007, whereas Antofagasta data spans from August 1998 to May 2007.

4.5 Determination of scale height of water vapour

Scale height, H, as discussed in §2.4, is the interval of height at which the pressure/density of the atmosphere decreases by a factor of $1/e$ [37]. H determines the distribution of water vapour within the atmosphere.

An important distinction needs to be made between the scale height of the atmosphere and the scale height of water vapour. They both result in a similar decrease in pressure/density but they have radically different values. The scale height of the atmosphere is on the order of 8 km, as calculated in §2.4, while the scale height of water vapour found in the literature ranges from ∼1.0 to 2.5 km. The reason for the difference between the two scale heights (atmospheric and water vapour) is the same reason a difference exists between Γ_{measured} and $\Gamma_{\text{theoretical}}$. Again, it is the presence of water vapour and its propensity to condense that creates the difference. The atmosphere is primarily composed of N_2 ($\sim 78\%$ by volume) and O_2 ($\sim 21\%$ by volume), both of which are well-mixed and present in their

gas phase throughout the entire atmosphere. The water in our atmosphere exhibits more complicated behaviour. The property most affecting the scale height of water vapour is its tendency to condense into a liquid (or solid) phase and precipitate. As altitude increases, and temperature decreases, there comes a boundary beyond which the presence of gaseous water falls off rapidly, as opposed to N_2 and O_2 which do not condense under the conditions within our atmosphere.

As mentioned above, scale height is a decrease in pressure or density with respect to increase in altitude. Therefore, to determine scale height, the partial pressure of water vapour, P_{water}, and the density of water vapour, ρ_{water}, must first be expressed as a function of altitude. The raw radiosonde data provides values for pressure, P, temperature, T, dewpoint temperature, D, and altitude, Z. From these values, it is possible to determine the partial pressure of water vapour, and subsequently the density of water vapour. Once density has been calculated, scale height can be determined satisfying the following equality:

$$\rho_{\text{water}}(h + H) = \frac{\rho_{\text{water}}(h)}{e} \ . \tag{4.2}$$

This equality, based on the equation for scale height, Equation 2.2, states that the density at height $h + H$ is equal to the density at height h divided by e. Thus, H is the height interval required to decrease density by a factor of $1/e$, the definition of scale height.

Once the density, $\rho_{\text{water}}(h)$ is known, multiplication by an interval of height results in a water vapour column density with units kg m^{-2}. These units are functionally equivalent to the linear units of PWV expressed in mm*.

*1 kg of water distributed equally over a unit area of 1 m^2 will have a depth of 1 mm.

4.5.1 Calculating the partial pressure of water vapour

To calculate the partial pressure of water vapour, P_{water}, it is necessary to introduce the concept of saturation, or equilibrium, vapour pressure. As has been discussed, the atmosphere contains varying amounts of water vapour. The heat carrying capacity of the air is proportional to this amount. As the amount of water vapour in the air increases, there reaches a point of saturation, beyond which the addition of more water vapour is not possible, and precipitation occurs. This point of saturation is dependent on the dew point for conditions in question. The dew point temperature, D, for a parcel of air at a constant pressure is the temperature at which water vapour will condense and form drops of liquid water, or ice crystals if the dew point is below the freezing point of water.

An expression for equilibrium vapour pressure, $e_s(T)$, with 0.3% accuracy over the temperature range $-35\ ^\circ\text{C} \leq T \leq 35\ ^\circ\text{C}$ is given as [46]:

$$e_s(T) = 6.112 \times \exp\left(\frac{17.67 \times T}{T + 243.5}\right) \qquad \text{[mb]} \quad , \tag{4.3}$$

where T is the temperature of the gas [°C]. For example, if $T = 26.6\ ^\circ\text{C}$, and $D = 20.6\ ^\circ\text{C}$ for a volume of atmosphere, the equilibrium vapour pressures are calculated as:

$$e_s(20.6) = 6.112 \times \exp\left(\frac{17.67 \times 20.6}{20.6 + 243.5}\right) = 24.25 \qquad \text{[mb]} \ , \tag{4.4}$$

$$e_s(26.6) = 6.112 \times \exp\left(\frac{17.67 \times 26.6}{26.6 + 243.5}\right) = 34.83 \qquad \text{[mb]} \ . \tag{4.5}$$

The difference between these partial pressures is due to the atmosphere not being saturated with water vapour. If the atmosphere were saturated, the temperatures would be equal, $T = D$. Air at $T = 26.6\ ^\circ\text{C}$, $P_{\text{water}} = 34.83$ mb if it was saturated with water vapour. However, it is not saturated, as shown by $T > D$. At its current level of saturation, $P_{\text{water}} = 24.25$ mb. Thus, the relation for partial pressure of water vapour, P_{water}, is given

by:

$$P_{\text{water}} = e_s(D) \qquad [\text{mb}] \ , \tag{4.6}$$

where D is the dew point temperature. A useful indicator known as the relative humidity index, is based on the ratio of the saturation vapour pressures computed at T and D. Relative humidity, RH [%], is expressed as:

$$RH = \frac{e_s(D)}{e_s(T)} \times 100\% \qquad [\%] \ . \tag{4.7}$$

where T is atmospheric temperature, and D is the dew point temperature. For the example given above the relative humidity is 69.9%:

$$RH = \frac{24.25}{34.83} \times 100\% = 69.6\% \ . \tag{4.8}$$

With RH = 69.6%, the water content of the atmosphere is such that the partial pressure of water vapour as determined by $e_s(T)$ at the dew point is 69.6% of the partial pressure as determined at the measured air temperature. At RH = 100%, the atmosphere is saturated with water vapour and precipitation will occur.

Water molecules are constantly changing phase (solid, liquid, or gas). If more water molecules are leaving a liquid surface than arriving, there is a net evaporation. If more are arriving there is a net condensation. The rate at which molecules leave (or arrive at) a surface depends on vapour pressure. As air is cooled (and thus water vapour also cools) the evaporation rate decreases more rapidly than does the condensation rate resulting in a critical temperature (dew point) where evaporation is less than condensation and a water droplet (or ice crystal) can form.

4.5.2 Calculating the density of water vapour

The vertical distribution of any atmospheric component can be expressed as a mass mixing ratio profile. The mass mixing ratio for water vapour is defined as the ratio of water vapour mass to dry air mass within a given volume [37]. Since the mass-to-mass ratio is being computed within an equal volume, it is equivalent to a density-to-density ratio $\left(\frac{m_1}{V} : \frac{m_2}{V} \equiv \rho_1 : \rho_2\right)$. Thus, the mass mixing ratio can be computed with densities for each atmospheric layer.

$$\text{Mixing ratio} = \frac{\rho_{\text{water}}(z)}{\rho_{\text{air}}(z)} \quad , \tag{4.9}$$

where z goes from the base elevation to the top of the atmosphere. Since water vapour is primarily constrained to the troposphere, and the radiosonde database had little data above 16 km, the generic latitude-based profiles from FASCODE were used from 16 to 54 km, the top of our model.

Having calculated the partial pressure of water vapour in the previous subsection, it is possible to use that quantity to determine the density of water vapour through an application of the ideal gas law. According to the ideal gas law:

$$P\,V = N\,k_B\,T \qquad [\text{J}] \quad , \tag{4.10}$$

where P is pressure [Pa*], V is volume [m^3], N is the number of molecules, k_B is the Boltzmann constant [J K^{-1}], and T is the absolute temperature [K]. If density, ρ, is defined as a number density equal to N/V, then Equation 4.10 becomes:

$$P = \rho\,k_B\,T \qquad [\text{Pa}] \equiv [\text{N m}^{-2}] \quad . \tag{4.11}$$

*Note: 1 millibar [mb] = 100 Pascals [Pa]

To calculate the density of air, ρ_{air}, for a given parcel of atmosphere, Equation 4.11 can be re-expressed as:

$$\rho_{\text{air}} = \frac{P_{\text{atm}} - P_{\text{water}}}{k_B\ T} \times \frac{M_{\text{air}}}{N_A} \qquad [\text{kg m}^{-3}] \tag{4.12}$$

where M_{air}* is the molecular mass of dry air [0.02896443 kg mol^{-1}], N_A is Avogadro's number [6.022×10^{23} mol^{-1}], P_{atm} is atmospheric pressure [Pa], P_{water} is the partial pressure of water [Pa], k_B is the Boltzmann constant [J K^{-1}], and T is atmospheric temperature within the parcel [K]. When performing any of these calculations it is important to be aware of the units being used. Some formulations use pressure in millibars, whereas others use the SI unit of Pascals, others use temperatures expressed in Celsius rather than Kelvin. When calculating ρ_{air} using Equation 4.12, the pressure parameter is $P_{\text{atm}} - P_{\text{water}}$. This is because the air density being calculated is not that of the air in its entirety, but that of dry air (without any water content). Thus the need to subtract the partial pressure due to water, P_{water}. Following the example from the previous page with conditions of $P = 1014$ mb, $T = 26.6$ °C, $D = 20.6$ °C, and thus $P_{\text{water}} = 24.25$ mb, the density of air is calculated as:

$$\rho_{\text{air}} = \frac{P_{\text{atm}} - P_{\text{water}}}{1.3806503 \times 10^{-23} \times (273.15 + T)} \times 100 \times \frac{0.02896443}{6.022 \times 10^{23}} \tag{4.13}$$

$$\rho_{\text{air}} = \frac{1014 - 24.25}{1.3806503 \times 10^{-23} \times (273.15 + 26.6)} \times 100 \times \frac{0.02896443}{6.022 \times 10^{23}} \tag{4.14}$$

$$\rho_{\text{air}} = \frac{989.75}{1.3806503 \times 10^{-23} \times (299.75)} \times 100 \times \frac{0.02896443}{6.022 \times 10^{23}} \tag{4.15}$$

$$\rho_{\text{air}} = 1.150 \qquad [\text{kg m}^{-3}] \tag{4.16}$$

The factor of 100 in the air density equations above is required to convert the $P_{\text{atm}} - P_{\text{water}}$ pressure term from millibars to Pascals. Water vapour density can also be determined using

*M_{air} can be estimated through the composition of the atmosphere. 78% N_2 ($M_{N_2} = 28$ g/mol), 21% O_2 ($M_{O_2} = 32$ g/mol), and 1% Ar ($M_{Ar} = 40$ g/mol), resulting in a weighted average of $M_{\text{air}} = 28.96$ g/mol

a re-expression of Equation 4.11:

$$\rho_{\text{water}} = \frac{P_{\text{water}}}{k_B\ T} \times \frac{M_{\text{water}}}{N_A} \qquad [\text{kg m}^{-3}] \ , \tag{4.17}$$

where M_{water} is the molecular weight of water [0.018015 kg mol^{-1}].

$$\rho_{\text{water}} = \frac{24.25}{1.3806503 \times 10^{-23} \times (299.75)} \times 100 \times \frac{0.018015}{6.022 \times 10^{23}} \tag{4.18}$$

$$\rho_{\text{water}} = 1.753 \times 10^{-2} \qquad [\text{kg m}^{-3}] \tag{4.19}$$

4.5.3 Calculating precipitable water vapour

Now that the density of water vapour, ρ_{water}, in a given parcel has been computed, to determine the column density of the water, also expressible as PWV, simply multiply the density by the height of the layer, for example $h = 1000$ m:

$$\text{PWV} = \rho_{\text{water}} \times h \ , \tag{4.20}$$

$$\text{PWV} = 1.753 \times 10^{-2} \times 1000 \ , \tag{4.21}$$

$$\text{PWV} = 17.53 \qquad [\text{kg m}^{-2}] \ . \tag{4.22}$$

As mentioned in §4.5, 1 kg m^{-2} of water vapour will have a depth of 1 mm if condensed. Thus the computed water vapour column density of 17.53 kg m^{-2} $\equiv$ 17.53 mm PWV. PWV is being used here to represent the column abundance in one layer. PWV can also refer to the total column abundance of water vapour, i.e. integrated over all layers. 17.53 mm of PWV is extremely high if considering the site to be useful for astronomical observing, however, one should be reminded that the conditions for the calculation performed above are for a location at sea level. On average there is $\sim$ 25 mm of PWV distributed above the entire surface of the Earth. Since this amount of water decreases exponentially with

altitude, shown by Equation 2.2, therein lies the fundamental reason to use high altitude sites for observatories.

4.5.4 Calculating scale height

When H is determined using the column density relationship in Equation 4.2, it is important to recall that radiosondes are often launched from elevations far below the observatory locations. For example, Hilo airport launches radiosondes at sea level, but the base elevation of Mauna Kea is ∼4200 m. While there is data allowing the calculation of H for elevations below 4200 m, the purpose of the study is to determine the scale height above the site. Therefore the base density used in the calculation is the density at the observing site. Having devised a method of determining H from radiosondes, it is necessary to statistically characterise the results in a meaningful sense. From the 3003 radiosondes for Antofagasta, the $1/e$ points were calculated (starting from the base values at 3000 m), and the resulting values of H were plotted in Figure 4.6. The frequency of derived scale heights are plotted in histogram form. The red line is a binned representation of the raw histogram data. An exponential function has been fitted to the data, shown as the blue line. The vertical green lines indicate the selected range of scale height values,

$1.1 < H < 1.7$ km.

The lower values of scale height, $H < 1$ km, represent wet atmospheric conditions. For example, if $H = 0.5$ km, then in a 1 km interval of altitude, 2 scale heights will have elapsed, implying >86 % of the atmospheric water column is located within 1 km above the base. This water vapour would be pressure broadened and subject to the relatively higher temperatures found near the surface of the Earth. Observing conditions would be poor,

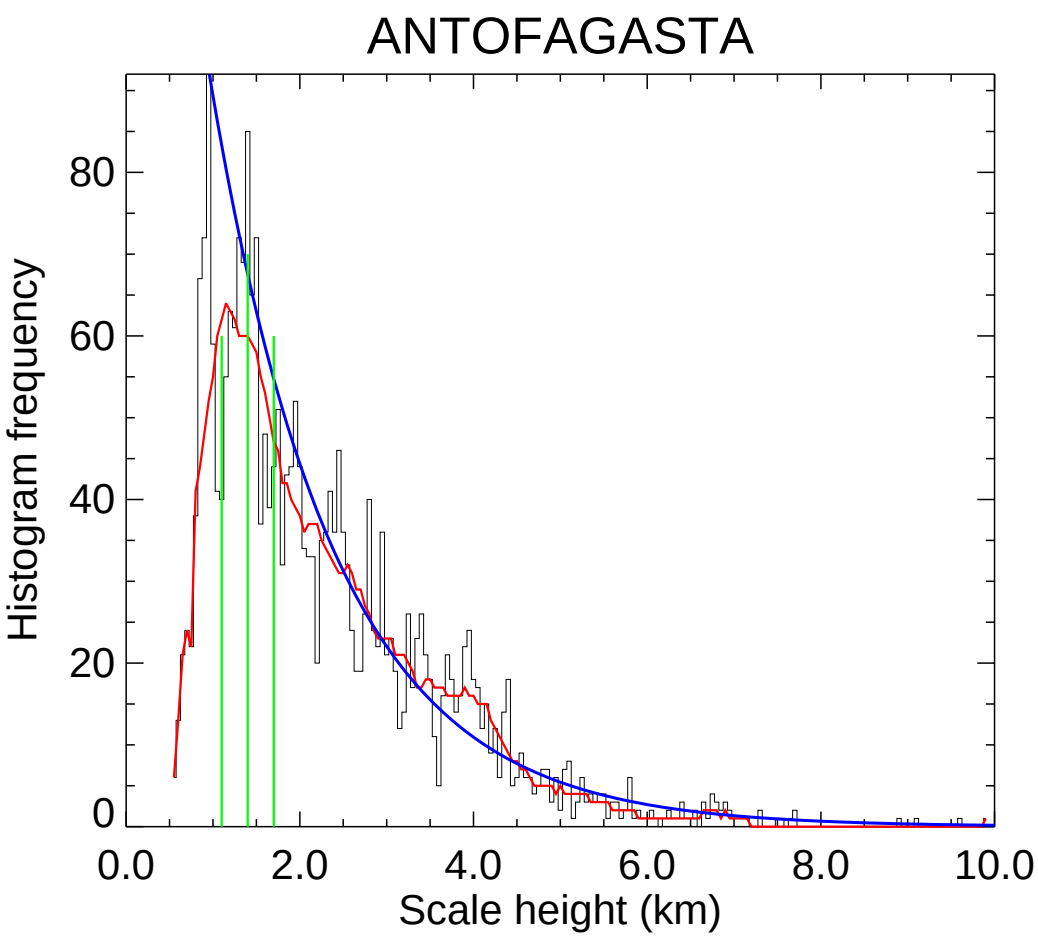

Figure 4.6: Scale heights calculated from 3003 radiosondes from Antofagasta, Chile. To calculate H, the $1/e$ point was determined relative to the base value at 3000 m. The histogram of the scale heights is shown in black with a bin width of 50 m. The red line is the histogram smoothed by a factor of 10. The blue line represents an exponential fit to the data. The vertical green lines, $H = 1.1$, 1.4 and 1.7 km, indicate the range of scale heights that I have used in the sensitivity study, which represents typical observing conditions.

and likely not be performed under these conditions. For this reason, scale heights less than 0.5 km have been removed from the data set calculated above.

The higher values of scale height, $H > 2$ km, represent dry atmospheric conditions. In the same hypothetical 1 km interval used in the example above, if $H = 2.0$ km, only half of a scale height will have elapsed, implying $\sim$40 % of the water vapour column is located in the bottom 1 km interval. When compared to the >86 % water vapour present in the

example of wet atmospheric conditions, a scale height of 2 km or greater has the potential of offering good observing conditions.

Having now determined values for Γ and H from the radiosonde data, a sensitivity analysis was performed on these parameters as applied within the atmospheric model.

4.6 Parameter sensitivity analysis

The four input parameters evaluated in terms of their effect upon the resulting sensitivity of PWV measurements were surface P, surface T, Γ, and H. Each of these parameters was independently varied whilst holding the other parameters at typical values. The resulting variance was determined for atmospheric water vapour content of 0.5, 1.0, and 2.0 mm PWV, corresponding to excellent, good, and poor observing conditions at submillimetre wavelengths. These studies were performed using the full set of Antofagasta radiosonde data.

Figure 4.7 shows the PWV sensitivity to input parameter variations. Figure 4.8 displays the same data as a percentage difference from unvaried as a function of increasing PWV. For each of the plots, one parameter was varied while the other three were held at typical values. PWV resulting from the model run with the varied parameter is plotted versus the PWV resulting from the unvaried parameter. Through this method, the PWV sensitivity to changes in each parameter can be explored. Figure 4.7 uses preliminary parameter uncertainties chosen to demonstrate the relative significance of each parameter. Later in this section, more representative parameter uncertainties will be used to show the actual sensitivity to PWV for the given parameters.

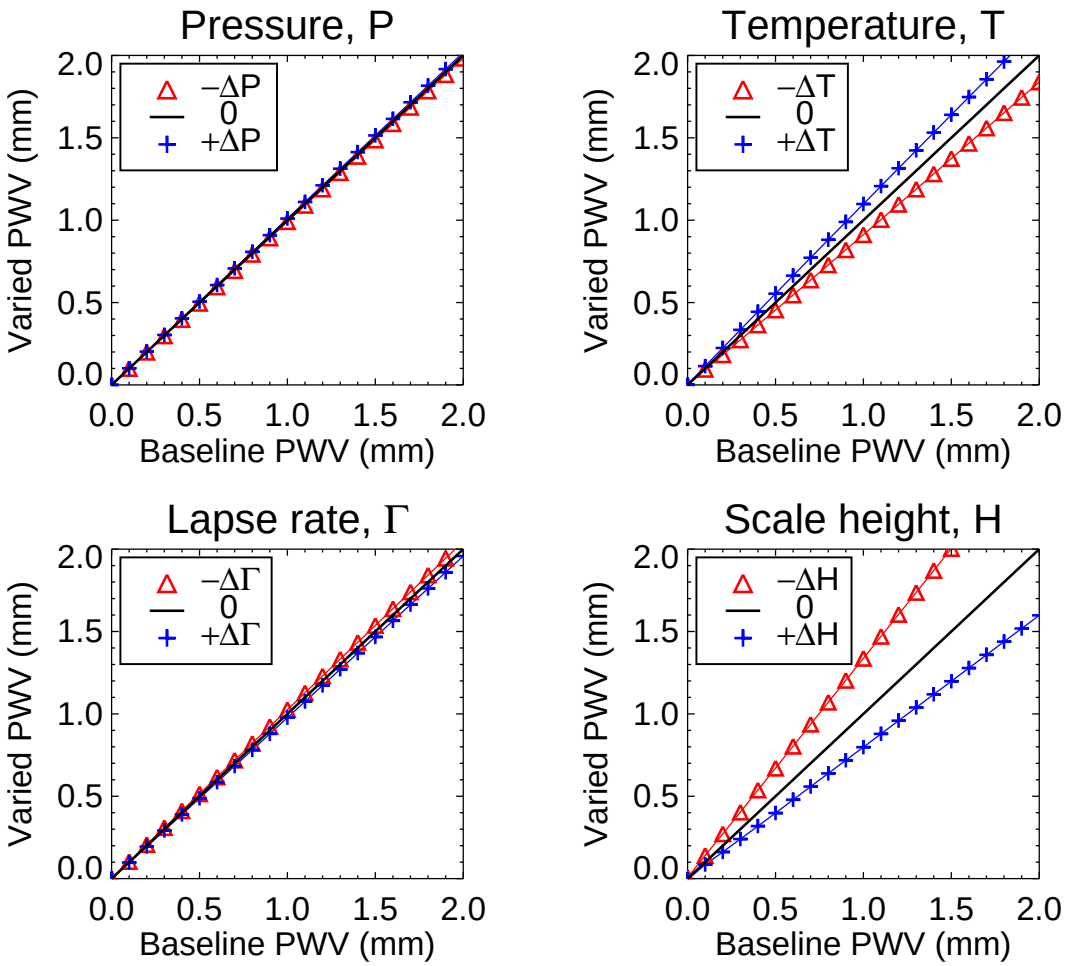

Figure 4.7: Sensitivity to PWV from varying surface P, surface T, Γ, and H for preliminary estimates of parameter uncertainties. PWV resulting from the varied parameter input is plotted versus PWV for unvaried parameter input. $\Delta P = \pm 1\%$, $\Delta T = \pm 1\%$, $\Delta \Gamma = \pm 10\%$, $\Delta H = \pm 25\%$. For each of the plots, the black lines represent X versus X, thus are the unity slope reference lines. Red triangles represent X versus $X - \Delta X$. Blue crosses represent X versus $X + \Delta X$. Increases in P and T result in increases to PWV. Increases in Γ and H result in decreases to PWV.

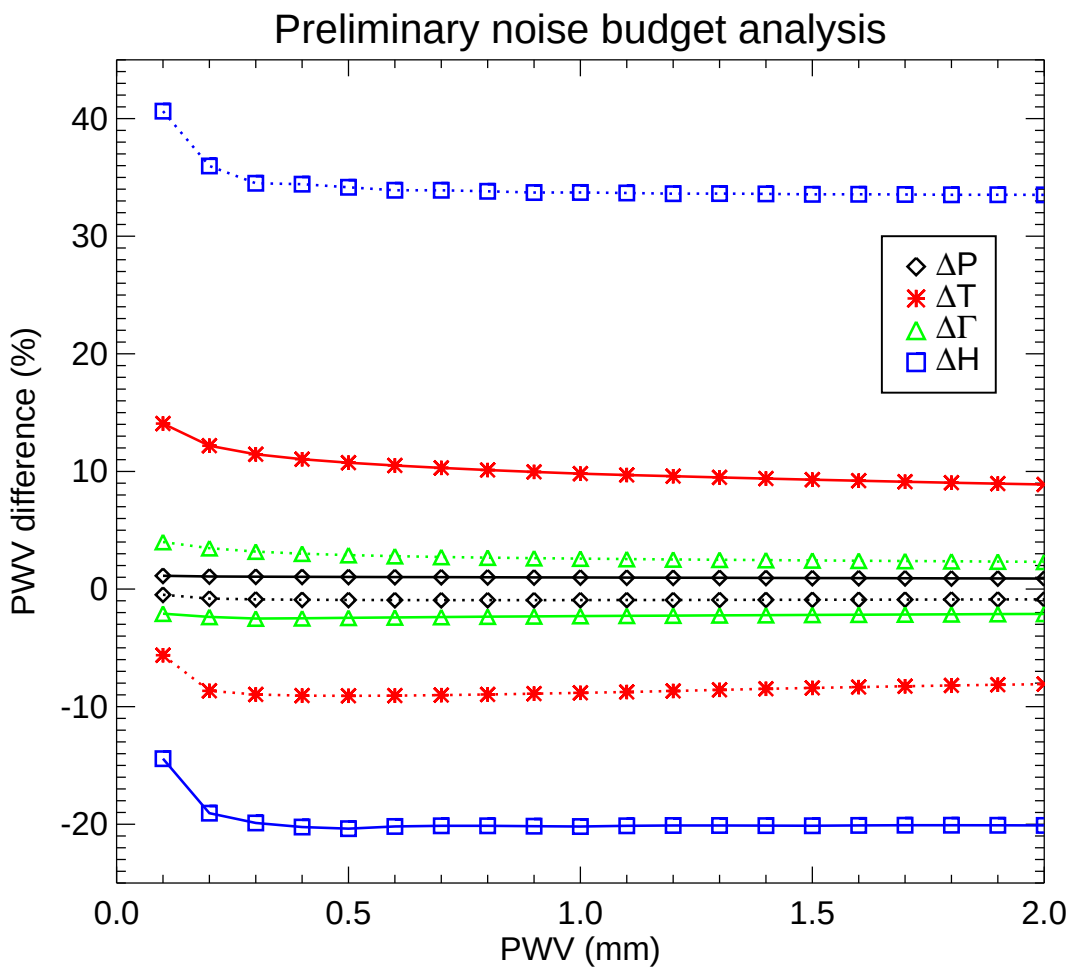

Figure 4.8: Noise budget for preliminary estimates of parameter uncertainties. Solid lines represent increasing the parameter value, $X \rightarrow X + \Delta X$, while the dotted lines represent decreasing the parameter value, $X \rightarrow X - \Delta X$. Increases in P and T result in increases to PWV, whereas increases in Γ and H result in decreases to PWV.

Here, for the case of the initial estimate, Base pressure and temperature were varied by $\pm 1\%$. PWV is more affected by changing temperature than by changing pressure, for the conditions shown, by a factor of $\sim$10:1. The temperature of the water vapour affects its line strengths and overall emission. Whereas changing the pressure affects the quantity of water vapour, i.e. density, and also the pressure broadening of the rotational transitions. Thus, for both base pressure and base temperature, an increase in the parameter value results in an increase to PWV.

Adiabatic lapse rate, Γ, was varied by $\pm 10\%$. An increase to Γ, results in a decrease to PWV. Adiabatic lapse rate is a negative number representing the rate of decrease in temperature for increasing altitude. A decrease to Γ, i.e. $\Gamma - \Delta\Gamma$, results in a larger negative number, representing a faster rate of cooling.

Scale height, H, was set to a nominal value of 2.0 km, and varied by 25%, resulting in the range of $H = 1.5$, 2.0, and 2.5 km. As was the case with adiabatic lapse rate, as scale height increases, PWV decreases. An increase in H means that a larger interval of altitude is required for a factor of $1/e$ decrease in water vapour. Thus the water vapour is effectively stretched more thinly over the height of the atmosphere. This would explain how an increase to scale height would result in a decrease to PWV.

The next section analyses the sensitivity results using actual parameter uncertainty values.

4.6.1 Ambient surface pressure and temperature

Ambient surface pressure, P, and ambient surface temperature, T, are the only physical measurements input to the model. These parameters can be measured in real-time to an accuracy of 0.1% using local meteorological equipment, unlike adiabatic lapse rate, Γ, and water vapour scale height, H, which must be determined statistically.

An atmospheric model for Antofagasta was created using the mean pressure and temperature profiles shown in Figures 4.1 and 4.2. Typical conditions for a Chilean astronomical site were input to the model. These include a base elevation $Z = 3000$ m, base $T = 275$ K, base $P = 72.0$ kPa, lapse rate $\Gamma = -6.95$ K km^{-1}, and a water vapour scale height $H = 2.0$ km. Atmospheric flux values were computed for PWV ranging from 0 to 3

Table 4.2: Sensitivity of PWV on ambient surface pressure

PWV (mm)	ΔPWV (mm)	ΔPWV (%)
0.5	±0.005	±1.0
1.0	±0.010	±1.0
2.0	±0.018	±0.9

Table 4.3: Sensitivity of PWV on ambient surface temperature

PWV (mm)	ΔPWV (mm)	ΔPWV (%)
0.5	±0.005	±1.0
1.0	±0.009	±0.9
2.0	±0.017	±0.8

mm. The PWV sensitivities at 0.5, 1.0, and 2.0 mm are given in the data tables.

Surface pressure was varied by ±0.1%. The associated change in PWV is reported in Table 4.2. $\Delta P = \pm 0.1\% \rightarrow \Delta\text{PWV} \approx \pm 1\%$. Variation to base pressure had insignificant effect on PWV. Surface temperature was also varied by ±0.1%. The results are reported in Table 4.3. PWV was far more reactive to variation in temperature: $\Delta T = \pm 0.1\% \rightarrow \Delta\text{PWV} \approx \pm 0.9\%$.

The atmospheric model used in this study, BTRAM [12], scales the surface temperature value with the adiabatic lapse rate up to an altitude of 12 km. Thus any change to surface temperature affects all mean layer temperatures up to 12 km. When BTRAM was developed, 12 km was chosen as a mean value for the height of the tropopause. Above 12 km, the lapse rate is no longer used to determine layer temperature. Default temperature values are taken from a representative atmospheric profile.

Table 4.4: Sensitivity of PWV on adiabatic lapse rate

PWV (mm)	ΔPWV (mm)	ΔPWV (%)
0.5	±0.00011	±0.022
1.0	±0.00019	±0.019
2.0	±0.00033	±0.017

4.6.2 Adiabatic lapse rate

The adiabatic lapse rate, Γ, was varied by ±0.13%, as determined by the uncertainty of the lapse rate value from §4.4: $\Gamma = -6.95 \pm 0.009$ K km^{-1}. The PWV sensitivity on varying lapse rate is reported in Table 4.4. Thus, parameter input values for Γ = [-6.94, -6.95, -6.96 K km^{-1}]. $\Delta\Gamma = \pm 0.13\% \rightarrow \Delta\text{PWV} \approx \pm 0.02\%$. The effect of varying adiabatic lapse rate of PWV was insignificant.

4.6.3 Scale height of water vapour

From the analysis of radiosonde derived scale heights described in §4.5 and shown in Figure 4.6, values for scale height have been derived as follows: mean $H \approx 1.4$ km, low $H \approx 1.1$ km, and high $H \approx 1.7$ km. Thus the range for H used in this study are $H =$ [1.1, 1.4, 1.7 km], equivalent to $\Delta H \approx \pm 21\%$. The PWV sensitivity on varying scale height is reported in Table 4.5. The uncertainty in scale height is by far the largest amongst the parameters being studied here. Thus, it is not surprising that the wide range of scale height used as the input parameter, results in a $\sim \pm 23\%$ change in PWV.

The data presented in Tables 4.2, 4.3, 4.4, and 4.5, are shown graphically in Figures 4.9 and 4.10. As was shown for Figures 4.7 and 4.8, the graphs represent the variation in the retrieved PWV value as a function of the assumed variation in the parameter. The

Table 4.5: Sensitivity of PWV on the scale height of water vapour

PWV (mm)	ΔPWV (mm)	ΔPWV (%)
0.5	±0.11	±23.0
1.0	±0.23	±22.7
2.0	±0.45	±22.6

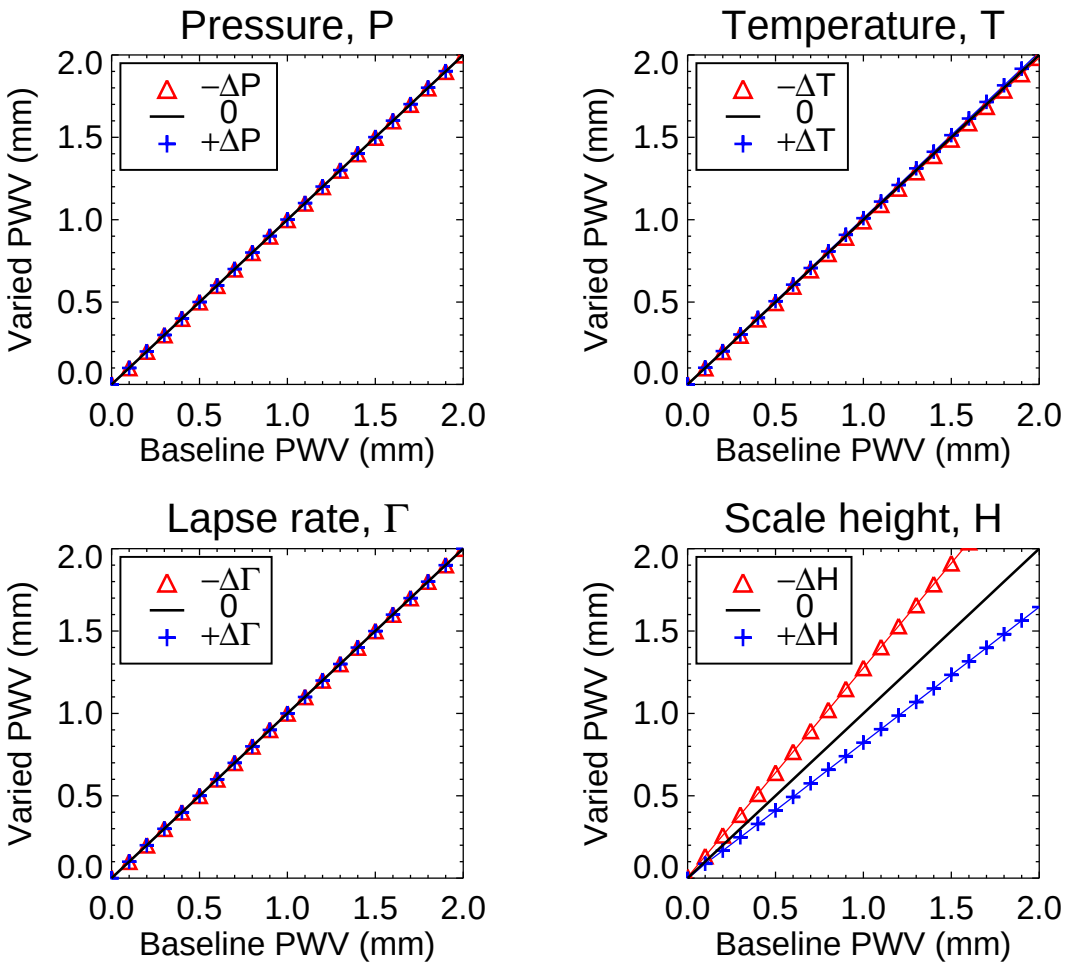

Figure 4.9: Sensitivity to PWV from varying surface P, surface T, Γ, and H for actual uncertainties in the site-specific parameter values. The uncertainties in all parameters except scale height are well known and insignificant to PWV sensitivity. Scale height has a large range of possible values, and its resulting effect on PWV is significant. PWV resulting from the varied parameter input is plotted versus PWV for unvaried parameter input. $\Delta P = \pm 0.1\%$, $\Delta T = \pm 0.1\%$, $\Delta \Gamma = \pm 0.13\%$, and $\Delta H = \pm 23\%$. For each of the plots, the black lines represent X versus X, thus are the unity slope reference lines. Red triangles represent X versus $X - \Delta X$. Blue crosses represent X versus $X + \Delta X$. Increases in P and T result in increases to PWV. Increases in Γ and H result in decreases to PWV.

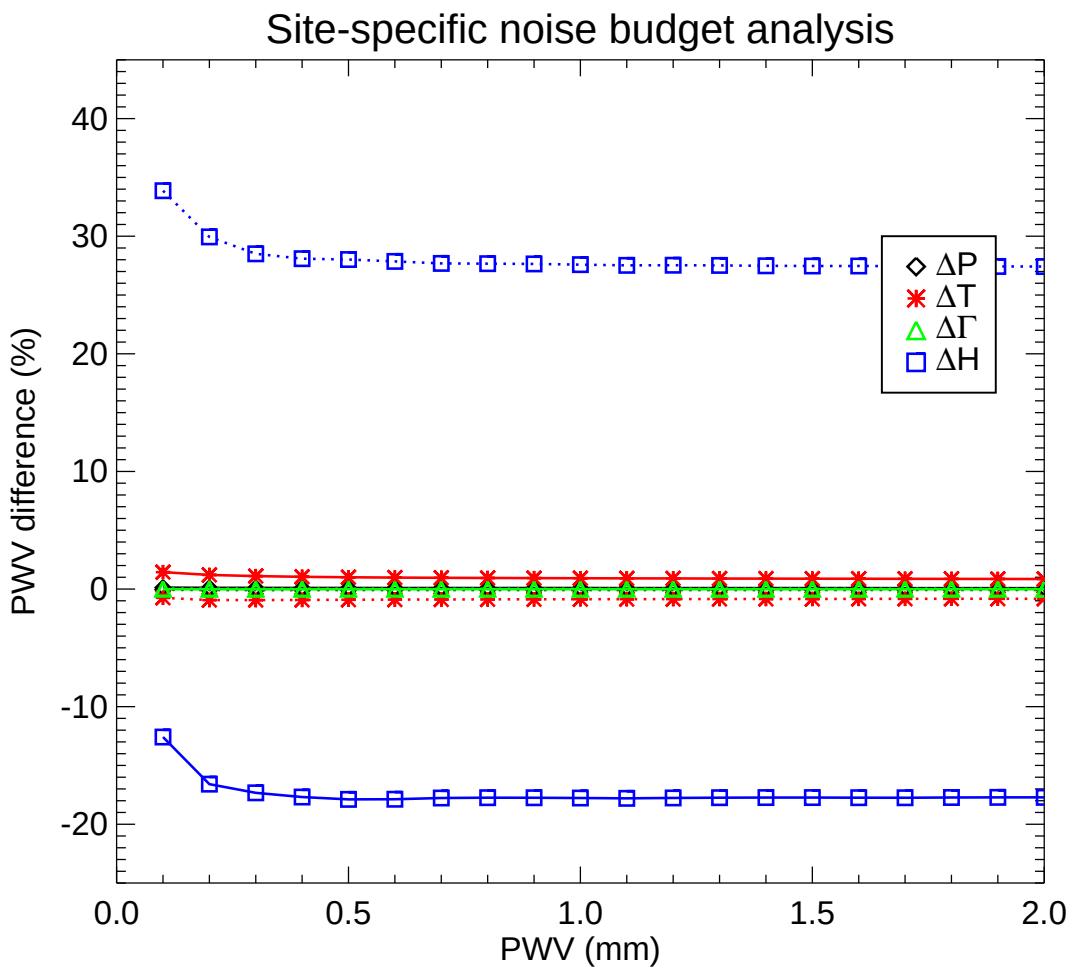

Figure 4.10: Noise budget analysis for site-specific parameter uncertainties. Solid lines represent increasing the parameter value, $X \rightarrow X + \Delta X$, while the dotted lines represent decreasing the parameter value, $X \rightarrow X - \Delta X$. Increases in P and T result in increases to PWV, whereas increases in Γ and H result in decreases to PWV.

base T, base P, and adiabatic lapse rate plots all show little sensitivity, due to their input uncertainties being well defined, and relatively small. Scale height is statistically derived and subject to a wider range of possible values than any other parameter being studied, which results in larger uncertainties in PWV. Therefore, any attempt at successfully modeling the atmosphere above any site, is limited by the uncertainty of the scale height of water vapour and its potential fluctuations over time.

4.7 Summary

It is now possible to take radiosonde data and create a regionally representative atmospheric model for any site on Earth. Temperature and pressure profiles can be created directly from the raw radiosonde data. Determination of adiabatic lapse rate and scale height of water vapour have been demonstrated using first principle calculations and statistical methods. The key parameters that drive the atmospheric model have been analysed in terms of how their variation affects resulting PWV output from the model. It was shown that scale height of water vapour is the parameter most affecting PWV sensitivity. While scale height of water vapour is critical to the accuracy of the model, it remains the most difficult to measure in real-time. Thus the need for statistical representation. In the next chapter I will describe the process of calibrating the IRMA instrument.

Chapter 5

Calibration

Calibration is arguably the most important part of any scientific experiment, and is often the component given the least attention. The evolution of this process as it applied to the IRMA instrument is outlined in this chapter.

5.1 Overview

Calibration is a central problem with any instrument. It is necessary to have a standard reference that measurements can be compared against. In earlier designs of the IRMA system [1], liquid nitrogen (LN_2), N_2, was used to cool the detector. This ample supply of LN_2 also allowed for the use of a LN_2 cold load as the cold baseline in a two-point calibration scheme, using a warmed blackbody as the hot reference point. The temperature of LN_2, ~77 K (~73 K on Mauna Kea), has effectively zero emission at 20 μm according to the Planck function, as seen in Figure 3.15. Therefore any flux measurements made of the LN_2 reference are instrumental in origin and can serve to establish an instrumental DC offset. The two calibration temperatures established boundaries well outside the range of

temperatures measured during normal operation.

Once the IRMA concept had been proven, the next step was to modify the design to allow for remote operation. Since remote sites were unlikely to have field personnel or a readily available supply of LN_2, the wet cryostat was replaced with a Stirling cycle Cryocooler [6]. Since the instrument no longer required LN_2 for operation, this also implied the elimination of the LN_2 cold blackbody. The two-point calibration method was preserved, replacing the LN_2 reference with an ambient blackbody reference, and allowing the reference to be heated to create a hot reference. Since both the ambient and the hot temperature flux measurements occur on the high-side of normal sky temperature flux measurements, an extrapolation to the sky temperature was required, as will be shown in Figure 5.2. This extrapolation required knowing the effective temperature of both the ambient and warmed blackbody to high precision, typically ± 0.1 K. The new two-point method was proved to be sufficient when IRMA was in the colder, more stable environmental conditions found at Mauna Kea. However, upon trying to do the same measurements and calibrations in the lower elevation locations in Chile, the method no longer proved adequate. It was assumed at this point that temperature gradients within the IRMA unit could be responsible. The justification for this argument was that the same methods applied to data in Chile produced systematic effects, that were not observed in Hawaii. Up to this point it had been assumed that the internal blackbody was well behaved.

However, when studied in detail, each was found to have non-uniform surface temperature and exhibited environmentally sensitive edge effects. One approach to study and correct for the edge effects of the smaller blackbodies was to construct a large diameter reference blackbody (LBB). As our understanding of the instrument grew, it quickly be-

came apparent that contaminating sources of infrared radiation were entering the detector. The measuring signal was sensitive to stray radiation. This led to a three-stage calibration between the LBB, the internal secondary calibration source, and the sky measurements described in §5.4. The individual internal, secondary calibration sources, can be referenced to trace back to the primary larger blackbody. Details to the calibration process are discussed in §5.4.

5.2 Evolution of the calibration process

IRMA has an infrared photodetector whose analog voltage is digitized using a Cirrus Logic 24-bit Delta-Sigma Analog-to-digital converter (ADC) [47]. The ADC has an input range of 0 — 2.5 V. This range is digitized into an integer from 1 to $2^{24} = 1,677,216$ counts. Thus the relationship between ADC counts and voltage is:

$$V = 2.5 \times \frac{\text{counts}}{2^{24}} \qquad \text{[Volts]} \quad . \tag{5.1}$$

Temperature diodes for use in the IRMA instrument, general purpose NPN 2N3904 transistors, were calibrated using a Lakeshore 340 Temperature Controller and temperature diode [48], and a Fisher Scientific 825F oven [49]. While supplying the transistors with a constant current, their voltages were measured. This was performed at two temperatures in the oven measured by the calibrated Lakeshore diode. This provided a two-point calibration for each of the transistors, referred to in the rest of the thesis as IRMA unit temperature diodes.

To first order, photodetector response is linear with respect to flux. This linear relationship is the basis for using the two-point temperature calibration. When relating

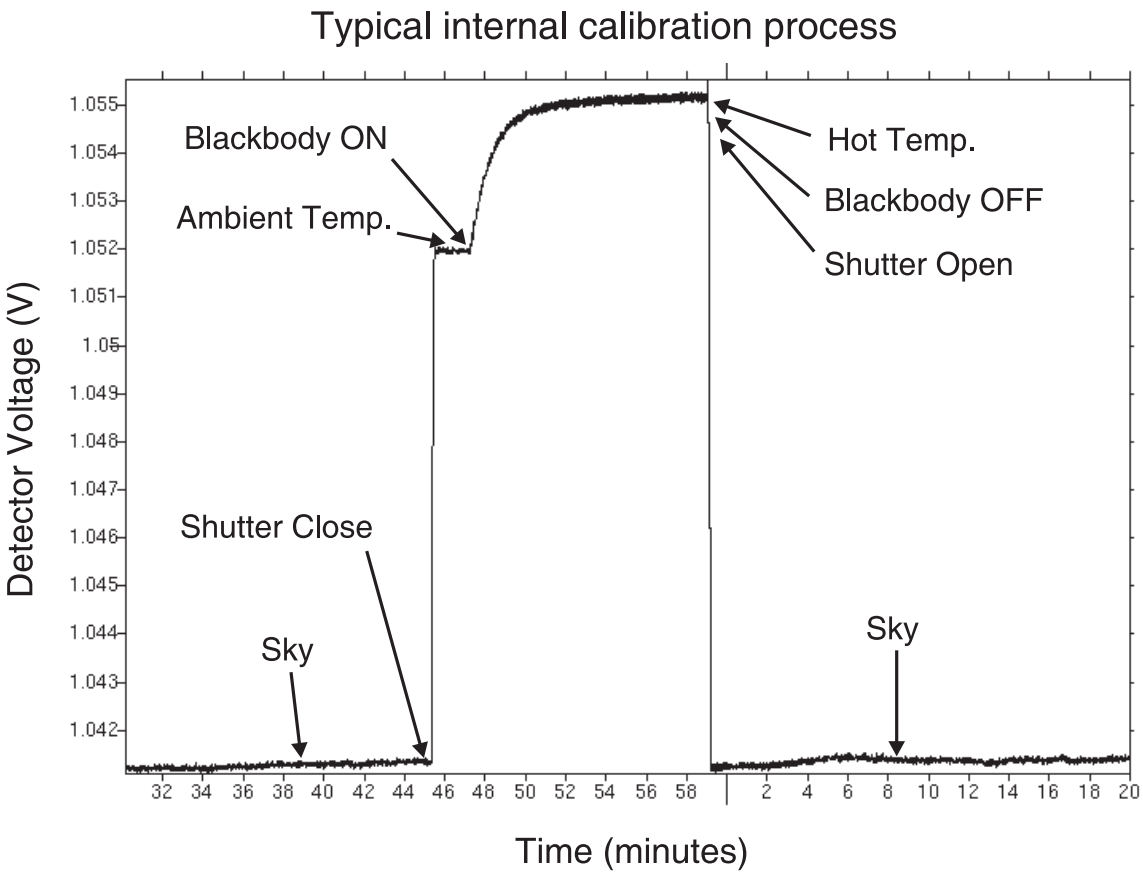

Figure 5.1: Detailed internal calibration curve/procedure for an IRMA unit.

surface temperature to emitted flux a non-linearity arises due to the Planck function. Thus, while there is linearity between the detector signal and input flux, when attempting to relate blackbody temperature to signal, the non-linearity of the Planck curve must be taken into account. Surface temperature values were scaled to account for the non-linearity. These corrected temperatures simplified the fitting procedure by allowed the calibration calculations to be performed in a linear temperature-space, as opposed to the non-linear flux-space. While there is a slight nonlinearity associated with the photoconductor response, for the flux levels encountered here, this effect is negligible.

To calibrate the photodetector, measurements of the lid blackbody are made at

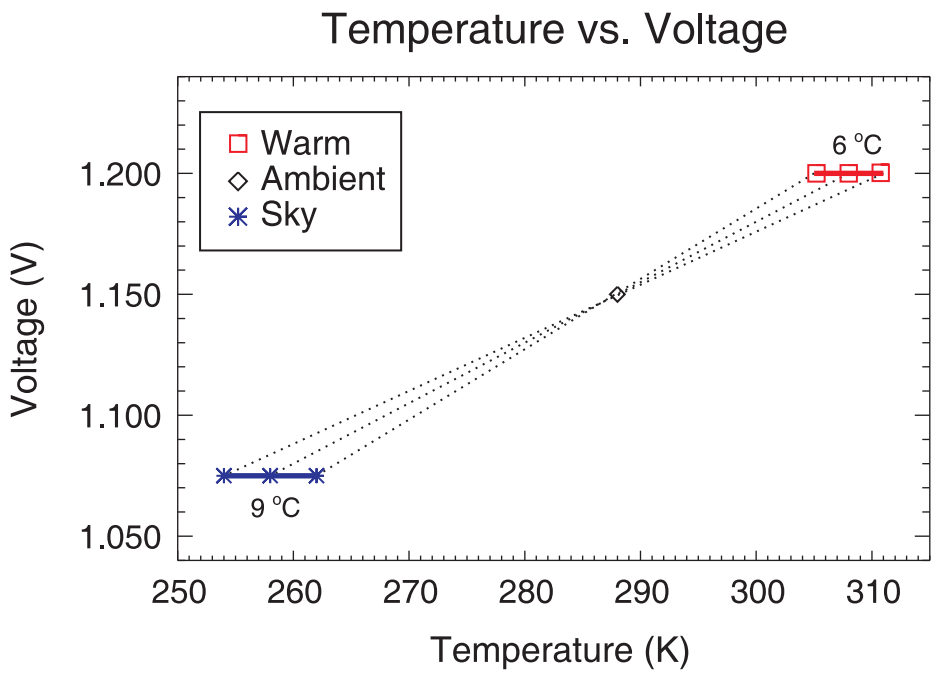

Figure 5.2: Potential sky temperature error introduced through two-point extrapolation. The ambient temperature is taken to have small error bars and acts as a fulcrum point. Warm temperature variance of ±3 K results in an extrapolated difference of ±4.5 K at sky temperature.

two different temperatures: one ambient, one warm. The detector signal voltage along with the temperatures of the lid blackbody are measured at the same time. The data are stored in a calibration file. Interpolation is used to relate all future detector measurements to a temperature (and subsequently to radiant flux) through this calibration file. Periodic re-calibrations are performed, and the nearest calibration data set (temporally) is used in the conversion from voltage to temperature. In the initial calibration procedure, this was all performed with the internal lid blackbody. Figure 5.1 depicts the internal calibration process. The voltage scale in this figure can equivalently be thought of as a temperature scale; the higher the voltage, the higher the effective temperature being measured by the detector. The entire calibration cycle takes on the order of 30 minutes, due primarily to the time necessary to warm the blackbody.

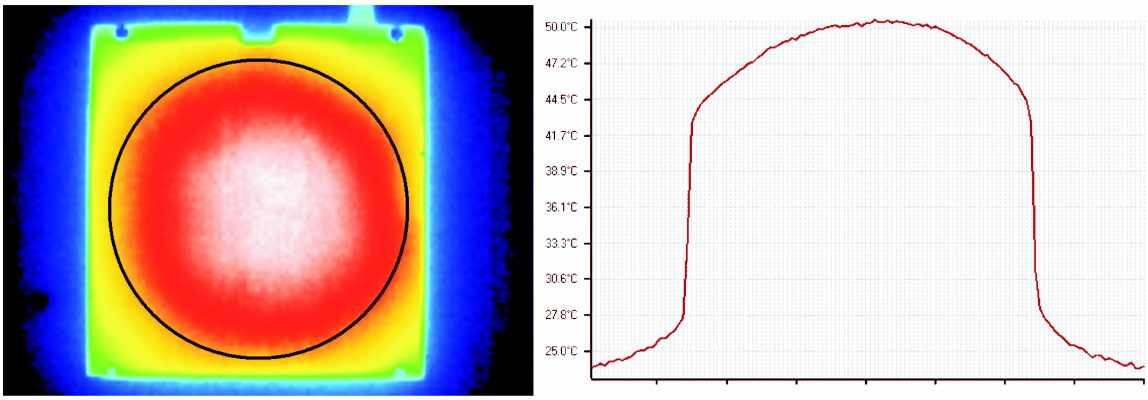

Figure 5.3: Thermal image of an internal lid blackbody taken with a Fluke Ti20 7-14 µm camera.

One difficulty encountered with the ambient/warm calibration temperature method is that these two temperatures are well outside the normal range of measurements made during normal operation (eg. ambient $T \approx$288 K , warm $T \approx$308 K, while sky $T \approx$258 K). Figure 5.2 shows this extrapolation. With a warm temperature range of $\pm$3 K, the resulting uncertainty at sky temperature is $\pm$4.5 K. This extrapolation places added importance on the accuracy of the ambient and warm temperature measurements. The ambient blackbody was assumed to be in a state of thermal equilibrium, and thus the sensor temperature was assumed to represent the temperature across the surface of the blackbody. However, when a heated blackbody was viewed with a Fluke Ti20 infrared camera on loan from Fluke, it was found that temperature gradients across the surface were significant, causing an overestimation of the flux emitted from the blackbody surface, as shown in Figure 5.3. Significant error had been introduced due to the incorrect assumption of uniform surface temperature.

The thermal gradient observed on the blackbody surface was circular, nearly Gaussian, and far from uniform. The central region was measured as $\sim$50$\pm$0.2 °C (323 K), while the edge was $\sim$46$\pm$ 0.2 °C (319 K). The area of the blackbody surface visible to the detector

(viewing port, circle of diameter 101.6 mm) is 8.1×10^3 mm^2. Unfortunately there were only two temperature sensors embedded in this blackbody, insufficient to investigate any thermal gradients. One sensor located at the centre and the other was located near one of the edges. This gradient would account for the $\sim$4 K difference measured between the two sensors. The temperature chosen to represent the surface was one of the two sensors, and from Figure 5.3, choosing either of the sensors was clearly not an accurate representation of the temperature profile across the surface. The correction to this gradient is described in the following section.

5.3 Effective temperature of the blackbody

As seen from Figure 5.3, the internal blackbody was warmest near the centre, with surface temperature decreasing towards the edges of the blackbody where it clearly exhibited edge effects as seen by the green and yellow bands in the figure. Thus it could be expected that any changes in the environment of the unit could cause changes in this gradient. For example the gradient measured in the controlled conditions of the laboratory, would be different than the gradients caused in the field by asymmetrical heating due to sunlight or wind conditions.

Using the information from the thermal camera, Figure 5.3, it was possible to identify and diagnose the problem. Using the Fluke data, I modeled the temperature gradient and determined the effective temperature of the blackbody based upon integrating the Planck curve over the blackbody area visible to the IRMA detector, using Equation 3.42. The thermal image had no scale, so the known dimensions of the lid (130×130 mm) were used to determine a scaling factor of 1.625 mm/pixel for this image. Therefore the

area of an individual pixel was 2.64 mm^2. Of the 128 × 96 Fluke microbolometer array pixels (12288 pixels total) the blackbody area visible to IRMA encompassed 2997 pixels. Of these 2997 relevant pixels, the maximum temperature was 50.6 ± 0.2* °C, minimum temperature was 45.8 ± 0.2 °C, and the mean temperature was 48.7 ± 0.2 °C.

The Planck function, as described in §3.6, gives the radiant energy in a given spectral band emitted from matter at a specific temperature. The total spectral radiance received by the photodetector depends on the throughput, $A\,\Omega$, and the instrument response function which varies with frequency, F_σ. The normalized, end-to-end, instrument response function incorporates the filter transmission profile, transmission through the anti-reflection (AR) coated ZnSe window, and the photodetector responsivity. The beam solid angle, Ω, is 7.80×10^{-6} sr. For IRMA, the integration range with values appreciably above zero is shown in Figure 5.4 as $\sim$ 450 — 575 cm^{-1} (equivalent to 17 — 22 μm). Thus, the total power detected by IRMA is given by:

$$S_T = \int_0^\infty \frac{2\,h\,c^2\,\sigma^3}{\exp\left(\dfrac{h\,c\,\sigma}{k_B\,T}\right) - 1} A\,\Omega\,F_\sigma\;d\sigma \qquad [\mathrm{W}]\quad . \tag{5.2}$$

To determine the effective temperature of the blackbody, the flux emitted from its surface needs to be calculated. The Planck function must be evaluated at the temperature of each individual pixel over the necessary spectral band given by the instrument response function, given in Figure 5.4. The total blackbody flux is computed by integrating across the instrument viewing area (flux emitted from all the visible pixels are summed). A custom made narrow band IR filter provided by Professor Peter Ade of the University of Cardiff, Wales, UK, limits the band of radiation that strikes the photodetector. To account for the

*Thermal sensitivity of the Fluke Ti20 is rated at ± 0.2 °C at 30 °C (303 K). The accuracy of the Fluke imager is rated at ± 2 °C or 2%, this was not relevant since the calibrated thermometry of the blackbody was used for absolute measurement.

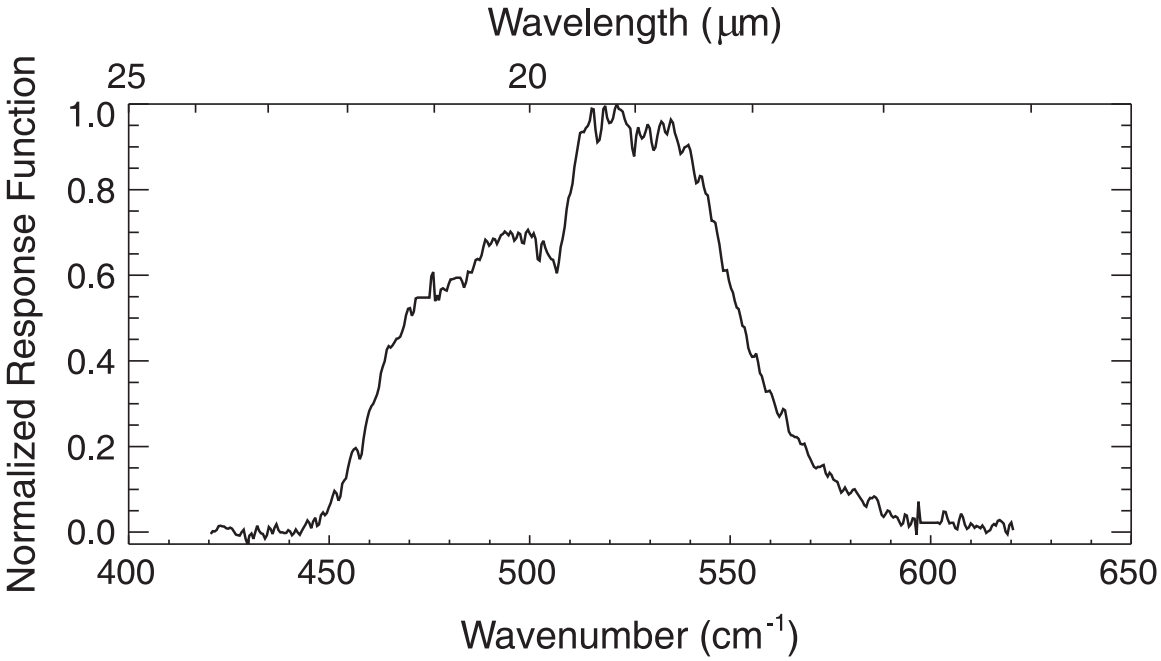

Figure 5.4: Normalized IRMA instrument response function as measured at 77 K using an ABB Bomem FTS. The profile is the end-to-end instrument response (the convolution of the filter transmission profile, transmission of the anti-reflection coated ZnSe window, and the photodetector response over the given spectral range).

effects of the filter, AR window, and detector responsivity, the total blackbody flux must be scaled by the instrument response function. The total blackbody area is calculated as 2997×2.64 mm^2 $= 7.91 \times 10^3$ mm^2. These summations over both spectral range and pixels leads to the results in Table 5.1. Assuming 100% transmission at the peak of the instrument response function, the measured gradient yielded a flux of 1.739×10^{-5} W; equivalent to the flux emitted from the same area if the surface temperature were a uniform 48.8 °C. In practice, the peak transmission of the instrument response function will not be 100%, however, this is irrelevant since all IRMA measurements are done by ratio. This is ~ 0.1 °C greater than the mean pixel temperature of 48.7 ± 0.2 °C. It should be noted that 0.1 °C is below the measurement sensitivity of the Fluke thermal camera, and thus the mean of the pixel temperatures (in this instance) can accurately represent the blackbody surface. The

Table 5.1: Results from the effective temperature calculations (assuming 100% transmission at the peak of the instrument response function).

Temperature Profile	[W] $\times 10^{-5}$	%diff
Measured Gradient	1.739	0
Uniform 50.6 °C (max T)	1.763	1.38
Uniform 48.7 °C (mean T)	1.737	0.12
Uniform 48.8 °C (effective T)	1.739	$\sim$0

non-linearities introduced by the Planck function were not sufficient to shift the effective temperature away from the mean pixel temperature.

Based on the above analysis, a correction term was incorporated for the warm blackbody temperature value. Rather than simply using the measured value from either of the two blackbody sensors to represent the warm blackbody, a composite effective temperature value was used, based upon the mean of the two sensors. On average, this method scaled the warm temperature values down by $\sim$3.5%. This correction was only valid within the controlled setting of the lab. Conditions of varying temperature gradients, as experienced in the field, could not be corrected for in this fashion. A more complicated correction was required, one that depended directly upon temperatures measured from inside the IRMA instrument, to better map the actual gradients. While this correction factor worked well in the lab, we still suffered the environmental effects discussed earlier.

5.4 Calibration procedure

Having observed the temperature gradients across the internal blackbodies with the Fluke camera, it was clear that the temperature recorded by the two embedded diodes could not be taken to represent the effective temperature of the surface as a whole. While a critical finding, it led us further along our journey of calibration.

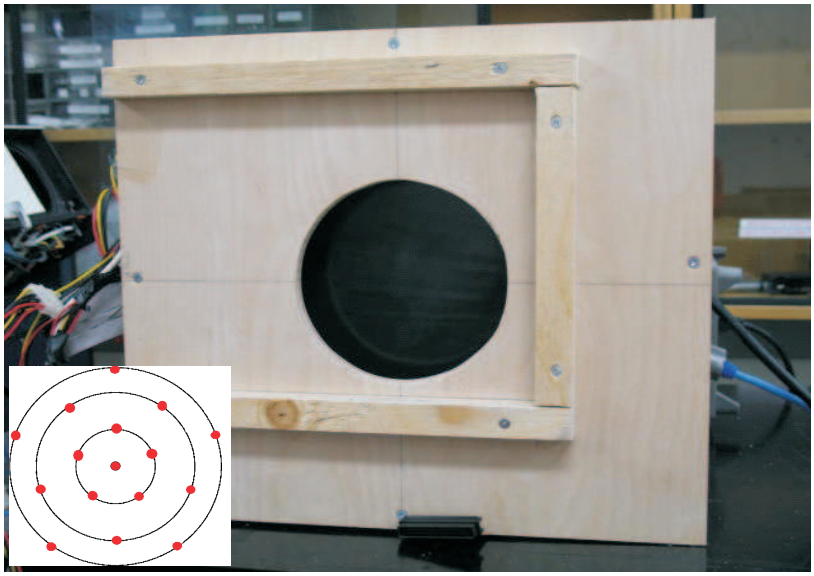

Figure 5.5: External view of the large reference blackbody (LBB). The wood frame allows the LBB to be accurately positioned atop an IRMA unit. Inset in the image is a representative mapping of the embedded temperature sensors. The circles diameters are 76.2 mm, 152.4 mm, and 203.2 mm respectively. The 5 sensors per circle are equally spaced leading to the pentagonal shapes in the modeled data. Analysis of Figure 5.6 determined that the effective temperature visible to IRMA could be based upon the mean value of the 6 centremost diodes.

To summarize the findings thus far: the internal blackbodies were found to have temperature gradients across their surfaces and associated edge effects that led to an overestimation of their effective temperatures. This contributed directly to an overestimation of flux emitted from their surfaces, that led to an overestimation of measured PWV.

In an attempt to address the challenges associated with the internal lid blackbodies, it was decided to construct a large diameter reference blackbody (LBB). The internal blackbodies were small and significant edge effects, and only had two embedded temperature sensors to map their entire surface. The reference blackbody was designed to be oversized to avoid edge effects, and had 16 temperature sensors embedded into its surface to allow for the accurate mapping of its surface temperature profile. Using the same LBB on different IRMA units served as a unifying primary calibration reference. A wooden housing was built to allow for repeatable positioning atop the IRMA viewing port, shown in Figure 5.5. The

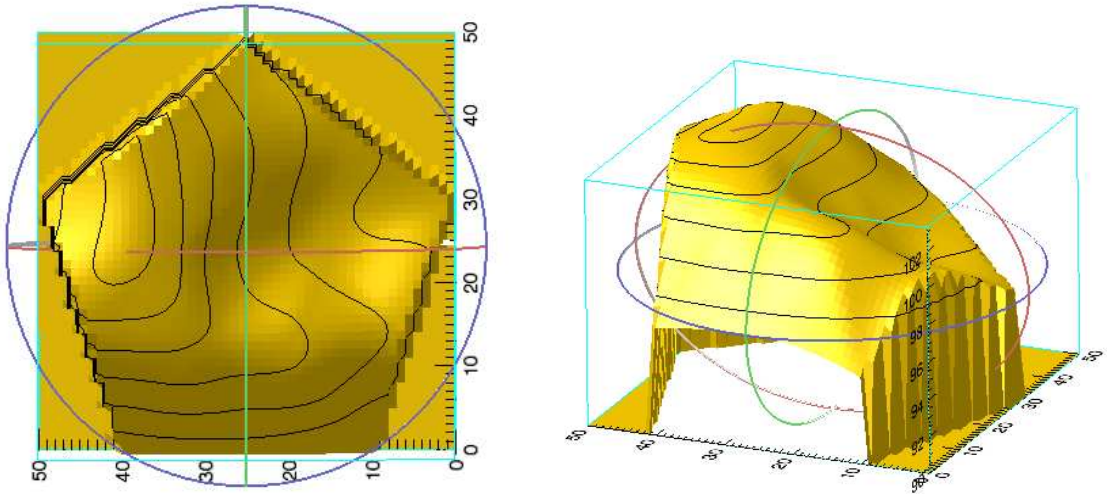

Figure 5.6: Modeled surface temperature for the large blackbody. The x-y axes are in arbitrary interpolation units resulting from the co-ordinate system conversion from polar to cartesian. The z-axis visible on the righthand plot is a temperature range from 90 — 102 °C. Each contour line represents 1 °C.

embedded silicon diodes were read using a dedicated USB data acquisition board (DAQ). Although there was still a gradient observed across the LBB surface, as seen in Figure 5.6, it was linear across the area visible to IRMA, and due to the large number of surface temperature sensors, the gradient across the surface could be mapped with little introduced interpolation error. It was determined from analysis of Figure 5.6 that the effective temperature visible to IRMA could be approximated by the mean value of the six temperature elements visible to IRMA (the centremost diode and the five diodes on the inner circle).

5.4.1 Optical alignment

The first step before the calibration process begins is to optimally position the detector assembly relative to the off-axis parabolic mirror. This alignment places the detector block at the focus of the mirror. This is achieved through having a relatively strong 20 μm source to view, in this case a heated plate of metal. The alignment heat source (AHS) was

Figure 5.7: Alignment heat source.

built for this purpose, see Figure 5.7. It is used for the alignment of the detector assembly within the IRMA unit. It consists of a hotplate with metal baffling and an insulating aperture of equal diameter to the IRMA viewing port. The AHS is placed $\sim$ 4 m away from the 90° off-axis parabolic mirror (OAP) along the instrument line-of-sight, this places it $\sim$40 focal lengths* away from the photodetector ensuring the image occurs at the focus of the OAP. The detector assembly is moved in one-dimension through the focal plane of the OAP while monitoring the photodetector voltage to maximize the signal.

5.4.2 Radiometric calibration

The motivation behind the radiometric calibration is to relate photodetector voltage to incoming flux using a single, consistent blackbody for all of the IRMA units, while

*The thin lens equation is given by: $\frac{1}{S_1} + \frac{1}{S_2} = \frac{1}{f}$, where S_1 is the object distance, S_2 is the image distance, and f is the focal length of the lens. As S_1 increases, $\frac{1}{S_1} \to 0$, image distance equals focal length.

incorporating internal IRMA temperatures in an attempt to identify and account for the effects of any stray radiation being measured by the detector that was not coming from the blackbody. Since the lid blackbodies are each custom made they differ slightly from each other across the IRMA units, and thus the importance of calibrating these different blackbodies with respect to a primary calibration standard.

Now that the detector is positioned at the focus of the OAP, the radiometric calibration can begin. This consists of a series of large black body (LBB) measurements interspersed with internal lid blackbody as discussed in §5.4 and shown in Figure 5.8. A typical calibration scheme consists of viewing the LBB at four distinct temperatures by applying DC voltages across the LBB heating element at 24 V, 30 V, 38 V, and 42 V. The LBB is able to reach its maximum temperature of $\sim$ 363 K ($\sim$90 °C) within 60 minutes.

A linear, least-squares fit was performed between the internal temperature map, the photodetector signal voltage, and the effective LBB temperature being viewed by IRMA.

The calibration/fit became a three step procedure:

Primary calibration:

A fit is performed between the detector voltage and the internal box temperature map with respect to the primary calibrator. Blackbody emission from the LBB is the effective temperature being viewed by IRMA, T_{LBB}, shown in red in Figure 5.1. The fit results in the following equation:

$$V = V_0 + c_{\mathrm{LBB}}\, T_{\mathrm{LBB}} + \sum_{i=0}^{n} c_i\, T_i \qquad [\mathrm{V}] \quad , \tag{5.3}$$

where V is photodetector voltage, V_0 is the offset term, c_{LBB} is the coefficient associated to the effective temperature being viewed by IRMA, and c_i are the n coefficients associ-

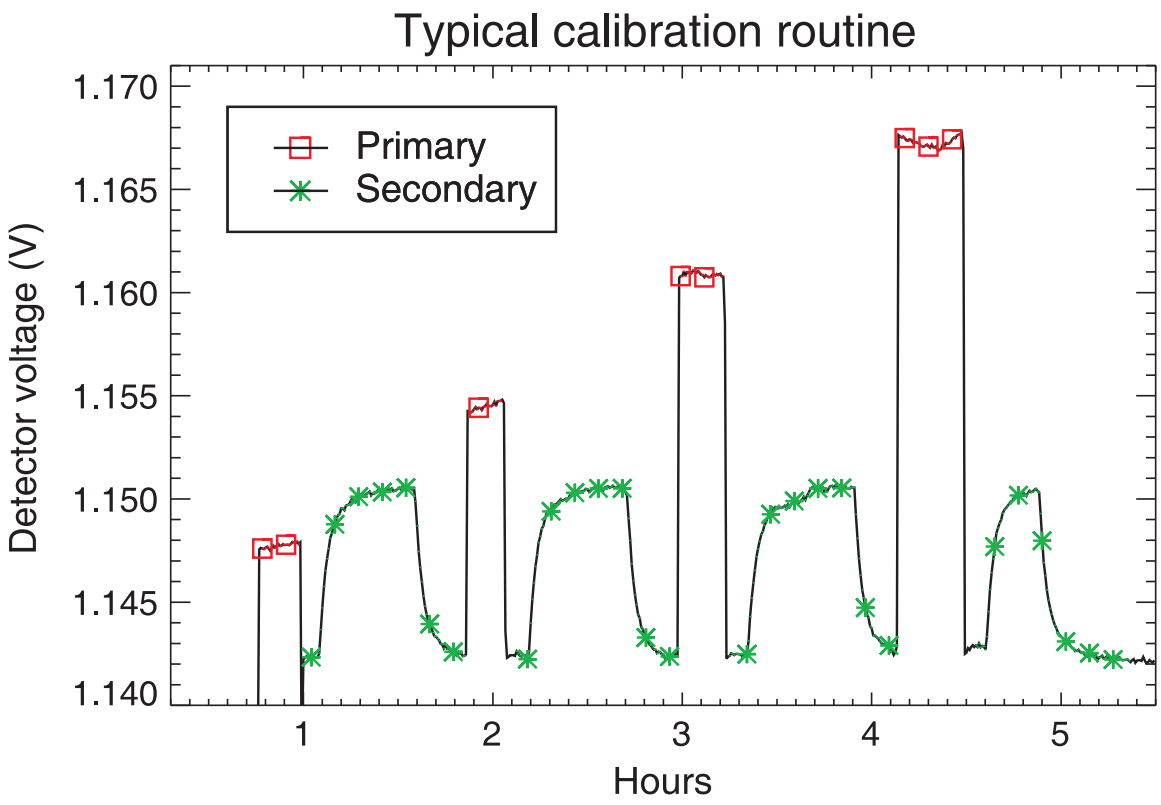

Figure 5.8: Typical calibration run performed in the lab. The black line is detector voltage, the red highlighted sections are the voltage when the large blackbody was being viewed (primary calibrator), the green highlighted sections are the voltage when the internal lid blackbody was being viewed (secondary calibrator).

ated to the n included internal temperature channels, T_i. These fit coefficients allow any combination of photodetector voltage and internal box temperatures to account for any contaminating stray radiation/flux viewed by IRMA to be identified and accounted for, as shown by rewriting Equation 5.3:

$$T_{\mathrm{LBB}} = \frac{V - V_0 - \sum_{i=0}^{n} c_i T_i}{c_{\mathrm{LBB}}} \qquad [\mathrm{K}] \quad . \tag{5.4}$$

Secondary calibration:

The internal blackbody is designed for periodic revalidation of the calibration whilst operating remotely in the field. For this calibration, a series of internal blackbody calibrations are performed, following the procedure outlined in Figure 5.1. These curves,

shown in green in Figure 5.8, are fitted to determine coefficients for the two temperature diodes embedded at the centre and edge of the lid blackbody. The resulting equation is given as:

$$T_{\text{LID}} = T_0 + c_1\,T_1 + c_2\,T_2 \qquad [\text{V}] \quad , \tag{5.5}$$

where T_0 is an offset term, T_1 and T_2 are the measured lid diode temperatures, and c_1 and c_2 are their fit coefficients. Although the lid temperature measurements may not accurately represent the temperature gradients across the surface, using Equation 5.5, it is now possible to reconstruct the effective temperature viewed by IRMA, in this case T_{LID}, based on the flux relationship derived using the primary calibrator. This is similar in nature to the correction term that was first devised from analysis of the Fluke data in section §5.3. Equating 5.4 and 5.5, the following relation is created:

$$T_0 + c_1\,T_1 + c_2\,T_2 = T_{\text{LID}} = T_{\text{LBB}} = \frac{V - V_0 - \sum_{i=0}^{n} c_i\,T_i}{c_{\text{LBB}}} \qquad . \tag{5.6}$$

Thus, using the coefficient c_{LBB} derived in the primary calibration, as the value for the coefficient c_{LID} it is possible to perform a field validation of the calibration using the internal lid blackbody, since the $V/T/$flux relation derived with the primary calibration is still valid. As an example the coefficients resulting from a fit performed on calibration data from the IRMA Gemini unit are shown in Table 5.2.

Calibrated sky measurement:

Using coefficients derived from the primary calibration (periodically validated and checked for parametric drift using the secondary calibration), sky measurements can be made using Equation 5.4, where T_{LBB} now represents T_{SKY} (since IRMA is viewing the sky,

Table 5.2: Example fit coefficients for the IRMA Gemini unit

Parameter	Coefficient value
T_{LBB}	0.0020820540
T sensor #6 (back wall behind cooler)	0.0047279932
T sensor #7 (floor in front of chopper)	-0.0057720618
V offset	1.0332378 V
Centre lid T	0.24492224
Edge lid T	0.66465639
T offset	4.2870716 K

not the calibration blackbody). Effective sky temperature, and thus sky flux, is readily converted to PWV through a pre-calculated site-dependent atmospheric model described in Chapter 4.

In summary, the flux from the large diameter reference blackbody (LBB) is viewed with IRMA while the LBB surface temperatures are measured with on-board thermometry. The primary calibration is performed, associating photodetector voltage to reference flux while accounting for stray radiation by mapping the internal temperatures of the instrument. The resulting relationship between instrumental data and effective input temperature, can be inverted to extract the effective temperature of the sky when provided with IRMA data (V and T_i) using Equation 5.4. The secondary calibration is not essential to the sky measurement process, but serves as a field validation of the calibration.

Determining which combination of internal temperature sensors to use in the fit is a non-trivial exercise. There are 16 temperature diodes in an IRMA unit. Of these 16 sensors, only 6 are located within the optical cavity of the instrument, and can thus potentially account for stray radiation. A statistical approach is taken to determine which

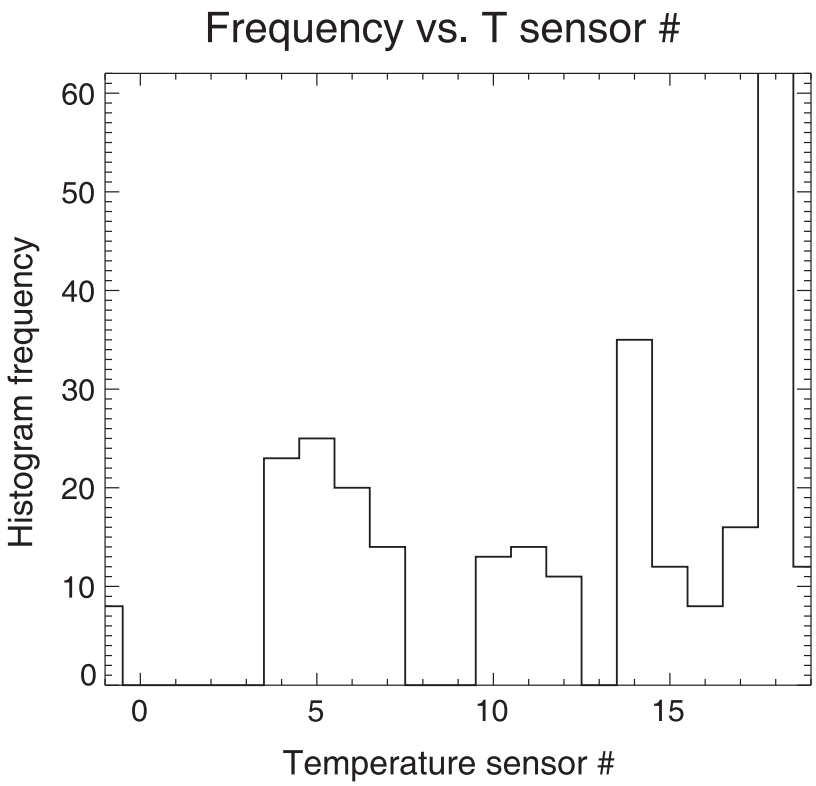

Figure 5.9: Histogram of temperature sensors resulting in a "best" fit to data set from primary calibration. All possible two and three sensor combinations were fitted to the primary calibration data set. Sensor #18 has the highest frequency, and thus occurs most in the "best" combinations. If selecting only two sensors to use in Equation 5.4, for this calibration data set, sensor #18 would be selected as the dominant/primary temperature sensor, and sensor #14 would be chosen as the secondary sensor. Sensor #14 is located on the inner wall (electronics side) and sensor #18 is located on the outer wall (optical cavity side) as seen in Figure 1.6.

of the 6 sensors are best suited to represent the stray radiation. All relevant combinations of sensors are fitted to a set of primary calibration data using Equation 5.4. The standard deviation, σ, of the difference between the fits and the measured T_{LBB} are computed. The temperature sensor combinations resulting in the lowest σ data are plotted in histogram form, shown in Figure 5.9. From the histogram, it is apparent that sensor #18 occurs with the highest frequency, and can thus be considered to be in the primary location to account for the stray radiation. Similarly, sensor #14 is also relevantly located within the IRMA unit. Sensor #14 is located on the inner wall (electronics side) and sensor #18 is located

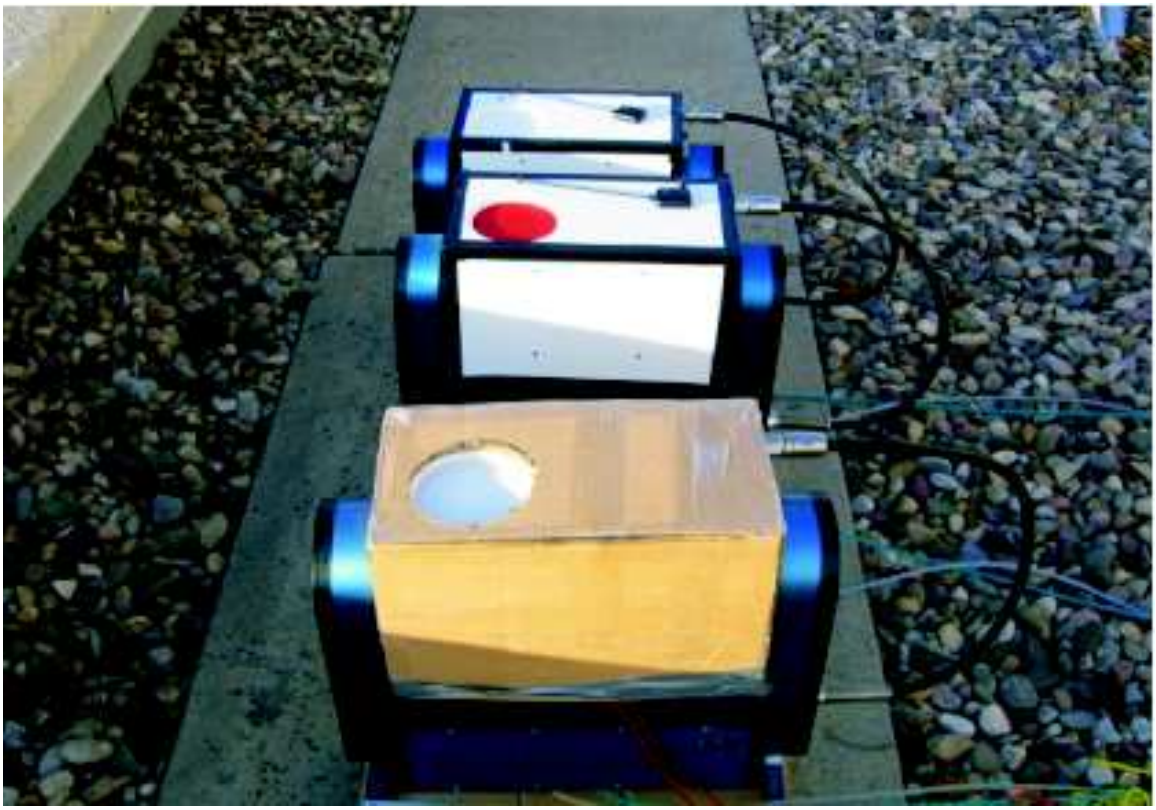

Figure 5.10: Three IRMA units on the roof at the University of Lethbridge. One is fitted with a heating cable and insulating jacket (cardboard) to test the ability of the fitting routine to correctly account for and remove the systematic offset due to heating.

on the outer wall (optical cavity side). From the data set depicted in the histogram, the fit coefficients and temperature data from sensors #14 and #18 are selected as the "best" combination of temperature sensors to use with Equation 5.4 to evaluate sky measurements.

5.5 Results

Now that we have identified that the photodetector signal depends upon internal temperatures within the IRMA unit, and having derived methods to account for the effects of this stray radiation, the next step is to apply the correction to a controlled situation and determine how well it performs. The most rigourous test of the calibration and stray

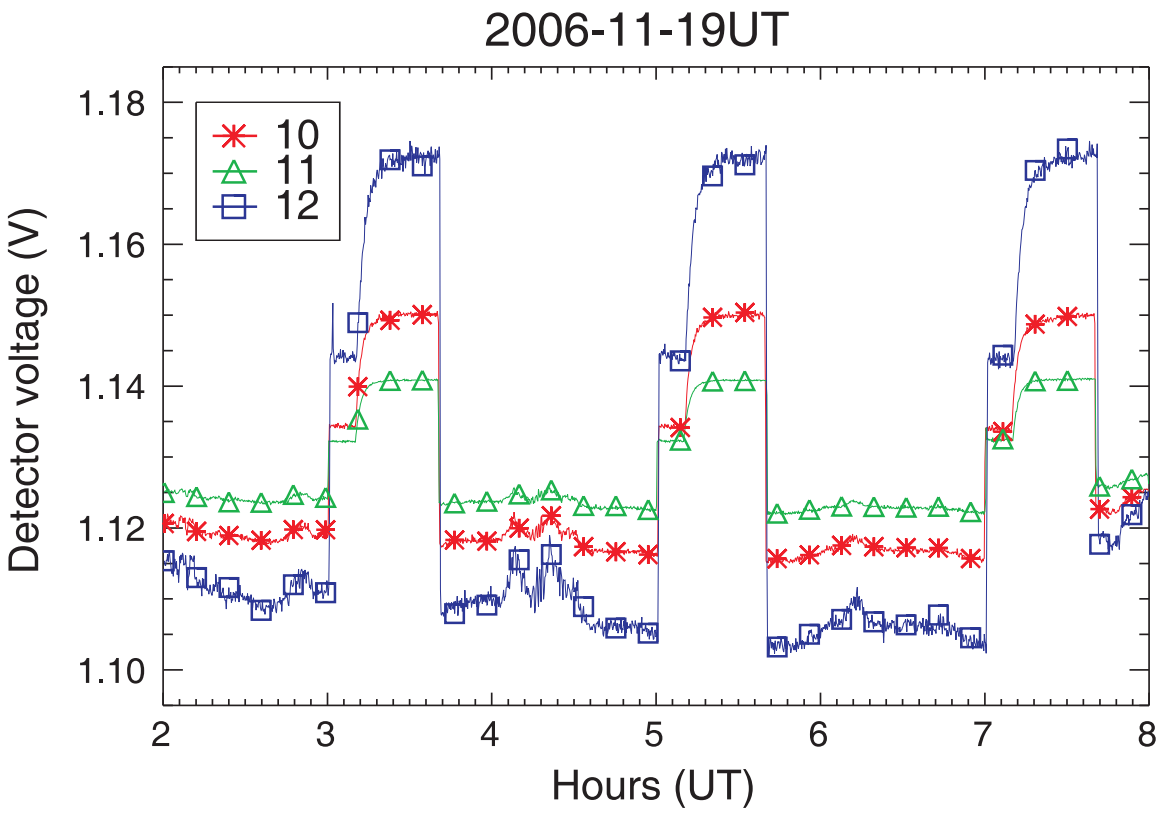

Figure 5.11: Raw voltage data for three co-located IRMA units in Lethbridge. The characteristic calibration curves can be seen in all three data sets.

radiation correction is to independently calibrate several IRMA units with respect to the same primary calibrator, install them in the same location measuring the same patch of sky, and vary the temperatures across the IRMA units. If the correction was successfully applied, the expected result would be equivalent PWV readings from each of the calibrated units, independent of individual differences in system temperature.

Three units were calibrated using the primary calibration routine. They were installed on the roof of the University of Lethbridge (directly above our lab). Figure 5.10 shows the three IRMA units co-located on the roof. To simulate varying temperature conditions across the IRMA units, one of the units in this photograph was fitted with a heating cable, and had an insulating (cardboard) jacket affixed to it. The heated unit

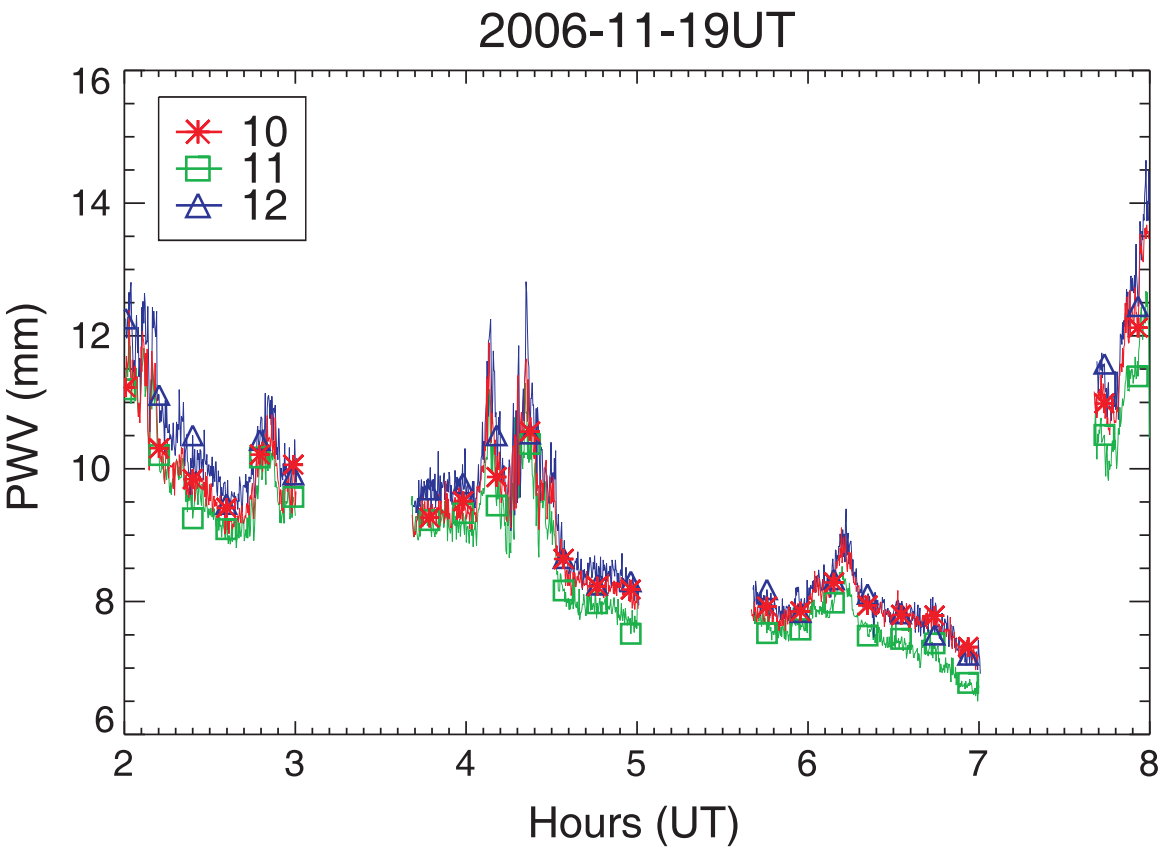

Figure 5.12: PWV values for three co-located IRMA units in Lethbridge. The high PWV data points near the edges of data are due to measurements of the lid, not sky measurements.

was warmed ∼10 K above ambient. The calibration was able to correctly account for this systematic heating, subsequently reducing the 10 K systematic to ∼2 K. This was the first success provided by the calibration process.

The next test of the calibration process, was to have different units measure the same sky and hopefully report equal values for PWV. Sky measurements were made with the three units while they were co-located in Lethbridge. Figure 5.11 shows the raw signal voltages for the three IRMA instruments. Three internal calibration curves (as seen in Figure 5.1) are present in each data set starting at 3 hours, 5 hours, and 7 hours. Each IRMA unit (Box 10, 11, and 12) have significantly differing gain and offset value from

one another. Another test of the calibration process will be to bring these gain and offset differences into alignment across the three units.

Application of the calibration method converts the detector signal voltage and internal box temperatures into flux, and then PWV through the atmospheric model. A rudimentary atmospheric model was created for Lethbridge, Alberta, Canada (49° 40' 47.53" N, 112° 51' 39.38" W), based on the mid-latitude winter profile with base $P = 90.0$ kPa, base $Z = 900$ m, and base $T = 288$ K.

The PWV results for the sky measurements are shown in Figure 5.12. The calibration procedure was able to bring the detector signal data into good agreement. There is a small spread visible in the PWV data, however, no median-filtering or complex data manipulation has been applied, which will serve to reduce this spread. IRMA was designed to measure water vapour below ∼2 mm. Above 2 mm, the spectral lines for water vapour begin to saturate, thereby reducing the sensitivity of the instrument to detect changes PWV. The PWV for this data set in Lethbridge ranges from ~ 7 — 14 mm. While this is far above the designed sensitivity range of the instrument, the resulting correlation between the three instruments is still quite good.

Another way of visualizing the intercomparison of co-located IRMA measurements is by plotting the data as a scatter plot. PWV measurements from one unit are plotted versus the PWV measurements from a second IRMA unit. The PWV data from Figure 5.12 is presented again in Figure 5.13 as a scatter plot.

If the measurements from two IRMA units matched perfectly, all data points would fall along a reference line of unity slope, represented by the solid black line. For site selection purposes, TMT requires intercomparability of absolute PWV measurements made

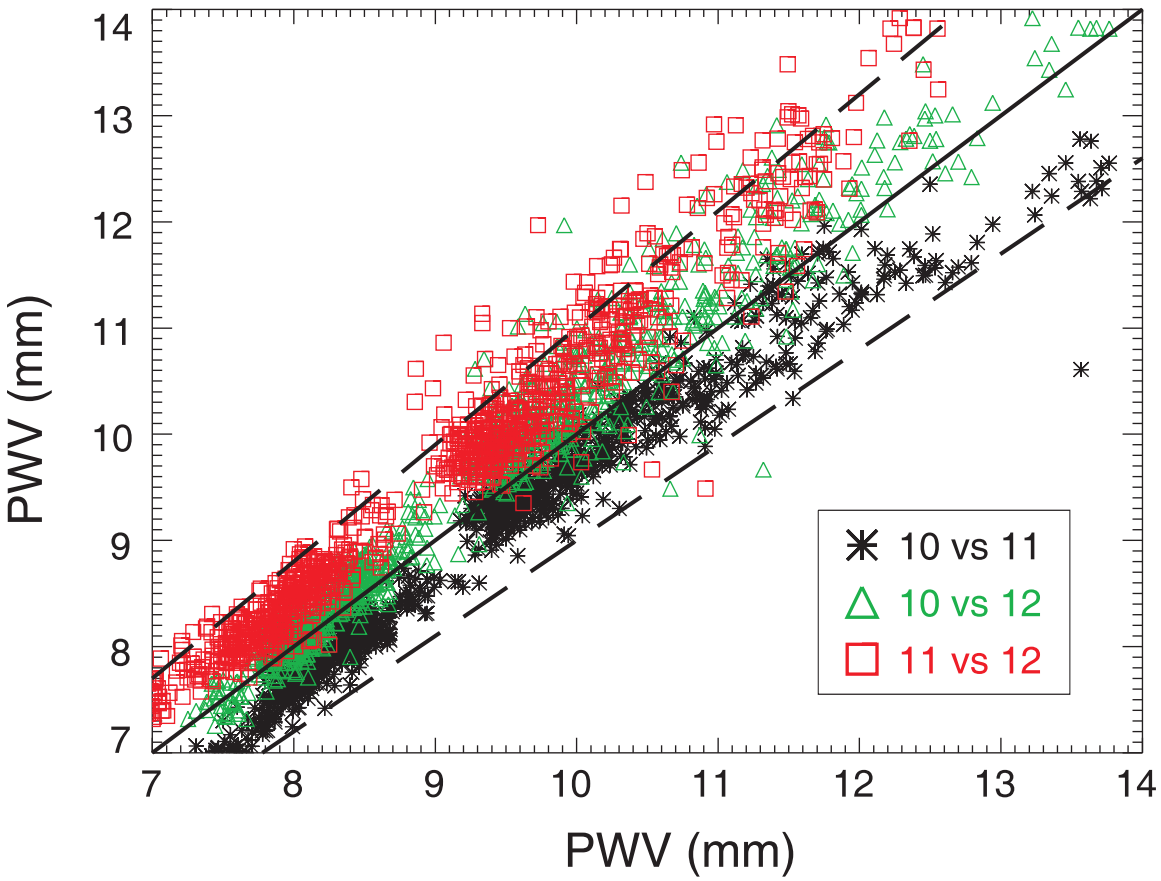

Figure 5.13: Intercomparison scatter plot for PWV data from three co-located IRMA units in Lethbridge. The data sets are each box as compared with the others. The solid line is the ideal unity slope reference line, while dashed lines are the ±10% tolerance limits.

by IRMA units on the order of 0.1 mm at 1.0 mm PWV: 10% absolute PWV. The dashed lines represent these ± 10% TMT measurement tolerance boundaries. Overall, most of the data fall within the 10% range, however, each data set has even less spread when examined in detail. For example, the box 10 vs. box 11 data set (black asterisks), has a spread on the order of ± 0.2 mm. This data set has a systematic offset below the reference line and both other data sets. Similarly, the box 11 vs. box 12 data set (red squares) is offset in the other direction, above the unity slope reference line. Again these data values are between 7 and 14 mm which is much higher than the 2 mm at which we begin to lose confidence in

Figure 5.14: Three IRMA units co-located in Chile at ∼3000 m. Greg Tompkins is inspecting the units.

the accuracy/sensitivity of the photodetector. Also, as PWV increases a larger spread is observed, as expected.

After the calibrating and testing had been completed in Lethbridge, the three units were shipped to Chile. Upon arrival, they were set-up at the Chilean mountain top site at an altitude of ∼3000 m, shown in Figure 5.14. While located there, the IRMA units made simultaneous measurements of the same patch of sky, represented in a PWV vs time plot in Figure 5.15 and the scatter plot in Figure 5.16.

The spread is much tighter when compared to the Lethbridge data, which is to be expected since the site is ∼2000 m higher in altitude than Lethbridge, and accordingly, has less water vapour present in the atmosphere to emit. The data again fall within the 10% tolerance limits before statistical averaging or manipulation of the data. The spread in the data, and the shift of each data set with respect to the others is still being studied, and is

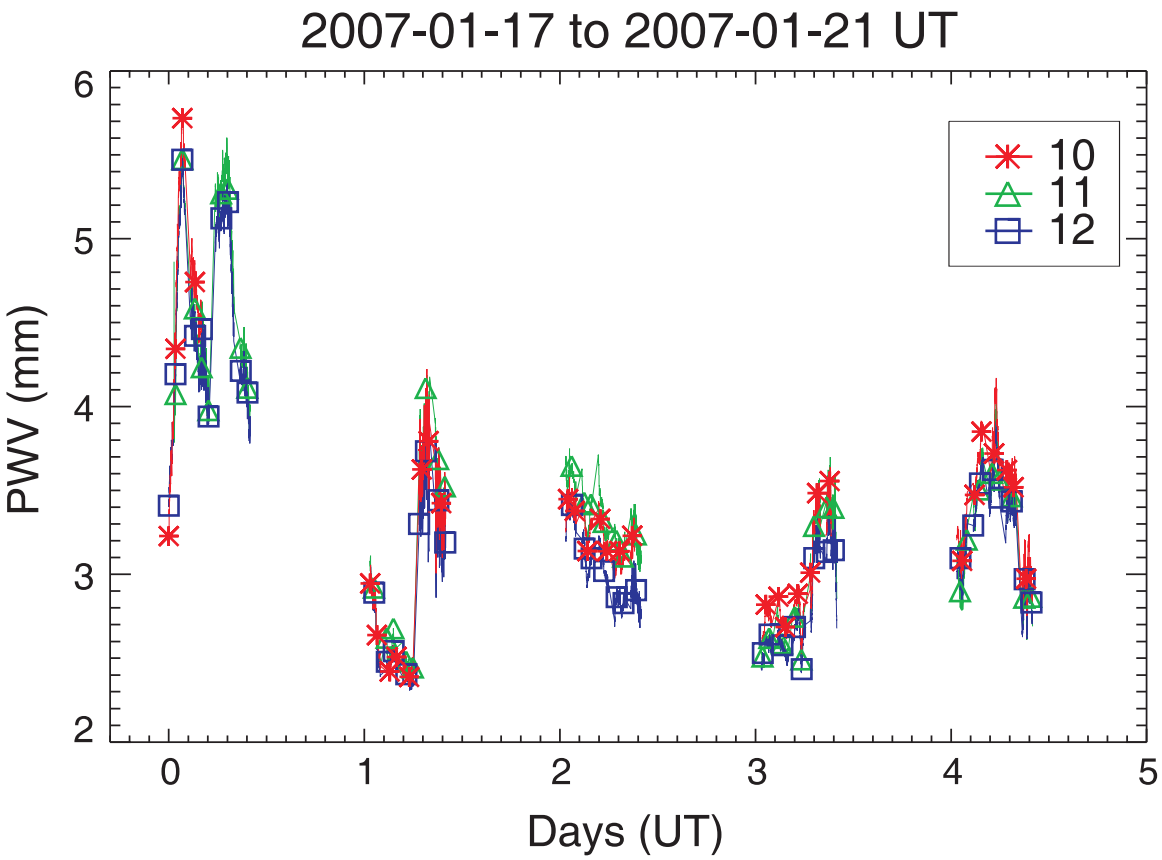

Figure 5.15: PWV values for three co-located IRMA units in Chile.

likely due to second order effects that are currently under investigation.

5.6 Analysis for site testing

The data produced by IRMA is being used to determine, quantitatively, the observing potential of each of the TMT candidate sites. The first approach is to plot the precipitable water vapour column data for a given site over a long period of time as a cumulative distribution function, as shown in the lower plot of Figure 5.17. The figure shows approximately 60 nights of PWV measurements made by one of the IRMA units at one of the potential TMT sites in Chile during 2007. This data shows that over this duration of

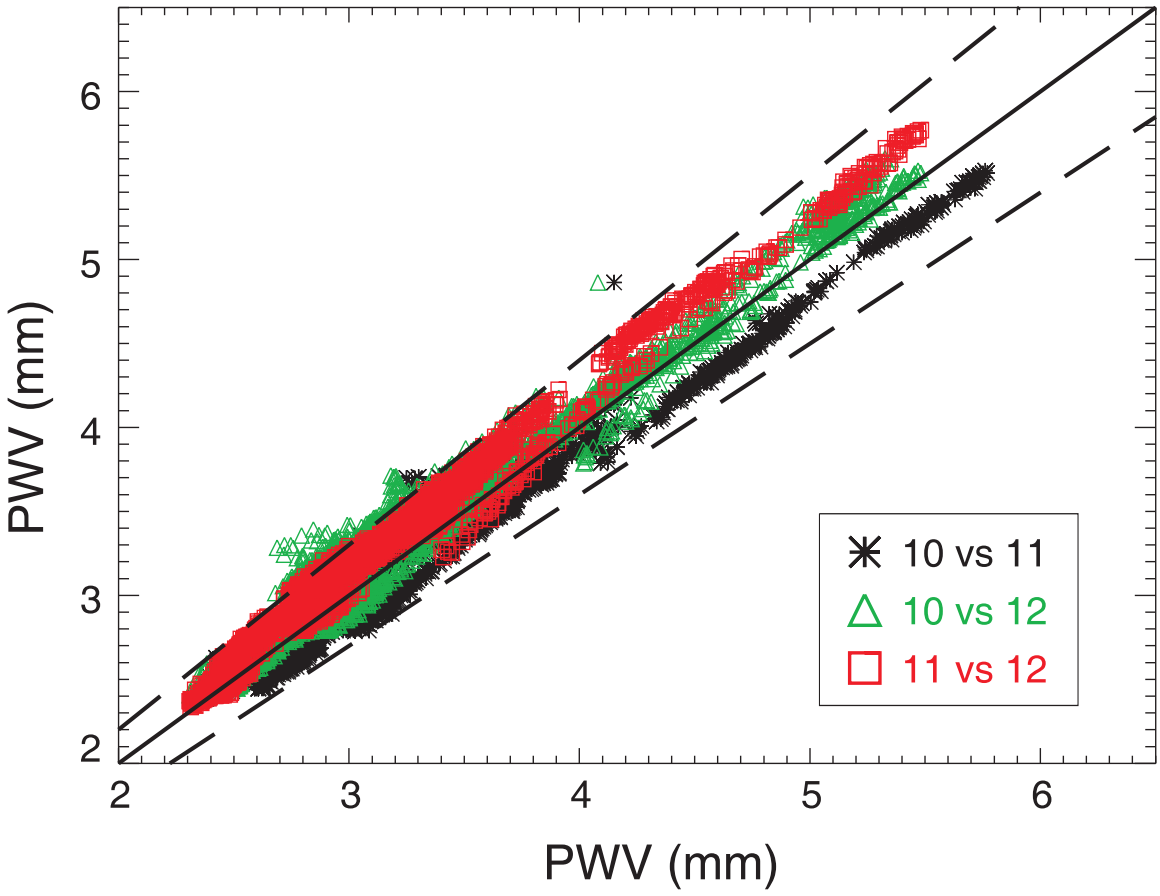

Figure 5.16: Intercomparison scatter plot for PWV data from three co-located IRMA units in Chile. The data sets are each box as compared with the others. The solid line is the ideal unity slope reference, while dashed lines are the ±10% tolerance limits.

measurements, 78 % of the observations were adequate for astronomical observing (< 5 mm PWV) and ∼ 0 % of the observations represented excellent observing conditions (< 1 mm PWV). PWV is directly related to atmospheric opacity at infrared wavelengths because water vapour rotational transitions in this region dominate the spectrum. The lower the PWV, the lower the atmospheric emission due to water vapour, and therefore the lower the overall opacity of the sky. The ideal candidate site would have 100 % of the observations occurring at zero mm PWV. This is unphysical for the Earth's atmosphere, however, PWV values below 1 mm are possible. To properly evaluate sites and choose between them, it is

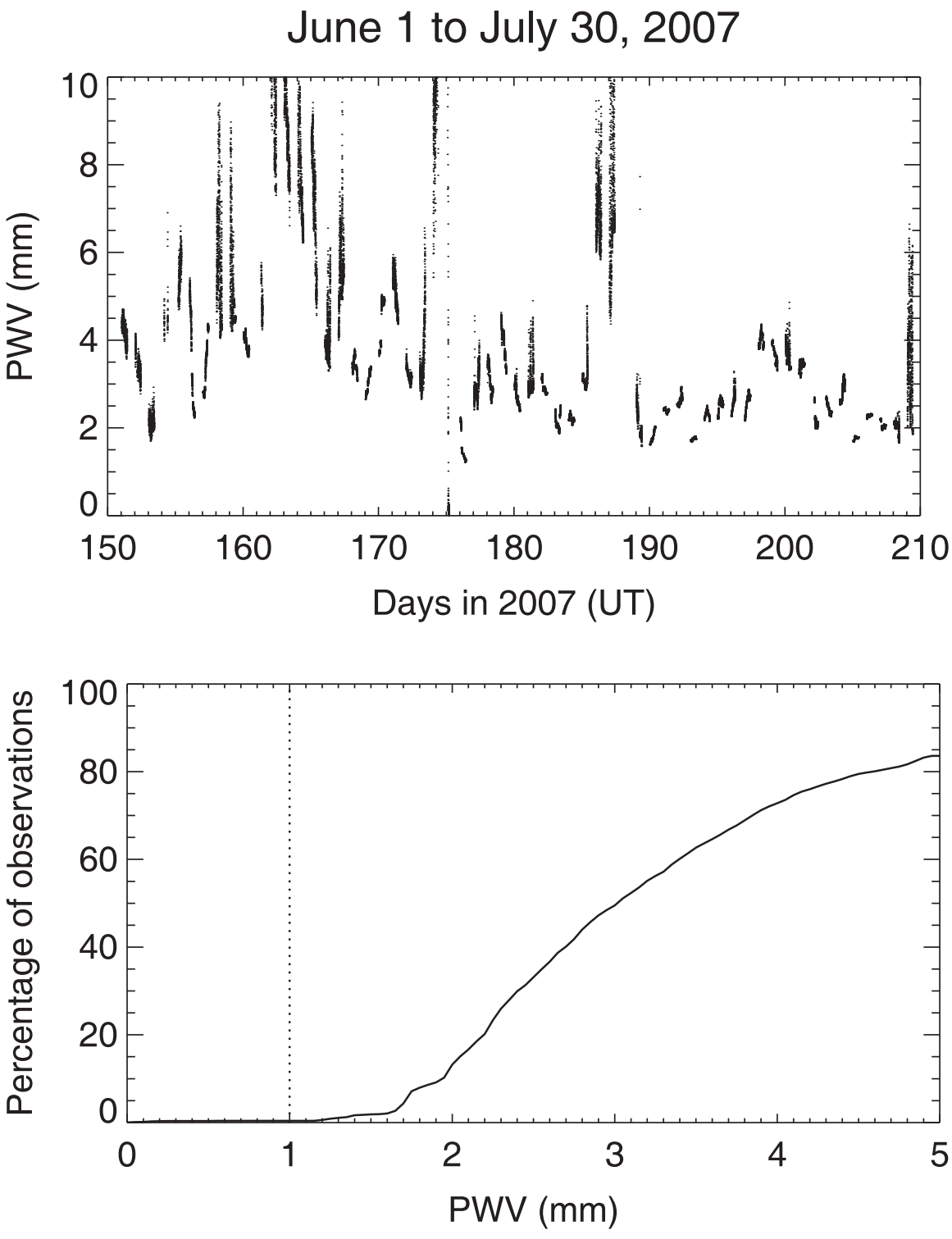

Figure 5.17: 2 months of nighttime IRMA data measured in Chile. Top plot is the measured PWV versus time measured by days in 2007 UT. The lower plot is a cumulative distribution of the same PWV measurements presented in terms of their percentage of observation. The dotted line is at 1 mm PWV, which is considered a low amount of PWV, and thus good conditions for astronomical observing.

necessary to determine the specific qualities that would make the site a good choice. Such qualities could include overall lowest PWV achieved, or highest percentage of observations at the lowest possible PWV. However, the choice will most likely be based on the type of science to be performed at the site. This is because some types of astronomical observations require pristine atmospheric conditions, while others require only average sky conditions to perform their science. Whether 80 % average conditions is deemed better than 1 % outstanding conditions will be decided upon based on a metric put together by the TMT site selection committee.

5.7 Summary

In this chapter it has been shown that systematic effects due to stray radiation within the IRMA units can be both identified and accounted for through a calibration scheme that includes internal IRMA box temperatures. Three IRMA units were independently calibrated using a large diameter reference blackbody constructed expressly for this purpose. Calibrated PWV data from co-located measurements made in Lethbridge and Chile were also presented. The Lethbridge data represents relatively high PWV conditions, while the Chilean data represents relatively low PWV conditions. Under both the high PWV and low PWV conditions, the three calibrated units showed a high degree of correlation within their data sets. All calibrated data presented from these two measurement periods fall within the 10 % tolerance range set by the TMT site selection committee as a reference standard for the intercomparison of absolute PWV IRMA data.

Chapter 6

Conclusion

6.1 Summary

In this thesis I have demonstrated a method for intercalibrating several IRMA instruments resulting in PWV measurements correlated to within ∼10% absolute PWV. While there are still some remaining systematic effects, as seen in Figures 5.13 and 5.16, we are confident that through refining the calibration procedure a further improvement may be obtained. I have shown that calibration relative to a primary reference blackbody while measuring temperatures within the IRMA unit is necessary to identify and account for stray radiation entering the detector from sources within the IRMA instrument. I have also shown through parametric analysis of the atmospheric models used in this study, that the uncertainties within the input parameters are negligible apart from the scale height of water vapour. The scale height of water vapour was found to be the primary source of uncertainty in the model; not surprising since it is also the most rapidly varying parameter both temporally and spatially.

The initial application of IRMA was as a phase correction tool for radioastronomy [1]. In this application the devices are located in close proximity to one another, and therefore a relative measurement of water vapour is sufficient. When used as an infrared opacity monitor for site selection, the central theme of this thesis, the units will be located on different mountain tops at widely dispersed locations. Absolute measurements are required to allow meaningful comparison of water vapour measurements obtained at these sites. A calibration procedure was developed to relate each IRMA instrument directly to a single reference blackbody source. This calibration is necessary to account for stray radiation within each radiometer. In order to identify and account for this stray radiation, we have developed a calibration scheme that incorporates temperature sensors located within the IRMA unit itself. This calibration method has been verified through changing the operating environment of one IRMA unit relative to two other units co-located, observing the same patch of sky.

Every remote sounding instrument requires a retrieval scheme based upon an atmospheric model. The model we use is a locally developed line-by-line layer-by-layer radiative transfer model called BTRAM [3]. The model is based on the HITRAN 2004 spectral database and uses atmospheric profiles derived from both FASCODE and the U.S.Standard Atmosphere 1976. The atmospheric profile represents one potential systematic source of error that can be reduced by use of a site-specific model. In order to create a site-specific model I have analysed $\sim$3000 radiosonde data sets for radiosondes launched from Antofagasta, Chile, the nearest airport to the sites being considered. I have found that pressure, temperature, and lapse rate are relatively stable over time, and can be well represented with statistically derived means for their respective profiles or values. However, from a purely

statistical analysis perspective the scale height of water vapour exhibits the largest variance and is the principle source of error in the retrieved water vapour measurement. Its value varied from $\sim 1.1-1.7$ km, resulting in PWV uncertainties of $\sim 20-30\%$, which illustrates the importance of this parameter to the retrieved PWV values.

6.2 Lunar spectrophotometer

When measuring PWV in remote sites, it would be an advantage to have independent measures of PWV to validate the PWV measurements being made by IRMA. Many such measurements exist, including 183 GHz heterodyne radiometers, PWV derived from GPS measurements, opacity measurements such as CSO Tau tipper, and MIKE [50]. What would be most advantageous would be a hand-hold monitor that could be used simultaneously with IRMA measurements at a remote location. One such measure is proposed by modifying the design of a solar spectrophotometer [51] [52]. This instrument measures a water absorption feature in the near-IR at 0.94 μm and ratios it with respect to an off-band measurement. The spectrophotometer described by Thome is designed to use solar radiation as its background source, whereas the PWV measurements most applicable to our instance are nighttime values. The only source bright enough to be measured by a relatively small instrument would be solar radiation reflected from the lunar surface. I am currently in the proof of concept stage of the lunar spectrophotometer development

6.3 IRMA deployment at Dome C, Antarctica

All of the work presented in this thesis lends itself directly to my Ph.D. research which will include an IRMA deployment to Dome C, Antarctica, scheduled for 2007-2008.

Table 6.1: Dome C, AWS data 1994

	Mean T (°C)	Max T (°C)	Min T (°C)
Max	−28.6 (Jan)	−16.0 (Jan)	−44.5 (Dec)
Min	−67.8 (Aug)	−46.0 (Aug)	−80.0 (Aug)

The astronomical observing conditions in Antarctica are unparalleled anywhere on Earth. According to the 1994 report edited by M. Burton [24], the Antarctic plateau is the most favourable terrestrial site for astronomical development due to its dark sky, hyper-dry, steady, and clear air, minimal interference from man-made sources, possibility for continuous observation, and geographical considerations. Studies have shown that for roughly 0.5% of observation times the conditions of observation from Dome C would parallel those afforded the space-based Hubble telescope [5].

An IRMA unit is in the process of being retrofitted for use in one of the most hostile environments on Earth, Dome C in Antarctica. Table 6.1 contains the meteorological data from an automatic weather station (AWS) taken in 1994, Argos number 8904, Latitude 74.50S, Longitude 123.00E, Altitude 3260 m. The mean temperature at Dome C is −51.5 °C. Mean air pressure is 64.5 kPa. Mean wind speed ranges between 1.8 and 3.1 m/s. Max wind speed recorded during the 1994 data set was 12 m/s.

To simulate the Antarctic winter our group has procured a low-temperature freezer able to house a fully assembled IRMA unit. Initial tests of IRMA at −80 °C found most components to be inoperable at that temperature. Systematically we have tested and replaced components, progressively developing a fully functional, Antarctic qualified unit.

Several modifications were required to achieve this goal. The electronics were found not to function below −40 °C. This was solved by first heating the boards to −40 °C with heating pads, then subsequently powering them up. The lubricant in all of the

electric motors was a major challenge, it becomes highly viscous preventing motion at −80 °C. Motors were opened, de-greased, and then re-greased with a lubricant rated to −100 °C. Belts on the ALT drive system and lid-mechanism broke at low temperature. These were successfully replaced with chain-link drives. Moveable wires connecting IRMA to the power system and communications system have been replaced with Teflon coated wires that remain flexible at −100 °C.

Heating IRMA to a suitable operating temperature is the simplest solution. This, however, is impractical because energy is in short supply in Antarctica and will be at a premium. The entire IRMA system, including its site computer, electronics, cooler, calibration blackbody, motors, sensors, and heating-pads will all need to powered within a limited energy budget. At present, a heated and operational IRMA system requires ∼0.2 kW. Further reduction of this energy footprint will require two-stage operation: an initial warm-up stage, then switching off the heaters and diverting energy to power the electronics and other components. The biggest challenge is economizing on power whilst heating critical components within the low-power restrictions imposed by the location.

Characterization of water vapour in the 20 μm spectral region above Antarctica using an IRMA instrument will be both novel and the foundation for my Ph.D. thesis research.

Fin.

References

[1] G. J. Smith. *An Infrared Radiometer For Millimeter Astronomy*. MSc thesis, University of Lethbridge, Lethbridge, AB (2001).

[2] MCT infrared detector #KMPC19-1-SP, Kolmar Technologies, Inc. URL `http://www.kolmartech.com`.

[3] I. M. Chapman. *The Atmosphere Above Mauna Kea At Mid-Infrared Wavelengths*. MSc thesis, University of Lethbridge, Lethbridge, AB (2003).

[4] J. S. Lawrence, *et al.* "The AASTINO: Automated Astrophysical Site Testing INvincible Observatory." *Memorie della Societa Astronomica Italiana Supplement*, **2**:217–220 (2003).

[5] J. S. Lawrence, *et al.* "Exceptional astronomical seeing conditions above Dome C in Antarctica." *Nature*, **431**:278–281 (16 Sept 2004).

[6] Honeywell Hymatic, Redditch, Worcestershire, UK. URL `http://www.hymatic.co.uk/`.

[7] L. Barron, L. Hecht, and G. Wilson. "The Lubricant of Life: A Proposal That Solvent Water Promotes Extremely Fast Conformational Fluctuations in Mobile Heteropolypeptide Structure." *Biochemistry*, **36**(43):13143–13147 (1997).

[8] M. Pidwirny. "Fundamentals of Physical Geography, 2nd Edition." (2006). URL `http://www.physicalgeography.net/fundamentals/contents.html`.

[9] "NASA MODIS homepage." National Aeronautics and Space Administration, U.S.A. URL `http://modis.gsfc.nasa.gov/index.php`.

[10] H. D. Young and R. A. Freedman. *University Physics with Modern Physics*. 11th edition. Addison Wesley: San Francisco, California, U.S.A. (2004).

[11] M. C. B. Ashley, *et al.* "Robotic telescopes on the Antarctic plateau." *Astronomische Nachrichten*, **325**:619–625 (2004).

[12] I. M. Chapman and D. A. Naylor. "Development of a Freely Distributed, Customizable Atmospheric Radiative Transfer Model." In *Fourier Transform Spectroscopy/ Hyperspectral Imaging and Sounding of the Environment*. Technical Digest (CD), paper HTuD2, OSA (2005).

[13] H. J. P. Smith, *et al.* "FASCODE: Fast Atmospheric Signature Code (Spectral Transmittance and Radiance)." Technical Report AFGL-TR-78-0081, Air Force Geophysics Laboratory, Hanscom AFB, Massachusetts, U.S.A. (1978).

[14] "Interactive Data Language." Product information from ITT Visual Information Solutions, Boulder, CO, U.S.A. URL `http://www.ittvis.com/idl/`.

[15] L. Rothman, *et al.* "The HITRAN 2004 molecular spectroscopic database." *Journal of Quantitative Spectroscopy and Radiative Transfer*, **96**(2):139–204 (2005).

[16] D. A. Naylor, *et al.* "Atmospheric emission in the 20-micron window from Mauna Kea." *Publications of the Astronomical Society of the Pacific*, **96**:167–173 (1984).

[17] WinSystems, Inc. 715 Stadium Drive, Arlington, Texas, 76011, USA. URL `http://www.winsystems.com/`.

[18] Advanced Micro Peripherals Ltd. URL `http://www.ampltd.com/`.

[19] Rabbit Semiconductor, 2900 Spafford Street, Davis, California, 95618-6809, USA.

[20] R. Phillips, *et al.* "Initial results of field testing an infrared water vapour monitor for millimeter astronomy (IRMA III) on Mauna Kea." In *Ground-based Telescopes*, **5489**:100–101. SPIE (2004).

[21] I. S. Schofield. *The IRMA III Control and Communication System*. MSc thesis, University of Lethbridge, Lethbridge, AB (2005).

[22] "Thirty Metre Telescope - Instrumentation." Canadian aspects of the Thirty Metre Telescope. URL `http://lot.astro.utoronto.ca/design/instrument.html`.

[23] F. K. Lutgens and E. J. Tarbuck. *The Atmosphere: An Introduction to Meteorology*. 6th edition. Prentice Hall College Division: Prentice Hall, Paramus, NJ, U.S.A. (1995).

[24] M. Burton. "The Scientific Potential for Astronomy from the Antarctic Plateau." (1994). URL `http://citeseer.ist.psu.edu/burton94scientific.html`.

[25] Lord Rayleigh. "On the light from the sky, its polarization and colour." *Phil. Mag*, **41**:107–120,274–279 (1871).

[26] S. Chandrasekhar. *Radiative Transfer*. 1st edition. Dover Publications, Inc.: New York, U.S.A. (1960).

[27] P. Bernath. *Spectra of Atoms and Molecules*. 2nd edition. Oxford University Press: New York, U.S.A. (1995).

[28] J. M. Hollas. *Modern Spectroscopy*. 4th edition. John Wiley & Sons, Ltd.: Chichester, West Sussex, England (2005).

[29] D. J. Griffiths. *Introduction to Quantum Mechanics*. 2nd edition. Addison-Wesley: Boston, MA, U.S.A. (2004).

[30] R. C. Weast, *et al.* (Eds.). *CRC Handbook of Chemistry and Physics*. 70th edition. CRC Press, Inc.: Boca Raton, FL, U.S.A. (1989).

[31] "JPL Molecular spectroscopy catalogue." Jet Propulsion Laboratory, California Institute of Technology, CA, U.S.A.

[32] U. S. C. on Extension to the Standard Atmosphere. "U.S. Standard Atmosphere, 1976." , National Oceanic and Atmospheric Administration, National Aeronautics and Space Administration, United States Air Force, Washington D.C., U.S.A. (1976).

[33] A. M. Larar, *et al.* "Airborne Imaging Fabry-Perot Interferometer System for Tropospheric Trace Species Detection." In *Earth Science Technology Conference - 2002*. Earth Science Technology Office, NASA (2002).

[34] M. Born. *Principles of Optics*. 7th edition. University Press: Cambridge, U.K. (2005).

[35] S. P. Davis, M. C. Abrams, and J. W. Brault. *Fourier Transform Spectrometry*. 1st edition. Academic Press (2001).

[36] K. Schwarzschild. "Über das Gleichgewicht der Sonnenatmosphäre." *Göttinger Nachrichten Math-Phys Klasse*, **195**:41–53 (1906).

[37] J. T. Houghton. *The physics of atmospheres*. 2nd edition. Cambridge University Press: University Press, Cambridge, U.K. (1986).

[38] K. N. Liou. *An Introduction to Atmospheric Radiation*. 2nd edition. Academic Press: Burlington, MA, U.S.A (2002).

[39] J. T. Houghton, F. W. Taylor, and C. D. Rodgers. *Remote sounding of atmospheres*. 1st edition. Cambridge University Press: University Press, Cambridge, U.K. (1984).

[40] "NOAA/FSL/FRB/MAB - RAOB - Radiosonde Database Access." NOAA Earth Systems Research Laboratory, Boulder, CO, U.S.A. URL `http://raob.fsl.noaa.gov`.

[41] B. Schwartz and M. Govett. "A Hydrostatically Consistent North American Radiosonde Data Base At The Forecast Systems Laboratory, 1946-Present." NOAA Technical Memorandum ERL FSL-4, Forecast Systems Laboratory, National Oceanic and Atmospheric Administration, Boulder, Colorado, U.S.A. (August 1992).

[42] The answer to the ultimate question of life, the universe and everything.

[43] R. M. Goody and J. C. G. Walker. *Atmospheres*. 1st edition. Prentice-Hall Inc.: Englewood Cliffs, New Jersey, U.S.A. (1972).

[44] "The International System of Units (SI)." Bureau International des Poids et Mesures. URL `http://www.bipm.org/en/si/`.

[45] "AMS Glossary of Meteorology." American Meteorological Society. URL `http://amsglossary.allenpress.com/glossary/browse?s=s&p=75`.

[46] D. Bolton. "The Computation of Equivalent Potential Temperature." *Monthly Weather Review*, **108**:1046–1053 (1980).

[47] Cirrus Logic, Inc. 2901 Via Fortuna, Austin, Texas, 78746, U.S.A. URL `http://www.cirrus.com/en/`.

[48] Lake Shore Cryotronics, Inc. 575 McCorkle Blvd, Westerville, Ohio, 43082, U.S.A. URL `http://www.lakeshore.com/`.

[49] Fisher Scientific 825F Oven. URL `https://www.fishersci.com/`.

[50] J. Thomas-Osip, *et al.* "Calibration of the Relationship between Precipitable Water Vapor and 225 GHz Atmospheric Opacity via Optical Echelle Spectroscopy at Las Campanas Observatory." *Publications of the Astronomical Society of the Pacific*, **119**:697–708 (2007).

[51] K. J. Thome, B. M. Herman, and J. A. Reagan. "Determination of Precipitable Water from Solar Transmission." *Journal of Applied Meteorology*, **31**:157–165 (1992).

[52] K. J. Thome, *et al.* "Three-channel solar radiometer for the determination of atmospheric columnar water vapor." *Applied Optics*, **33**:5811–5819 (1994).